

Age stratigraphy and basal properties of the East Antarctic Ice Sheet from radio-echo sounding measurements – and inferences about ice dynamics –

Kumulative Dissertation
zur Erlangung des akademischen Grades Dr. rer. nat.
vorgelegt dem Fachbereich Geowissenschaften
der Universität Bremen im April 2018
von Anna Winter

Erstgutachter: Prof. Dr. Olaf Eisen
Zweitgutachter: Prof. Dr. Tilo von Dobeneck

Datum des Dissertationskolloquiums: 25. Mai 2018

Erklärung

Ich versichere, dass

1. die Dissertation ohne unerlaubte fremde Hilfe angefertigt wurde,
2. keine anderen als die von mir angegebenen Quellen und Hilfsmittel benutzt wurden und
3. die den benutzten Werken wörtlich oder inhaltlich entnommenen Stellen als solche kenntlich gemacht wurden.

Bremen, den 17.07.2018

.....
(Anna Winter)

Zusammenfassung

Die Ostantarktis stellt einen erheblichen Unsicherheitsfaktor in aktuellen Prognosen zum globalen Meeresspiegelanstieg dar. Diese Prognosen beinhalten lediglich vernachlässigbare Beiträge des Ostantarktischen Eisschildes (OAES) zum Meeresspiegelanstieg, da der Eisschild momentan insgesamt nicht an Masse verliert und dort auch bei einer globalen Erwärmung von einigen Grad höchstwahrscheinlich kein erhebliches Schmelzen auftreten wird. Nichtsdestotrotz ist eine schnelle Destabilisierung großer Teile des OAES nicht auszuschließen. Solche Szenarien sind in aktuellen Meeresspiegelprognosen nicht berücksichtigt, da weder Zeit und Geschwindigkeit, noch die genauen Rahmenbedingungen für eine solche Destabilisierung abschließend geklärt sind. Geologische Datensätze zeigen aber, dass solche Zerfälle in der Geschichte des OAES bereits auftraten. Um das Verhalten des OAES im Klimawandel besser zu verstehen, muss deshalb seine Reaktion auf frühere Klimaänderungen untersucht werden. Eine gute Möglichkeit dies zu tun bereitet die Erforschung des Eisschildes selbst, da (i) die Geschichte und Fließdynamik des Eisschildes in seiner inneren Struktur abgebildet sind und (ii) das Eis und die darin eingeschlossene Luft wertvolle Informationen über die Klimageschichte enthalten. Die Stratigrafie des Eisschildes kann mit Radarmessungen abgebildet werden. Eine Kartierung der Stratigrafie über den gesamten Kontinent könnte zu einer Verbesserung sowohl für die Rekonstruktion der Klimageschichte als auch für die Fließmodelle zur Prognose des Meeresspiegelanstiegs beitragen.

Ziel meiner Dissertation ist es, die innere Struktur und die basalen Eigenschaften eines möglichst großen Anteils des OAES mit Hilfe von Radarmessungen abzubilden und daraus die Fließdynamik des Eisschildes und Orte mit möglichst altem Eis abzuleiten. Dies wurde in drei gesonderten Veröffentlichungen erarbeitet, die sich jeweils auf eine andere Entwicklungsstufe der großskaligen Kartierung und Interpretation der Stratigrafie und des Felsbetts konzentrieren. Die erste Publikation bildet die methodologische Grundlage. Es wird beurteilt, ob die Radardaten verschiedener Systeme miteinander kombinierbar sind, was die Grundvoraussetzung für eine großflächige Abdeckung der Ostantarktis ist. Außerdem wird unter Zuhilfenahme einer synthetischen Radarspur, berechnet aus Dichte- und Leitfähigkeitsmessungen an einem Eiskern, die Ursache für einzelne Reflexionen in den Radardaten untersucht. Dadurch kann festgestellt werden, ob die Reflexionen, die in den Radarprofilen über den Eisschild verfolgt werden können, isochron und für eine Kartierung der Alters-Tiefen-Verteilung geeignet sind. Es zeigte sich, dass beides zutreffend ist.

Die Erkenntnisse werden in der zweiten Publikation verwendet, um eine großskalige Kartierung der Alters-Tiefen-Struktur des OAES zu erstellen. Die Tiefenverteilung der Paleo-Eisoberflächen gibt einen Überblick über die Akkumulationsverteilung über den

OAES. Anhand der Tiefenlage der ältesten Isochrone im Verhältnis zur Eisdicke kann abgeschätzt werden, wo das basale Eis älter oder jünger ist als am Ort des bisher ältesten Eiskerns. Der Versuch einer quantitativen Berechnung der Akkumulationsraten verschiedener Zeitintervalle und auf großer räumlicher Skala lieferte keine vertrauenswürdigen Ergebnisse. Für die Berechnung exakter Akkumulationsraten über den kompletten Eisschild müssen die Radarisochronen vermehrt in Fließmodelle eingebunden werden.

Der dritte Teil meiner Dissertation betrachtet die Rauigkeit des Ostantarktischen Gletscherbettes, welche die Eisdynamik sowohl stark beeinflusst, als auch von ihr beeinflusst wird. Ich führte eine statistische Analyse der Betttopografie des OAES durch, um dessen basale Eigenschaften zu bewerten. Dadurch konnten verschiedene Landschaftsformen unter dem Eisschild klassifiziert werden. Außerdem wurden Zusammenhänge zwischen der basalen Rauigkeit, der Fließgeschwindigkeit des Eises und der Temperatur an der Basis des Eisschildes beobachtet. In Regionen mit langsamen Fließgeschwindigkeiten zeigt einer der Rauigkeitsparameter signifikante Unterschiede, je nachdem, ob das Eisschildbett warm oder kalt ist. Dies könnte zukünftig eine Möglichkeit sein, um unter gewissen Umständen Rückschlüsse von der Bettrauigkeit auf die Temperaturbedingungen des Eisschildbettes zu ziehen oder die Orte, an denen Modelle ein temperiertes Bett vorhersagen, zu validieren.

Abstract

In current projections of future global sea-level rise, East Antarctica constitutes a major factor of uncertainty. Such projections show negligible contribution from the East Antarctic Ice Sheet (EAIS), because, overall, it is not losing mass at the moment and even with few degrees of warming most probably no substantial melting will occur. Nevertheless, it is possible that large parts of the EAIS disintegrate rapidly. Such scenarios are not included in the current projections, because it is not conclusively clarified when, how fast, and under which exact boundary conditions this happens. However, geological records suggest that the EAIS did disintegrate in the past. To better understand how the East Antarctic Ice Sheet will behave in a changing climate, it is therefore necessary to investigate its past responses to climatic transitions. This is best undertaken by looking at the ice sheet itself, because (i) the internal structure of an ice sheet is an imprint of its history and dynamics, and (ii) the ice and enclosed air provide valuable information about the past climate. The internal stratigraphy of the ice can be revealed by means of radio-echo sounding (RES) measurements. An established continental-wide stratigraphy can constrain both paleo-climate reconstructions and ice-flow models.

The aim of my thesis is to infer the internal stratigraphy and basal properties of the EAIS from RES measurements over an area as wide as possible and to interpret its characteristics with respect to ice dynamics and occurrence of old ice. This was achieved with three separate publications, each focusing on a different stage of mapping and interpreting a large-scale stratigraphy and basal properties. The first publication builds the methodological basis by evaluating the compatibility of multiple RES data sets, a prerequisite for large-scale mapping of the stratigraphy of the EAIS, where no reasonable coverage is obtained with only one data set. The physical cause for specific internal reflections in the RES data is investigated, using a synthetic RES trace calculated from ice-core density and conductivity profiles, to ensure their isochronicity and consequential usability for mapping the age-depth distribution throughout the ice sheet. Both have proved to be feasible.

This expertise is used in the second publication to map on a large scale the age-depth stratigraphy across the EAIS. This depth distribution of paleo surfaces gives an overview of the accumulation-rate distribution across the ice sheet. By the percentage depth of the oldest traced isochrone it can be estimated where basal ice is older or younger than at the drill site of the so far oldest ice core. The attempt to quantitatively derive mean accumulation rates for different time periods miscarried for the large scale, highlighting that more efforts are needed to incorporate RES isochrones into ice-flow models.

The third part of my thesis focuses on the roughness of the subglacial bed beneath the EAIS, a key factor in the control of ice dynamics and at the same time affected by past

ice flow. I assessed the basal properties of the EAIS by statistical analysis of the bed topography, allowing for a classification of different subglacial landscapes. Furthermore, relationships between basal roughness, ice-flow speed and basal temperatures were observed. In East Antarctic regions with slow flow speed, there are significant differences in one of the roughness parameters for cold and warm conditions at the bed. This could in future serve as a new method to use the basal roughness to infer, under some circumstances, the basal thermal condition, or validate modeled temperate-bed locations.

Contents

1	Introduction	1
1.1	Ice sheets and climate	1
1.2	Ice sheets as archives	3
1.3	Radio-echo sounding in glaciology	3
1.4	The East Antarctic Ice Sheet	5
1.5	Objectives and structure of the thesis	6
2	Radio-echo sounding measurements	9
2.1	Electro-magnetic wave propagation	9
2.2	Electro-magnetic waves at interfaces	11
2.3	Radio-echo sounding systems	13
2.4	RES data and processing	15
3	Publication synopsis	21
3.1	Paper I: Comparison of measurements from different radio-echo sounding systems and synchronization with the ice core at Dome C, Antarctica	21
3.2	Paper II: Deducing large-scale age distribution and paleo-accumulation rates from radiostratigraphy in East Antarctica	22
3.3	Paper III: Basal roughness of the East Antarctic Ice Sheet and its indications for ice flow and basal thermal state	23
4	Comparison of measurements from different radio-echo sounding systems and synchronization with the ice core at Dome C, Antarctica	25
4.1	Introduction	26
4.2	Synthetic radar traces	28
4.2.1	Ice core data	28
4.2.2	Electro-magnetic modeling of radar traces	29
4.2.3	Assessing the permittivity of ice	30
4.3	Radio-echo sounding data	31
4.4	Assembling the data sets	34
4.5	Results	35
4.5.1	Single traces, A-scope	35
4.5.2	Radargrams, Z-scope	36
4.5.3	Depths of the RES reflectors	39
4.6	Discussion	39
4.6.1	Comparability of RES data	40
4.6.2	Synchronization of RES and ice core data	44
4.7	Conclusions	47
4.8	Acknowledgements	48

5	Deducing large-scale age distribution and paleo-accumulation rates from radiostratigraphy in East Antarctica	51
5.1	Introduction	51
5.2	Study region	53
5.3	Data and Methods	54
5.3.1	RES data	54
5.3.2	RES internal reflection horizons	54
5.3.3	Deriving accumulation rates	56
5.4	Results	58
5.4.1	Age stratigraphy	58
5.4.2	Mean accumulation rates	60
5.5	Discussion	63
5.5.1	Age stratigraphy	63
5.5.2	Accumulation rates	66
5.6	Conclusions	69
5.7	Acknowledgements	70
6	Basal roughness of the East Antarctic Ice Sheet and its indications for ice flow and basal thermal state	71
6.1	Introduction	71
6.2	Data and method	73
6.2.1	Radio-echo sounding data	73
6.2.2	Roughness parameters	75
6.3	Results	76
6.3.1	Roughness parameters	76
6.3.2	Landscape classification	76
6.3.3	Hurst exponent and basal temperature	79
6.3.4	Roughness and flow speed	80
6.4	Discussion	82
6.4.1	Landscape classification	82
6.4.2	Does the Hurst exponent indicate thermal conditions at the base?	84
6.5	Conclusions and outlook	87
7	Conclusions and perspectives	89
	Bibliography	93
	Appendix	111
	Appendix A: Mapping the Raymond bump at Søråsen	111
	Appendix B: Exemplary RES images of structures seen in the radiostratigraphy	115
	Appendix C: List of publications	121

List of Abbreviations

AGAP	Antarctica's Gamburtsev Province Project
AWI	Alfred Wegener Institute, Helmholtz Centre for Polar and Marine Research, Bremerhaven, Germany
BAS	British Antarctic Survey
BE-OI	Beyond EPICA - Oldest Ice
COF	Crystal-orientation fabric
CReSIS	Center for Remote Sensing of Ice Sheets, University of Kansas, Lawrence, USA
DA	Dome Argus (Dome A)
DC	Dome Concordia (Dome C)
DEP	Dielectric Profiling
DF	Dome Fuji (Dome F)
DML	Dronning Maud Land
EAIS	East Antarctic Ice Sheet
EDC	EPICA Dome C
EDML	EPICA Dronning Maud Land
EPICA	European Project for Ice Coring in Antarctica
GrIS	Greenland Ice Sheet
Hc	Holocene
ICECAP	International Collaborative Exploration of the Cryosphere through Airborne Profiling
INGV	Istituto Nazionale di Geofisica e Vulcanologia, Rome, Italy
IPCC	Intergovernmental Panel on Climate Change
IPICS	International Partnerships in Ice Core Sciences
IRH	Internal Reflection Horizon
LDEO	Lamont-Doherty Earth Observatory, Columbia University, New York, USA
LG	Last Glacial
MPT	Mid-Pleistocene Transition
PG	Penultimate Glacial
PISM	Parallel Ice Sheet Model
pmp	pressure melting point
RES	Radio-Echo Sounding
RMS	Root-Mean Square

SAR	Synthetic-Aperture Radar
SCAR	Scientific Committee on Antarctic Research
SIA	Shallow ice approximation
SSA	Shallow shelf approximation
TWT	Two-way travel time
UTIG	University of Texas Institute for Geophysics, Austin, USA
WAIS	West Antarctic Ice Sheet

List of Parameters

μ	complex-valued magnetic susceptibility [$\text{V s A}^{-1} \text{m}^{-1}$]
ε	complex-valued electrical permittivity $\varepsilon = \varepsilon' + i\varepsilon''$ [$\text{A s V}^{-1} \text{m}^{-1}$]
E	electric field [V m^{-1}]
t	time [s]
ω	circular frequency [$\text{s}^{-1} \equiv \text{Hz}$]
k	complex wave vector [m^{-1}]
c	electro-magnetic wave speed [m s^{-1}]
n	refraction index []
σ	electrical conductivity [S m^{-1}]
ρ	density [kg m^{-3}]
q	refraction gain [dB]
R_A	amplitude reflection coefficient []
f	frequency [Hz]
B	bandwidth [Hz]
P	power [W]
G	Antenna gain [dB]
L	two-way-path power loss [dB]
v	flow speed (v_x, v_y, v_z) [m s^{-1}]
\dot{b}_b	basal mass balance [$\text{kg m}^{-2} \text{a}^{-1}$]
\dot{b}_s	surface mass balance [$\text{kg m}^{-2} \text{a}^{-1}$]
ν	root-mean-square deviation of bed elevation, 'amplitude roughness' [m]
H	Hurst exponent, 'wavelength roughness' [] (and ice thickness [m] in Chap. 5)

List of Figures

2.1	Sketch of RES measurements in common-offset configuration	14
2.2	Overview of East Antarctic place names and RES profiles being used	17
2.3	Radargram in Landmark for IRH tracing	18
2.4	Two radargrams in Landmark while transferring IRHs	18
4.1	East Antarctic deep drill sites and RES profiles around Dome C	32
4.2	A-scopes of five radar systems and synthetic trace at Dome C	35
4.3	Z-scopes of five radar systems and synthetic trace at Dome C	37
4.4	AWI and UTIG radargram for IRH transfer	42
4.5	Age gradient in the EDC ice core	47
5.1	Antarctica with the two investigated regions and RES profiles with continuously traced IRHs	53
5.2	IRH depths, normalized depths and accumulation rates along example profiles . .	59
5.3	IRH-depth distribution across East Antarctica	61
5.4	Accumulation-rate distribution across East Antarctica	63
5.5	Comparison of accumulation rates with another study	67
6.1	Flow speed, basal temperature and two roughness parameters in East Antarctica .	77
6.2	Scatter plot of the distribution of the two roughness parameters	78
6.3	Distribution of subglacial landscape classes in East Antarctica	79
6.4	Frequency of the roughness parameters for different basal thermal conditions . . .	81
6.5	Behavior of the wavelength-roughness parameter with basal temperature	82
6.6	Behavior of the roughness parameters with flow speed	83
6.7	Behavior of wavelength roughness with basal temperature for fast and slow flow speeds	85
6.8	Modeled basal temperatures where our method predicts a thawed bed	86
A1	Location of Sørasen	112
A2	Radargram 1 imaging the Raymond bump at Sørasen	112
A3	Radargram 2 imaging the Raymond bump at Sørasen	113
A4	Radargram 3 imaging the Raymond bump at Sørasen	113
A5	RES profiles and mapped Raymond bump at Sørasen	114

B1	Example radargram with flat stratigraphy	116
B2	Example radargram at Lake Vostok	117
B3	Radargram 1 with disturbed stratigraphy close to Dome A	118
B4	Radargram 2 with disturbed stratigraphy between Dome A and Vostok	118
B5	Radargram 3 with disturbed stratigraphy from the AGAP-S data	119

1 Introduction

1.1 Ice sheets and climate

The future behavior of the Earth's ice sheets in a continually warming climate is of great importance to us as a species, due to its impact on the habitability of our planet. For at least the last two decades, continental ice sheets have been decaying increasingly rapidly (Rignot et al., 2011; Vaughan et al., 2013, Sect. 4.4.3). This loss of mass from continental ice has a direct impact on global sea level. In total, the Greenland Ice Sheet (GrIS) and West Antarctic Ice Sheet (WAIS) have the capacity to produce about 7 m eustatic sea-level equivalent each, whilst melting the East Antarctic Ice Sheet (EAIS) would equate to about 54 m eustatic sea-level rise (Huybrechts et al., 2000; Cuffey and Paterson, 2010). Such a sea-level rise would massively reduce the available land space for agriculture and directly affect a large proportion of the human population as most settlements are located in direct vicinity of the coasts.

In addition to the direct impact of melting ice sheets on sea level, the cryosphere can also affect human activity in more subtle ways. The release of freshwater masses by melting ice sheets changes the composition of nearby ocean waters, which in turn affects regional and global weather systems and ocean currents, potentially leading to abrupt climate shifts (Rahmstorf, 2002; Lenton et al., 2008). Enhanced freshwater fluxes from melting glaciers in the Arctic are thought to have already weakened the Atlantic meridional overturning circulation over the past 150 years (Thornalley et al., 2018). In affecting atmospheric and ocean circulation, the heat and moisture transport throughout the entire climate system is altered. This can act to increase the occurrence of extreme events, for example, bringing more floods to humid regions, more droughts to arid regions, and increasing the frequency of large storms and tornados (Intergovernmental Panel on Climate Change (IPCC), 2014). The adaptation to these changes will become an increasingly important task in the future.

To react to a changing environment, it is essential to know what to expect. One way to anticipate the future behavior of the Earth system is to study its past. Archives of past

climate show that there has always been climate change in Earth history, albeit not with the rate of the current anthropogenic warming. During the Quaternary, the last 2.6 Ma of Earth history, the climate state of Earth fluctuated between cold glacial periods and warm interglacial periods with a regular cyclicity (e.g., Lisiecki and Raymo, 2005). The frequency content of these climatic transition cycles can be explained by orbital parameters and resultant variations in solar insolation (Milankovitch cycles, Milankovitch, 1941; Hays et al., 1976). Yet, the amplitudes and dominant frequencies are thought to be determined by a combination of non-linear feedback mechanisms and changing greenhouse-gas concentration (Masson-Delmotte et al., 2013), which are sometimes difficult to pinpoint. For example, the causes for the Mid-Pleistocene Transition (MPT) have not yet been conclusively identified. The MPT is characterized by a cyclicity change at about 1 Ma from low-amplitude, high-frequency (41 ka period) to higher-amplitude, low-frequency (100 ka period) glacial-interglacial cycles, essentially without a change of orbital forcing (Raymo et al., 2006).

Several feedback mechanisms of the ice sheets at the two poles play a major role in driving glacial–interglacial transitions (e.g., Lisiecki and Raymo, 2005; Clark et al., 2006; Cuffey and Paterson, 2010; Masson-Delmotte et al., 2013). They act to amplify or even initiate a change in climate. One powerful feedback mechanism is the change in albedo. The Earth’s absorption of energy from solar short-wave radiation increases when its surface is darkening. Such darkening surfaces in a warming environment are, for example, the replacement of sea ice by open ocean, retreating mountain glaciers, reduced seasonal snow cover, and a reduced area of summer snow on the ice sheets and glaciers. All of these processes increase the absorption of short-wave solar radiation, reinforcing further warming. Another important feedback mechanism of the ice sheets into the global climate system is given by a change in freshwater retention by the sheets, which may result in a rapid water release into the ocean. The density change of ocean waters in the ice-sheet vicinity enhances or diminishes deep-water formation, and thus affects ocean circulation, which can provoke abrupt climate oscillations (Dansgaard-Oeschger oscillations, Heinrich events, Dansgaard et al., 1993; Heinrich, 1988). The ice sheets are thought to be an important component affecting the pacing of glacial–interglacial cycles. For example, in the case of the MPT, the growth of larger ice sheets between 1250 ka and 900 ka ago, possibly enabled by exposure of a hard, high-friction crystalline bedrock (Clark and Pollard, 1998), and the resultant changing ice-sheet response to orbital forcing is thought to be one possible cause for the transition (i.e., the onset of the longer-period 100 ka cycles) (Clark et al., 2006; Elderfield et al., 2012).

1.2 Ice sheets as archives

Not only are the ice sheets an important component of the climate system, they are also a valuable archive of past climate states. Through the accumulation of annual layers of snow being compacted into ice which slowly flows from the continental interior to the margins, the ice sheets store the climatic history. The accumulated snow contains atmospheric air, which is trapped when the snow gets buried. The air exchange is completely stopped after the pore close-off, when the firn is finally compressed to ice. Afterwards, the air stays in the ice in form of bubbles and clathrates (e.g., Kipfstuhl et al., 2001). This paleo air, as well as dust and impurities washed out from the atmosphere or transported onto the ice by wind, can be retrieved from within ice cores and then be analyzed. In that way, polar ice provided many insights and illuminated new aspects of the climate of the past 800 ka, which is the age of the oldest ice retrieved as an ice core so far (EPICA community members, 2004). To go even further back in time and resolve more enigmas of the climatic history, for instance the cause of the MPT, requires retrieval of older ice in a continuous record. Future scientific goals of ice-core research, outlined by the Steering Committee of the International Partnerships in Ice Core Sciences (IPICS), aim at retrieving a new “Oldest Ice” ice core, a complete ice core spanning 1.5 Ma (Brook et al., 2006).

Ice cores are not the only cryospheric tool providing information about the past. The structure of an ice sheet in itself is the expression of the ice-sheet history. Summer and winter snow, snow from warmer and colder periods, and the precipitation after specific events like volcanic eruptions or atomic tests, all leave distinct fingerprints in the ice sheet and build up in a stratified structure. The initial stratigraphy from the ice-sheet formation is stored and slowly deformed by the ice-flow divergence. Therefore, the internal stratigraphy of an ice sheet is the imprint of its complete dynamic history. Examining the stratigraphy can thus provide information about past and current ice-sheet dynamics, e.g., about the amount and variation of snow accumulation over different time periods, the stability of ice rises, domes and ice divides, a changing position or extent of ice streams, regional surface erosion, or time-variable basal sliding (e.g., Raymond, 1983; Nereson and Waddington, 2002; Urbini et al., 2008; Winter et al., 2015; Das et al., 2013; Wolovick et al., 2014). These dynamic processes can be observed through radio-echo sounding (RES) images of the internal ice-sheet structure.

1.3 Radio-echo sounding in glaciology

Radio-echo sounding is an ideal method to reveal the internal stratigraphy of an ice sheet and the bedrock topography beneath it. RES has been used in glaciology for more than 50 years, starting with a focus on ice-thickness measurements. This has been used to reveal the subglacial bed topography on continental scales, which is not accessible to that extent

by other means (Robin et al., 1970; Evans and Smith, 1970; Evans et al., 1972). The bed topography and the nature of the RES signal from the bed reflection can be indicative of further properties of the subglacial bed, like its consistency of soft, deposited sediments or hard rock, its state of erosion, and even the thermal state at the bed (e.g., Oswald and Robin, 1973; Oswald, 1975; Siegert et al., 2005; Oswald and Gogineni, 2008; Bingham and Siegert, 2009; Li et al., 2010; Rippin et al., 2014; Urbini et al., 2015; Jordan et al., 2017; Diez et al., 2018). All of these properties affect the ice-sheet dynamics.

In addition to determining the ice thickness, RES can also be used to image the internal structure of ice sheets (Robin et al., 1969; Gudmandsen, 1970; Harrison, 1973; Gudmandsen, 1975; Paren and Robin, 1975). In more recent years, radar systems and data processing have been adjusted and advanced to target for an improved resolution of internal reflection horizons (IRHs). They are able to resolve those structures in the ice-sheet stratigraphy that provide further information about past ice-sheet dynamics and stability. Some examples are Raymond bumps that develop above temporally stable ice rises, domes and ice divides (Raymond, 1983; Nereson et al., 1998; Vaughan et al., 1999; Drews et al., 2013), (buried) ice-stream shear margins, indicating where fast ice flow ceased or changed its position (Jacobel et al., 1996, 2000; Clarke et al., 2000; Conway et al., 2002; Christianson et al., 2014), buried dunes or paleo surfaces truncated by wind scour (Das et al., 2013; Cavitte et al., 2016), disruptions in the stratigraphy, induced by changes in the flow regime (Karlsson et al., 2012; Holschuh et al., 2014; Panton and Karlsson, 2015), and basal freeze-on structures and folds (Bell et al., 2011, 2014; Wolovick et al., 2014; Bons et al., 2016; Wrona et al., 2018). Some of these structures were also observed and mapped in the context of this thesis. A collection with locations and exemplary RES images of these structures is given in Appendix A and B.

Furthermore, RES measurements are an important complement to ice-core analyses. While ice cores are valuable archives of past climate change, they contain only the momentary state at one single location. RES measurements can improve the interpretation of the ice-core records by informing about the provenance of the ice-core ice and potential irregularities along its flow path (Jacobel and Hodge, 1995; NEEM community members, 2013). With a direct connection of different deep ice cores by RES profiles with a continuous stratigraphy, the ice-core age scales can be synchronized and the uncertainties reduced (Siegert et al., 1998; Steinhage et al., 2013). Information about ice properties and age, retrieved from ice cores can be expanded to larger areas by RES measurements (e.g., Cavitte et al., 2016). This also makes RES measurements a valuable tool for reconnaissance studies for further ice-core drilling sites.

The spatial coverage of RES data of the major continental ice sheets, especially the GrIS, is good enough to facilitate a broad glaciological interpretation with respect to ice-sheet dynamics and response to climatic changes. Studies that illustrate the broadness and value

of RES data interpretation are, e.g., the studies by MacGregor et al. (2015a, b, 2016), where the deep radiostratigraphy was traced in RES data to obtain the ice volume of past glacial periods and to estimate the temperature distribution in the ice sheet from attenuation rates, and to infer the basal thermal state of the ice sheet. All of these aspects play a crucial role in influencing the ice-sheet dynamics. However, the full potential of available RES data is not yet exploited. Especially the combination of multiple data sets from different surveys and institutes provides the possibility for whole-ice-sheet interpretations also for Antarctica.

1.4 The East Antarctic Ice Sheet

Despite the growing number of RES surveys in Antarctica, the portion of the area mapped with RES remains far behind that of Greenland. The reason for this lag is the extensive area of the continent and its remoteness, which results in high cost for logistics and surveys. Another drawback is that past RES surveys on the EAIS have not been centrally coordinated, which resulted in surveys being conducted by numerous different institutes, using different RES systems with unclear compatibility of the generated data, partly without connection lines between different surveys or unfavorable survey design for IRH interpretation (Cavitte et al., 2016; Winter et al., 2017; Young et al., 2017). Notwithstanding these difficulties, understanding the behavior of the EAIS is crucial for anticipating future sea-level rise as it is the largest continental ice sheet and represents a major element of uncertainty in sea-level predictions (Cook et al., 2013; Ritz et al., 2015; Gulick et al., 2017). Even though the response of the EAIS to the ongoing climate change is currently not as apparent as that of the other continental ice sheets - and it is even gaining mass in some regions (e.g., Shepherd et al., 2012; Helm et al., 2014; Velicogna et al., 2014) -, there is evidence for large-scale deglaciations and EAIS contribution to sea-level rise in past warm periods (Williams et al., 2010; Miller et al., 2012; Cook et al., 2013; Aitken et al., 2016). The volume of the floating ice shelves, which buttress the EAIS, thereby preventing faster discharge of ice through the ice streams, is decreasing at an accelerating rate (Paolo et al., 2015). Recent studies (e.g., Gulick et al., 2017) suggest that the EAIS contributions to future sea-level projections (e.g., Vaughan et al., 2013; Golledge et al., 2015; DeConto and Pollard, 2016) might be underestimated because they assume stability of the EAIS. Even if the ice sheet will not collapse completely, the effect of a partial disintegration on global sea level is still major. One example is the Wilkes Land, especially vulnerable to instability, as much of the subglacial bed in this region is located below sea level (Walker, 2018). The Wilkes Land has been deglaciated several times during the evolution of the EAIS (Young et al., 2011). The ice streams and glaciers draining this region show high rates of grounding-line retreat (Konrad et al., 2018), indicating a possible collapse of their catchment areas (Joughin et al., 2014; DeConto and Pollard, 2016). The Wilkes Land alone

contains about 9 m sea level equivalent (Vaughan et al., 2013, Sect 4.4.5). Its disintegration would thus have a larger impact on our living environment than losing the entire GrIS or WAIS.

Apart from its important role in the climate system and its potential impact on global sea level, the EAIS, having evolved since the Eocene epoch (roughly 34 Ma – 56 Ma ago), is also the oldest ice sheet on Earth (Kennett, 1977; Miller et al., 1991; Lear et al., 2000; Coxall et al., 2005). This makes the EAIS the place to search for a suitable drill site for an ice core containing 1.5 Ma old ice, a keystone of unraveling the causes for the pacing of Quaternary climate cycles and the MPT (Brook et al., 2006; Fischer et al., 2013). The precise boundary conditions that have to be fulfilled at an East-Antarctic location for such old ice to still exist are outlined in Fischer et al. (2013), Young et al. (2017) and Van Liefferinge et al. (2018).

1.5 Objectives and structure of the thesis

This thesis aims at achieving a broad picture of the interior of the EAIS, using RES data, with regard to its stratigraphic architecture and inferences about ice-flow dynamics. This is relevant for both reconstructing and predicting the ice-sheet reaction to a changing climate. The study comprises three parts, one methodological, and two focused on application. The following specific issues are addressed by my thesis:

1. **Are the already available RES data, measured by different institutes with different instruments, combinable for joint analysis and interpretation?** Of particular interest is hereby the combinability of the IRH information from these RES data. To date, a large amount of RES data from the EAIS already exists, but the surveys of different institutes are focused on different regions and have not yet been combined for common interpretation. If this was to be accomplished, a long way would have been gone towards entire-ice-sheet interpretations of East Antarctic ice dynamics.
2. **Can reflections that appear as continuous horizons in the RES data set be matched with specific layers in ice cores?** A direct match between RES IRHs and ice-core measurements reveals which property of the ice is causing the the specific reflection in the RES data. The reflection cause informs about the isochronous character of the IRH and thus about its usability for mapping the age-depth stratigraphy of the ice sheet. Furthermore, this allows a determination of the exact depth of the origin of the reflection (within the limits of accuracy of ice-core depth measurements), defining the age of the IRHs more precisely than current methods of age assignment.
3. **Which information about ice dynamics and maximum age of the ice sheet can, and which cannot, easily be obtained from a dated IRH stratigraphy of the EAIS?**

Information of interest would be the distribution and temporal variation of accumulation rates, regions with basal melt or a disturbed stratigraphy of the deep ice, and the maximum age of the ice. This information can, for example, further constrain the regions suitable for drilling an Oldest Ice ice core, as all these aspects are key factors for retrieving old ice in a continuous, undisturbed record.

- 4. What can subglacial bedrock properties tell us about the ice-sheet history, its present state, and its future behavior, and how do we obtain this information?**
The nature of the subglacial bed holds a lot of valuable information about the past, present and future of an ice sheet, as its shape is formed by glacial erosion, while, at the same time, it is a key control on present and future ice flow. Depending on the bed material, soft sediment or hard crystalline rock, the friction and deformation properties that influence the flow speed of the ice sheet can vary over a large range. The nature of the subglacial bed might determine how fast the ice sheet will destabilize with increasing temperature and occurrence of liquid water (Jamieson et al., 2014).

With the work towards these objectives, my thesis contributes to the efforts of two currently running international projects, (i) the European Union's Horizon 2020 research and innovation programme 'Beyond EPICA - Oldest Ice' (BE-OI), aiming at the retrieval of 1.5 Ma old ice from East Antarctica, and (ii) the proposed Scientific Committee for Antarctic Research (SCAR) Science Programme 'AntArchitecture', working towards a combined database of the available RES data from Antarctica, facilitating a broad interpretation of the East Antarctic stratigraphic architecture to inform paleo-climate reconstructions and ice-flow modeling (Bingham et al., 2016).

The structure of the thesis takes the following form. As a preparation for the three main chapters, Chap. 2 provides a short introduction to the methods and measuring systems of RES, with a focus on application in polar glaciology.

The main part of the thesis is structured into three chapters (Chap. 4, Chap. 5 and Chap. 6) that represent the centerpiece of this work. Each of these standalone chapters has been or will be published separately in a peer-reviewed scientific journal. The text of these chapters is re-formatted, compared to the published and submitted versions, to fit the layout of this thesis. The bibliographies are combined with the overall bibliography at the end of the thesis. For consistency and to follow the publication standards, the first person plural is used throughout the three chapters. Chapter 3 gives a summary of the objectives, results and implications of these main chapters and lists the contributions of each author.

An overall conclusion and outlook is given in Chap. 7. It describes the outcome and merit of this work, and gives suggestions for potential follow-up studies.

2 Radio-echo sounding measurements

This chapter provides a summary of the methods of RES, focusing on polar glaciology. I start with a short introduction to the propagation of electro-magnetic waves, followed by a description of the measuring instruments, the data and the general data processing I applied. All references in this chapter are exemplary, as the rich history of RES in cryospheric studies yielded a vast number of valuable publications. There are also many review studies on RES in glaciology that can be referred to for more detailed information. Some examples are: Bogorodsky et al. (1985); Plewes and Hubbard (2001); Dowdeswell and Evans (2004); Bingham and Siegert (2007); Navarro and Eisen (2009).

2.1 Electro-magnetic wave propagation

Radio-echo sounding or radar is an active remote sensing technique, based on electro-magnetic waves from the very-high and ultra-high frequency bands. The propagation of electro-magnetic waves is controlled by the magnetic and electrical properties of the carrier medium. These properties are the complex-valued magnetic permeability $\mu = \mu_0\mu_r$, with $\mu_0 = 4\pi \cdot 10^{-7} \text{VsA}^{-1}\text{m}^{-1}$ and the complex-valued electrical permittivity $\varepsilon = \varepsilon_0\varepsilon_r$, with $\varepsilon_0 = 8.8542 \cdot 10^{-12} \text{AsV}^{-1}\text{m}^{-1}$. The relative magnetic permeability μ_r and the relative electrical permittivity ε_r are dimensionless complex values, given relative to those in vacuum (or, in good approximation, also in air). Many materials, including ice, are non-magnetic with the relative magnetic permeability $\mu_r = 1$ (Plewes and Hubbard, 2001). The material properties are connected by Maxwell's equations that describe electro-magnetic fields and form the basis of the classical electro-magnetism (Maxwell, 1864). A combination of Maxwell's equations for homogeneous media leads to the electro-magnetic wave equation for the electric field E :

$$\Delta E + \mu\varepsilon \frac{\partial^2 E}{\partial t^2} = 0. \quad (2.1)$$

The same equation holds for the magnetic field.

A solution of the differential wave equation is a harmonic plane wave, propagating, e.g., in z-direction:

$$E(z) = E_0(z) \exp^{i(kz - \omega t)}, \quad (2.2)$$

with the circular frequency ω in Hertz (Hz) and the wave number $k = |\mathbf{k}|$ in m^{-1} . $\mathbf{k} = \omega \sqrt{\mu \epsilon} \mathbf{n}$ is the complex wave vector, with the normal vector of the wave plane \mathbf{n} . The wave speed c is the velocity with which a certain phase propagates in space. A certain phase (also called wave front) is defined by $kz - \omega t = \text{const}$, hence

$$c = \frac{dz}{dt} = \frac{\omega}{k}. \quad (2.3)$$

It follows for non-magnetic materials

$$c = \frac{1}{\sqrt{\epsilon_0 \epsilon_r \mu_0}} = \frac{c_0}{\sqrt{\epsilon_r}} \quad (2.4)$$

in relation to the electro-magnetic wave speed in vacuum/air, $c_0 = 2.988 \cdot 10^8 \text{ ms}^{-1}$. The ratio of the wave speed in vacuum to that in the material $n = \sqrt{\epsilon_r}$ is called the refractive index of the material (Pellikka and Rees, 2009). For non-dispersive materials and vacuum, $c(k)$ is constant ($\sqrt{\epsilon \mu}$, n independent of ω). This is not fulfilled for most materials. However, dispersion is small in the range of frequencies used for RES measurements (Johari and Jones, 1976).

In materials (in contrast to vacuum), there is a phase shift between the applied electric field and the polarization. This is implied by the (relative) permittivity being a complex number with an imaginary part, the loss factor, that can be expressed as a function of the electrical conductivity σ (Siemens per meter, Sm^{-1}):

$$\epsilon_r = \epsilon' - i\epsilon'' = \epsilon' - i \frac{\sigma}{\omega \epsilon_0} \quad (2.5)$$

The real part of the relative permittivity ϵ' (for simplicity called real permittivity hereafter) of glacial ice is mostly influenced by the density ρ (in kg m^{-3}) and there are several empirical equations to describe this relation. Two that are commonly used are the relation by Kovacs et al. (1995) that is valid for dry snow, firn and ice:

$$\epsilon' = (1 + 0.000845 \rho)^2, \quad (2.6)$$

and the real-valued dielectric mixture equation by Looyenga (1965):

$$\epsilon'(z) = \left(\frac{\rho(z)}{\rho_{\text{ice}}} \left(\epsilon'_{\text{ice}}{}^{\frac{1}{3}} - 1 \right) + 1 \right)^3, \quad (2.7)$$

with the measured density $\rho(z)$ and the pure-ice values for density and real permittivity $\rho_{\text{ice}} \approx 917 \text{ kg m}^{-3}$ and $\epsilon'_{\text{ice}} \approx 3.15 - 3.17$, depending on temperature (Fujita et al., 1993)

The imaginary part of the relative permittivity (Eq. (2.5)) is responsible for the absorption of wave energy in the material. σ increases with increasing ice temperature, impurity content, and wave frequency (Plewes and Hubbard, 2001; Dowdeswell and Evans, 2004). The distribution of electric conductivity with depth can be measured on ice cores, e.g., with the dielectric profiling (DEP) method (Moore, 1993).

Polar ice is a low-loss medium with $\frac{\sigma}{\omega\epsilon_0} \ll \epsilon'$ and so the wave speed in ice is determined by the real permittivity ϵ' :

$$c = \frac{c_0}{\sqrt{\epsilon'}} \quad (2.8)$$

In glaciers and ice sheets, the density and thus the real permittivity increase from the snow surface downwards through the firn, until ρ_{ice} is reached. The increasing density causes a reduction in wave speed with depth (Eqs. (2.6)/(2.7) and (2.8)). The wave-speed-depth function can be inferred from a known density-depth profile, e.g., measured at an ice-core.

Due to the decreasing wave speed, the waves are refracted in normal direction (towards nadir) when traveling from the snow surface towards the bed and when crossing the air-ice interface (Snell's law). The increase in energy around the nadir from this focusing effect of the ice is called refraction gain q .

2.2 Electro-magnetic waves at interfaces

Whenever an electro-magnetic wave reaches an interface between materials of different electrical properties, i.e. conductivity or permittivity, its energy is partly reflected and partly refracted. The ratio of the reflected amplitude A_r to the initial amplitude A_i of the wave for a plane interface can be expressed by the amplitude reflection coefficient for perpendicular angles of incident:

$$R_A = \frac{A_r}{A_i} = \frac{\sqrt{\epsilon_{r1}} - \sqrt{\epsilon_{r2}}}{\sqrt{\epsilon_{r1}} + \sqrt{\epsilon_{r2}}} = \frac{n_1 - n_2}{n_1 + n_2}, \quad (2.9)$$

with the index numbers indicating the different materials. For negative R_A s, the reflected wave has a changed polarity compared to the incident wave (Navarro and Eisen, 2009). The reflected wave is the wanted signal of a horizon for the radar measurement. Equation (2.9) shows that the amplitude of the reflected wave is dependent on the difference in relative permittivity between the two media. Therefore, internal reflections from within the ice are generally weaker than the bed reflection, and a subglacial lake can be distinguished from bedrock.

RES data from regions with undisturbed, uniform ice flow in East Antarctica are characterized by a (sub-)parallel stratigraphy. The internal reflection horizons (IRHs) are often

continuous over long distances. The stratigraphy is (mostly) built up from paleo surfaces that got buried by new snow. These paleo surfaces move deeper down the ice column with a velocity that is determined by accumulation rate, basal melt rate, ice thickness and distribution of horizontal flow speed. Shallow IRHs are usually sub-parallel to the ice surface and align more and more with the bed topography when moving deeper in the ice column. The degree of this alignment depends on the wavelength of the topographic features (Hindmarsh et al., 2006). The reflections from within the ice, which form the horizontally continuous stratigraphy in the RES images, have three different causes (Bogorodsky et al., 1985; Dowdeswell and Evans, 2004).

1. Contrasts in density, and resultant contrasts in the real permittivity (Robin et al., 1969). These reflections occur mainly in the uppermost part of the ice column, above and in the firn–ice transition zone with typical depths ranging from 50–100 m on the EAIS (Cuffey and Paterson, 2010). The density differences arise from different properties of summer and winter precipitation and spatial variations in the densification process, e.g., due to different temperature or accumulation rate (Herron and Langway, 1980; Hörhold et al., 2011). Below the firn–ice transition zone the density stays approximately constantly that of ice, $\rho_{\text{ice}} = 917 \text{ kg m}^{-3}$, with slight variation depending on temperature and pressure (Cuffey and Paterson, 2010).
2. Conductivity contrasts (Paren and Robin, 1975; Millar, 1981). In the context of my thesis this is the most important reflection mechanism. It is responsible for the majority of IRHs below the firn–ice transition. The conductivity originates from acidity content that was deposited during precipitation events. The conductivity signals form paleo surfaces or, as seen in RES profiles, continuous horizons that are isochronous. The most distinct and widely distributed conductivity signals in East Antarctica originate from large volcanic eruptions. Beside the acids, the volcanoes emit tephra that can sometimes be seen as a dark layer in ice cores. Specific volcanic eruptions can be identified by analyzing the tephra composition. Tephra layers and acidic isochrones are thus important time markers that are used to tune ice-core age-depth scales and to correlate the age scales of different ice cores (Hammer et al., 1980). The reflection strength of conductivity contrasts in RES data is dependent on the measuring frequency (Fujita and Mae, 1994; Matsuoka et al., 1996).
3. Changes in ice fabric, caused by stress and strain in the ice (Harrison, 1973; Fujita et al., 1993). Being subjected to strain, the originally randomly distributed, intrinsically anisotropic ice crystals can align to a preferred orientation and form an anisotropic layer which is called crystal-orientation fabric (COF) layer. A few of such layers, seen as horizontally continuous IRHs in radar data, could be identified at the EPICA (European Project for Ice Coring in Antarctica) Dronning Maud Land (EDML) drill site by Eisen et al. (2007) and Diez et al. (2015). COF layers are not nec-

essarily isochronous and therefore not used for inferring the age-depth distribution in an ice sheet. Nevertheless, they are indicative of the stress regime in the ice and recent or former ice-flow dynamics.

2.3 Radio-echo sounding systems

Common RES systems consist of synchronized transmitter and receiver with respective antennas, a digital recording system with a transient recorder and digital storage, and a control unit. The central parts of the transmitter are a signal generator and a modulator. Receivers usually contain filters, a limiter to protect the system from strong signals and an amplifier with variable gain (Navarro and Eisen, 2009).

The received signal of reflections from different depths, caused by one transient source signal (one shot) is called a trace. The received amplitude (usually power P_r in dB with respect to transmitted power P_t) is recorded as a function of time after signal transmission. The time at which the signal arrives at the receiver antenna is the time the wave needs for propagating from the transmitting antenna to the respective reflector and back to the receiver antenna (see Fig. 2.1). It is thus called two-way travel time (TWT). To convert the information in the RES data from TWT domain to depth, knowledge or assumptions about the wave speed in the material are needed.

A reflection is detectable when the received reflection power is above the noise level. The ratio of received power to transmitted power from a plane reflector is:

$$\frac{P_r}{P_t} = \frac{G_t A_r q R_A^2}{16\pi z^2 L}, \quad (2.10)$$

with the antenna transmission gain G_t , the receiver-antenna area A_r , the refraction gain q , the amplitude reflection coefficient R_A , the distance between antennas and reflector z and the complete power loss in the two-way path L (Dowdeswell and Evans, 2004). The distance term describes the energy loss due to the spreading of the wave in three-dimensional space, called geometric spreading. The loss factor L includes reflection losses at the air-ice interface, transmission losses at the ice-bedrock interface, and attenuation in the ice by dielectric absorption and scattering.

For applications considered in this study, like measuring the ice thickness or IRHs throughout the entire ice column, measurements are made in common-offset configuration. Hereby, the antennas are installed in a fixed distance from each other, for instance under the aircraft wings or fuselage, and then moved over the ice. Traces are recorded at regular temporal or spatial intervals and plotted next to each other to get a horizontal profile of the depth information. This image is called a radargram, or sometimes also Z-scope image, compared to A-scope, which is the single trace. Figure 2.1 shows a sketch

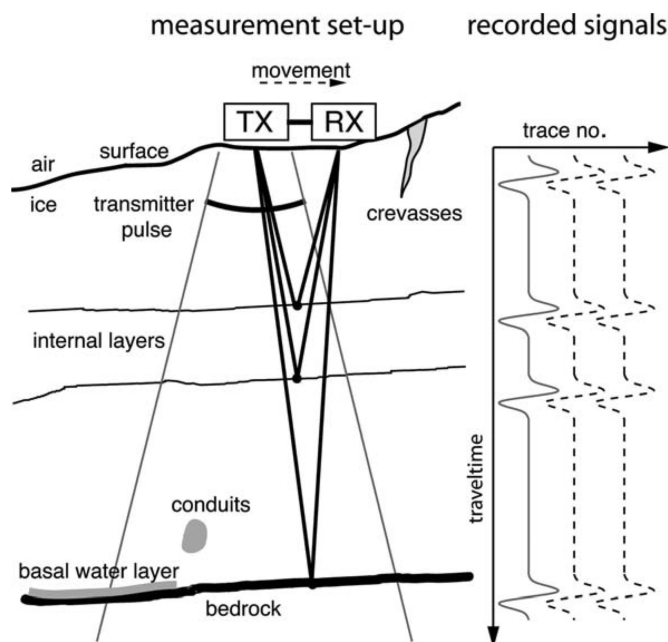


Figure 2.1. Sketch of RES measurements in common-offset configuration, borrowed from Navarro and Eisen (2009).

of ground-based RES measurements in common-offset configuration. The horizontal distance of the traces (horizontal sampling interval) is determined by the speed of the antenna movement and the signal repetition frequency. The transmitter and receiver antennas are close enough to assume normal incidence for horizontal reflectors. Other measurement configurations are the common midpoint configuration, where the distance of transmitter and receiver antennas is gradually increased and, if boreholes are available, a combination of one or both antennas being installed subsurface. These configurations can be used to accurately derive the wave-speed-depth functions, which, in turn, are needed for the TWT-to-depth conversion of the common-offset measurements.

There are different types of RES systems that are used depending on depth and size of the target structures and the measurement method. They are primarily differing in the kind of source signal they use. The earliest systems were airborne burst systems (sometimes also called pulse(d) systems). These systems are widely used for ice-thickness and IRH measurements on the polar ice sheets. The burst signals have of a certain frequency, the carrier frequency, which is amplitude modulated to produce the bursts. Typical carrier frequencies are between some tens of MHz and a few GHz. Burst lengths range from tens to hundreds of nanoseconds. Other systems use chirp signals. These signals have a

fixed pulse length during which the frequency runs through a defined frequency range. The chirp signals are characterized by their center frequencies f_c and bandwidths B . B is the width of the frequency range. Small pulse lengths for the burst and large bandwidths for the chirp systems, respectively, result in a high vertical resolution, often called range resolution, of the measurement. The advantage of the chirp systems over the burst systems is that pulse duration can be prolonged, facilitating the transmission of higher signal energies, without decreasing the range resolution. However, the data processing is costlier as pulse compression needs to be applied. Although the use of high frequencies for RES measurements is advantageous (for achieving higher resolution, needing smaller antennas, etc.), the frequencies cannot be increased to any height. Usually, there is a trade-off between resolution and penetration depth. For frequencies above approximately 150 MHz the absorption of wave energy by dielectric loss is increasing with frequency (Johari and Jones, 1976). Another factor is the enhanced volume scattering, further raising the total power loss by attenuation for higher measuring frequencies. Typical range resolutions of burst and chirp systems that can detect the bed reflection at ice thicknesses of up to 4 km are in the range of about ten to tens of meters.

For temperate ice or small valley glaciers it is often beneficial to increase the directivity of the measurements, to reduce clutter signals from the inhomogeneous ice or the valley sides. This can be accomplished with a decreased pulse length by using impulse (or mono-cycle) radars, transmitting a signal consisting of only approximately one cycle, frequency modulated (FMCW radar), or stepped frequency source signals. These systems can achieve a very good vertical resolution, depending on the frequencies they use. However, their performance regarding penetration depth remains behind the burst systems. Apart from applications on temperate ice they are often used to investigate density variations in snow and firn of the polar ice sheets, down to depths of a few hundred meters.

More recent development in the RES technique in glaciology goes towards multi-channel and coherent signal recording, which facilitates synthetic-aperture post-processing as known from synthetic-aperture radar (SAR) satellites. With this technique, the horizontal and vertical resolution can be increased in the post-processing, and even 3D images can be produced with measuring only one profile.

2.4 RES data and processing

My thesis is based on the RES data that were collected by colleagues from the Alfred Wegener Institute (AWI) during the last two decades. Additionally, I used some data from other institutes, for comparison in my first publication, and to enlarge the covered area in the other two parts. Due to the location of the German Neumayer Station, the logistic base for most of the RES surveys, and the deployment of the AWI RES system

for the EDML ice core pre-site survey, the AWI data are concentrated in Dronning Maud Land (DML). A few surveys were also flown outside of DML. Those start at the EPICA Dome C (EDC) drill site and, among others, connect the EDC and Vostok drill sites and continue to Dome A (DA), the highest point of the EAIS. Figure 2.2 gives an overview of East Antarctica with the deep drill sites, other place names and the RES profiles used in the thesis. The RES data and surveys are described in detail in the chapters where they are used. In Fig. 2.2, I just give the short names for orientation.

The paragraphs below describe the specifics of the RES systems, the basic processing and the bed and IRH tracing for the AWI RES data. Specific characteristics or different processing of any additional data that are used are described in the respective chapters.

The airborne radar system of the AWI is a burst system with a carrier frequency of 150 MHz that can be operated in toggle mode with 60 ns and 600 ns burst lengths. This corresponds to approximately 5 m and 50 m range resolution in ice, respectively (Nixdorf et al., 1999). In toggle mode, the burst length alternates between the shots, generating one radargram with higher range resolution and one with lower range resolution but higher penetration depth for each profile. The 600 ns data are used for ice-thickness measurements, the short-pulse data are used for IRH interpretation. Before interpreting the data, some basic processing needs to be applied, which was done with the commercial seismic-processing software application FOCUS (Paradigm). First, the data are stacked to an average trace distance of about 75 m for noise reduction. In a second step, the data are differentiated to enhance the contrasts of the reflections in the radargram image. Furthermore, an automatic gain control filter is applied in the vertical (TWT) direction, to partly compensate for the larger geometric-spreading and attenuation losses deeper in the ice column. Depending on application, different band-pass filters are applied to increase the visibility of the reflections of interest. The surface and bedrock tracing was conducted continuously during over 20 years of surveying by several colleagues with the FOCUS software. The exact procedure with example figures is, e.g., described in Bellot (2012). The last processing step before IRHs are traced and interpreted is to shift the surface reflection to a certain TWT in all traces, resulting in a flat surface in the radargram. This ensures a consistency of surface, bed and internal reflections at the crossover points of different profiles.

Processed as described, the data are loaded into the commercial seismic-processing software package Landmark (Halliburton) for the tracing procedure. The software allows for semi-automatic tracing, where manual picks can be set and are then automatically connected by searching for the maximum, minimum, or zero-crossing within a certain time window around the manual picks in the neighboring traces. In that way, the IRHs can be traced along the RES profiles and transferred from one profile to another at the crossover points of the profiles. The transfer is facilitated by the Landmark software by marking the

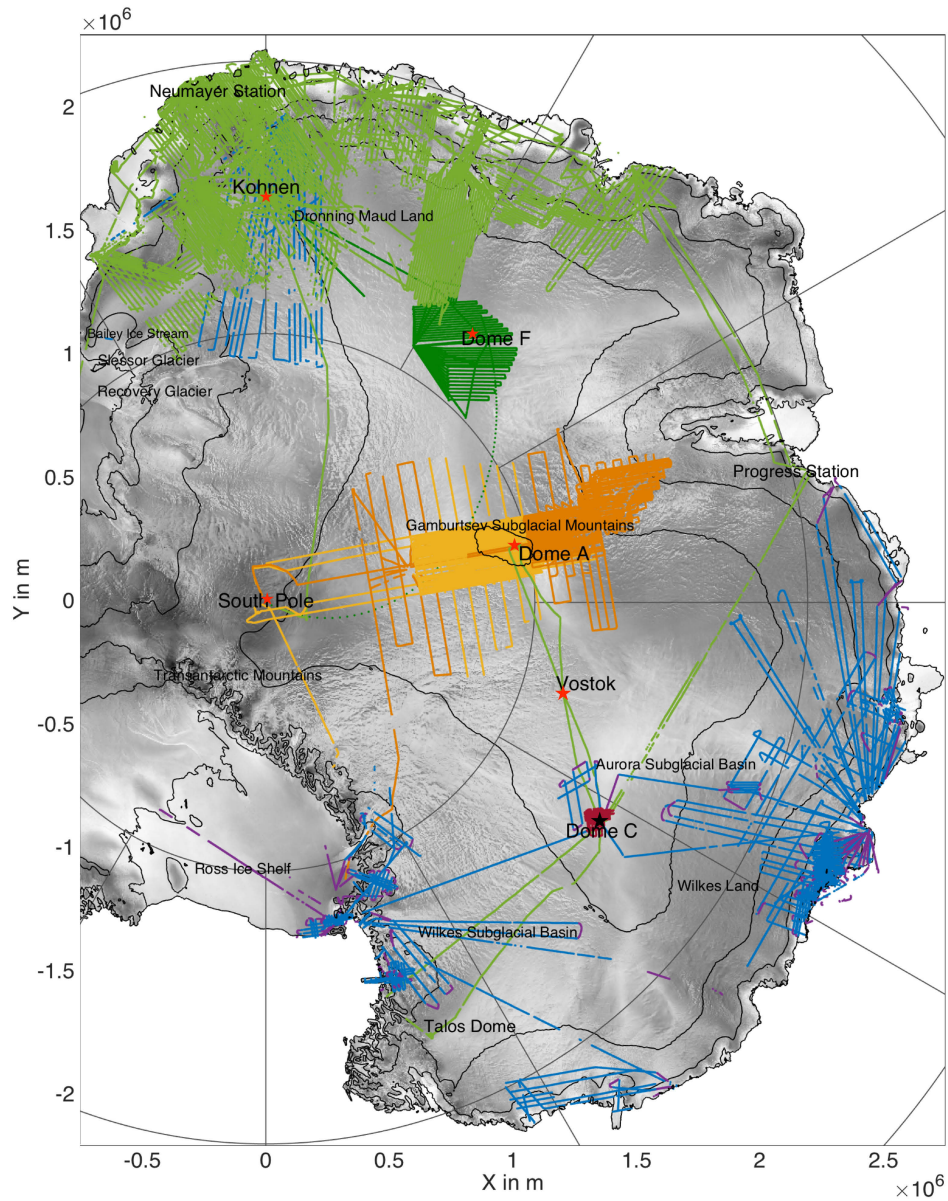


Figure 2.2. Overview of East Antarctica with important place names, drill sites, and the RES profiles used in this thesis. The axes are Antarctic Polar Stereographic coordinates. Green lines indicate the AWI RES profiles (dark green is the latest AWI survey OIR). Orange lines are AGAP data (bright: AGAP-South, dark: AGAP-North), blue lines are Operation IceBridge data from the ICECAP project, and red lines are the profiles of the OIA survey from the ICECAP II project.

TWTs of IRHs traced in crossing profiles (see Fig. 2.3) and by the possibility to display two profiles in a composite view, with the location along the profile shown in a separate window (Fig. 2.4).

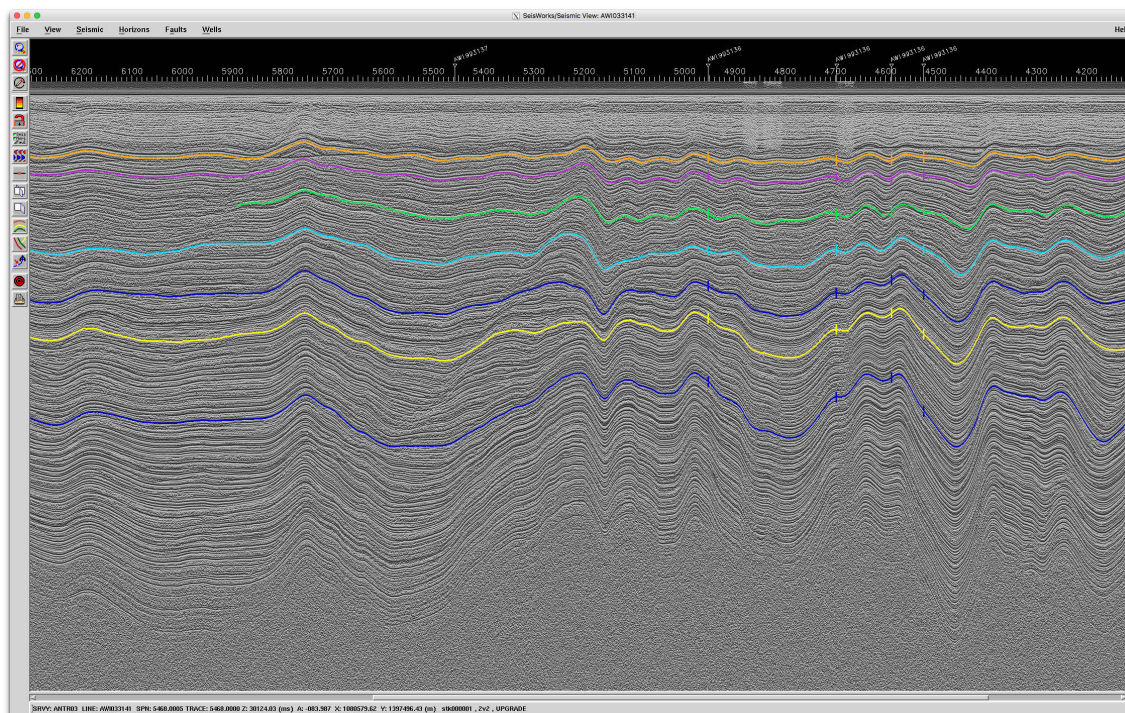


Figure 2.3. Example radargram in the Landmark processing software during the procedure of IRH tracing. Colored lines are traced IRHs, vertical ticks indicate where the respective IRHs are picked in crossing profiles. The names of the crossing profiles are written at the top of the radargram.

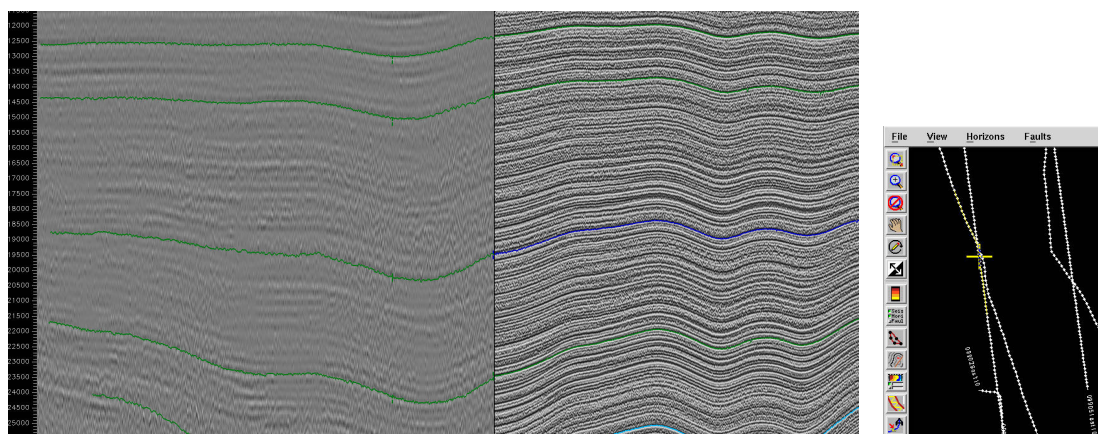


Figure 2.4. Two radargrams displayed next to each other in the Landmark processing software during the transfer of IRHs from one profile to another. The radargrams are compound at their crossing location. The cross in the small window indicates the location of the cursor in the profiles (dotted lines).

These features also provide the means for a independent control of the tracing, whenever there are full circles of profiles like for a gridded survey design. When a RES profile passes

the drill site of an ice core, the RES data can be converted from TWT to depth domain with an accurate wave-speed-depth function, derived from density measurements on the ice core and Eqs. (2.6)/(2.7) and (2.8). The traced IRHs can then be assigned with their age from the ice-core age scale. This approach is described in detail in Chap. 4.

3 Publication synopsis

The aim of this study is to establish a comprehensive interpretation of the interior of the EAIS, with respect to stratigraphic architecture, basal properties and ice-flow dynamics. The study is structured in three parts, investigating different aspects that are relevant for achieving this aim. The first part is focused on methodological questions. The second and third parts use the insights from the first part for a large-scale mapping of the age stratigraphy and basal properties of the EAIS and address what can be inferred thereof about the ice-sheet dynamics. The following three chapters (Chap. 4, 5 and 6) are my first-author contributions (to-be) to scientific journals and describe the science and outcomes of the different working parts. Furthermore, I contributed to another study, published in the journal *Frontiers in Earth Science* (Karlsson et al., 2016). The study has some common methods with my first two publications, but a different study area (Greenland) and time scale. As it is unrelated to the topic of my thesis, I will not include it here. The sections of this chapter (Sect. 3.1, 3.2 and 3.3) highlight the strategy of my thesis and give the motivation and results of the different working steps. Furthermore, the contributions of the different authors to the journal contributions are listed. To facilitate the readability and comprehension of these short overviews, any references are not given in this chapter, but only in the respective publication chapters. Specific RES data sets that are mentioned in the sections below are described in more detail in the respective publication chapters.

3.1 Paper I: Comparison of measurements from different radio-echo sounding systems and synchronization with the ice core at Dome C, Antarctica

by Anna Winter, Daniel Steinhage, Emily J. Arnold, Donald D. Blankenship, Marie G. P. Cavitte, Hugh F. J. Corr, John D. Paden, Stefano Urbini, Duncan A. Young, and Olaf Eisen published in *The Cryosphere* in March 2017 (Winter et al., 2017).

This first work package addresses some methodological questions that arise when interpreting RES data to obtain the internal stratigraphy of the ice sheet, and when moving

from local-scale interpretation to regional or even continental scales. Combining different RES data and accurate dating of IRHs is imperative for establishing a large-scale mapping of the age structure of the EAIS, where no reasonable coverage or resolution is obtained with only one data set. For these reasons, the questions of how combinable the different RES data are and if they all depict the englacial structure in the same way are addressed. We compile the data of five different RES systems from the research institutes that represent the main contributors of RES data from East Antarctica and compare the various systems' strengths and weaknesses. All data are recorded in close vicinity to the EPICA Dome C (EDC) drill site. Furthermore, we calculate a synthetic radar trace with the existing model 'emice', using density and conductivity measurements from the EDC ice core, to relate the IRHs to ice properties. We find that the IRH structure can be transferred between the data. A critical factor for a smooth transfer of IRHs between different data is the similarity of the systems' range resolution. By synchronizing IRHs in the measured RES traces with those in the synthetic trace and by conducting sensitivity studies with the conductivity profile, the exact depth and the reflection cause of the RES IRHs can be identified. They can be assigned with their age from the ice-core age scale. This method of age assignment has the advantage of only small uncertainties that are independent of IRH depth. Because the IRHs synchronized with the conductivity profile are definitely caused by conductivity contrasts, it is ensured that they are isochronous paleo surfaces. As the EDC ice core yielded the oldest continuously dated ice so far, this study is a good basis for tracing the oldest possible isochronous IRHs.

I processed the RES data collected by the Alfred Wegener Institute (AWI), selected the data from other resources and compiled all data, ran the (already available) model 'emice', tested different parameters and source wavelets, matched the IRHs with different methods, conducted the sensitivity studies, created the figures, and wrote the manuscript. **Daniel Steinhage** collected the AWI RES data, is responsible for RES-data storage and quality control, and proof-read the manuscript. **Olaf Eisen** developed the 1D finite-differences model 'emice' for calculating synthetic radar traces, introduced me to the other coauthors, provided scientific input, and supervised the work. All **other coauthors** provided RES profiles and proof-read the manuscript.

3.2 Paper II: Deducing large-scale age distribution and paleo-accumulation rates from radiostratigraphy in East Antarctica

by Anna Winter, Thomas Kleiner, Daniel Steinhage, Timothy T Creyts, and Olaf Eisen
in review for the Journal of Glaciology since November 2017.

In this second study, a large-scale age-depth stratigraphy of the EAIS is established, using the knowledge from the first study about the nature of RES IRHs, age assign-

ment on IRHs, and compatibility of RES data from different systems. We use RES data from various regions in East Antarctica and trace at least two isochronous IRHs continuously along all profiles. The stratigraphy is further used to derive first-order estimates of accumulation-rate distribution, locations of changing ice-flow characteristics and the maximum age of basal ice. Such an IRH stratigraphy is of great value to provide boundary conditions or parameters for continental ice-flow models. In combination with model results from the state-of-the-art ice-sheet model PISM (Parallel Ice Sheet Model) we derive paleo-accumulation rates from the traced IRHs. The comparison of the results with accumulation rates from ice-core measurements and other studies show that the method's underlying assumptions are too simplified to be applicable on an ice-sheet-wide scale.

I selected and compiled all data, transferred IRHs between different data sets, traced the IRHs in the Antarctica's Gamburtsev Province Project (AGAP)-South data set, calculated IRH depths and accumulation rates, created all figures, and wrote the manuscript. **Thomas Kleiner** ran the PISM model, contributed to the modeling section (Sect. 5.3.3), supported the interpretation of the model results, and proof-read the manuscript. **Daniel Steinhage** collected the AWI data, is responsible for data storage and quality control, traced the IRHs in the AWI data, and proof-read the manuscript. **Timothy T. Creyts** provided the AGAP-South data and proof-read the manuscript. **Olaf Eisen** provided scientific input, contributed to the discussion section (Sect. 5.5), and supervised the work.

3.3 Paper III: Basal roughness of the East Antarctic Ice Sheet and its indications for ice flow and basal thermal state

by Anna Winter, Daniel Steinhage, Veit Helm, and Olaf Eisen

manuscript in preparation, to be submitted within the next few weeks

This third part focuses on the subglacial bed properties of the EAIS. On the one hand, the ice-sheet bed is molded by past ice flow, on the other hand, its shape, solidity and thermal condition greatly influence the present and future ice dynamics. A thorough evaluation of the ice-sheet bed can thus inform about the ice-sheet history, as well as improve the sea-level projections from ice-flow models. In this study, we investigate the subglacial bedrock properties by statistical roughness analyses of the bed topography, derived from ice thickness measurements from a large RES data set combined from measurements of different institutes. The roughness analysis enables a classification of the subglacial landscape below the EAIS, with respect to evolution and erosion history. Relationships between roughness, ice-flow velocities and basal temperatures are observed, which, if confirmed by more tests and measurements, would facilitate inferences about the basal thermal state of the ice sheet, solely using ice-thickness measurements. This method could be

a valuable tool for validating the basal thermal state from modeling, which is currently the only means for obtaining basal temperatures apart from a few point measurements at ice-core drill sites. The thermal state, bedrock material and bed roughness determine the occurrence and magnitude of basal motion, the sum of the deformation of subglacial bed material and the sliding of the ice over the bed. Basal motion is that part of total flow speed that changes most rapidly with presence and absence of subglacial water and can therefore facilitate rapid variations in ice-stream configuration and the mass balance of the EAIS. The basal roughness is readily accessible information and could, in combination with a hydrological model, lead to a sliding-behavior parametrization for continental ice-sheet models. This could diminish the uncertainty on East-Antarctic contribution to future sea level.

I compiled all data, implemented the roughness parameter calculation, analyzed and interpreted the results, created all figures, and wrote the manuscript. **Daniel Steinhage** collected the AWI data, is responsible for data storage, quality control and the tracing of the bed reflection in the AWI data, and proof-read the manuscript. **Veit Helm** implemented and applied the auto-picker routine (see Sect. 6.2.1) and provided scientific input. **Olaf Eisen** brought the work of Jordan et al. (2017) (which this study is based on) to my attention, provided scientific input, and supervised the work.

4 Comparison of measurements from different radio-echo sounding systems and synchronization with the ice core at Dome C, Antarctica

This chapter is published in *The Cryosphere* (Winter et al., 2017).

Abstract

We present a compilation of radio-echo sounding (RES) measurements of five radar systems (AWI, BAS, CReSIS, INGV and UTIG) around the EPICA Dome C (EDC) drill site, East Antarctica. The aim of our study is to investigate the differences of the various systems in their resolution of internal reflection horizons (IRHs) and bed topography, penetration depth and capacity of imaging the basal layer. We address the questions of the compatibility of existing radar data for common interpretation and the suitability of the individual systems for reconnaissance surveys. We find that the most distinct IRHs and IRH patterns can be identified and transferred between most data sets. Considerable differences between the RES systems exist in range resolution and depiction of the bottom-most region. Considering both aspects, which we judge as crucial factors in the search for old ice, the CReSIS and the UTIG systems are the most suitable ones. In addition to the RES data set comparison we calculate a synthetic radar trace from EDC density and conductivity profiles. We identify 10 common IRHs in the measured RES data and the synthetic trace. We then conduct a sensitivity study for which we remove certain peaks from the input conductivity profile. As a result the respective reflections disappear from the modeled radar trace. In this way, we establish a depth conversion of the measured travel times of the IRHs. Furthermore, we use these sensitivity studies to investigate the cause of observed reflections. The identified IRHs are assigned ages from the EDC's timescale.

Due to the isochronous character of these conductivity-caused IRHs, they are a means to extend the Dome C age structure by tracing the IRHs along the RES profiles.

4.1 Introduction

To predict the future evolution of ice sheets, the knowledge of their past response to climate changes is inevitable. Ice cores are valuable archives to study the climate of the past (EPICA community members, 2004). In contrast to other climate archives, they contain actual paleo-atmosphere in the form of air bubbles and hydrates that are trapped in the ice. With this advantage, they are the only means to answer some important questions in climate studies with respect to greenhouse gases: e.g., why did the glacial–interglacial cycles change from 40 to 100 ka at the mid-Pleistocene transition (MPT) and what drove the 40 ka cycles (Raymo et al., 2006)? For this reason the International Partnerships in Ice Core Sciences (IPICS) included the retrieval of the “Oldest Ice” ice core as one of their scientific goals (Brook et al., 2006). This core should contain a continuous ice-core record over at least 1.2 Ma, preferably 1.5 Ma, at some distance above the ice–bedrock interface. As compared to the oldest continuous ice currently on record (retrieved at Dome C (EPICA community members, 2004) and has an estimated age of 800 ka), this future core is supposed to include the MPT and some 40 ka cycles.

There are only few promising regions for such an Oldest Ice ice core, all of them located close to dome or saddle positions on the East Antarctic Plateau (Fischer et al., 2013). As many conditions have to be fulfilled at a site for old ice to exist and, equally important, to be retrievable in an analyzable way, extensive pre-site surveys are necessary to fill in gaps in the already existing data sets. Of great importance are not only ice thickness and internal structure but also surface and basal mass balance, ice-flow history, as well as temperature profile and geothermal heat flux. Since not all of these parameters are easy to determine in the field, modeling studies will be engaged to constrain upper and lower bounds on parameters which cannot be measured. Radio-echo sounding (RES) is a widely used method to investigate accumulation, ice thickness and internal structure (e.g., Urbini et al., 2008; Rodriguez-Morales et al., 2014; MacGregor et al., 2015a). Variations in density, conductivity or crystal-orientation fabric (COF) cause the partial reflection of electro-magnetic wave energy and thus appear as internal reflectors (internal reflection horizons, IRHs) in radargrams. The IRHs from changes in density and conductivity are formed at the same time near the surface (Vaughan et al., 1999; Dowdeswell and Evans, 2004) and then advected by compaction and ice flow. Density variations are the primary cause of IRHs in the uppermost few 100 m of the ice sheet but do not occur in deeper parts (Millar, 1981). The IRHs from conductivity changes, in contrast, can be found throughout the ice sheet. The reflection coefficients of those IRHs are related

to changes in the imaginary part of the complex dielectric permittivity and are proportional to conductivity changes and inversely proportional to frequency. A change of COF is the second reason for reflections in the deeper parts of the ice column, predominating in zones of high shear. In RES measurements the conductivity-based IRHs can be distinguished by the frequency dependence of their reflectivity from IRHs caused by COF and density, which have frequency independent reflection coefficients related to changes in the real part of the complex permittivity (Fujita et al., 1999, 2000). Conductivity itself was assumed frequency independent in the range of RES frequencies, but more recent work implies that its frequency dependence cannot be neglected for, e.g., attenuation studies (MacGregor et al., 2015b).

RES data provide information about the englacial age structure away from any ice core. The isochronous conductivity-based IRHs can be traced continuously over long distances in the ice sheets (e.g., Steinhage et al., 2013) and thus be used for extrapolating the age-depth distribution from ice cores along the RES profiles. In comparison with ice core data sets this larger amount of information about the age structure of ice sheets is useful for the evaluation of ice-flow models and an important criterion at the current stage of the models (Sime et al., 2014). Furthermore, IRHs are used to directly derive ice dynamics (e.g., Karlsson et al., 2012; Winter et al., 2015) and attenuation rates, whereof depth-averaged temperatures can be obtained (Matsuoka et al., 2010; MacGregor et al., 2015b; Jordan et al., 2016).

The great value of RES data for the investigation of the ice sheets has led to numerous campaigns with gradually more sophisticated radar systems over the decades. Due to the variety of differently motivated surveys and the rapid technical development, the data of one particular radar system usually are confined to a more or less small area. Therefore it is inevitable to combine data of different systems when working on larger-scale or even ice-sheet-wide problems. For example, Cavitte et al. (2016) use data of two different radar systems to obtain a continuous connection of the East Antarctic deep drill sites Dome C and Vostok and a third system for an alternative connecting route and separate quality control. Searching for the oldest ice, it would be beneficiary to include the existing measurements of even more radar systems. However, it is not clear nor has it been investigated whether the data, measured with different radar systems at different times and having different characteristics, are comparable and can be assembled to one data set suitable for this purpose or if there are less confinable data sets.

In this study we address these questions and, for the first time, compile the data of five different RES systems, all recorded in close vicinity to the EPICA Dome C (EDC) drill site, for comparison of the various systems' strengths and weaknesses. Furthermore, we calculate a synthetic radar trace, using the EDC ice core profiles of density and conductivity, as established by Eisen et al. (2004) and Eisen et al. (2006) to relate the radar measurements

to ice properties. The modeled radar trace is also used for an accurate depth inversion and thus reliable age assignment of 10 horizons, identified in the RES data. As the EDC core yielded the oldest continuously dated ice so far, it is a good starting point for tracing the oldest possible layers.

4.2 Synthetic radar traces

To relate measured RES data to the physical properties and age of the ice, synthetic radar traces are calculated from measured ice core data. The modeled traces are then compared to the measured RES data with respect to the questions of depth origin and nature of the RES reflections. In the sections below we describe the ice core data used for calculating the synthetic traces (Sect. 4.2.1) and the actual modeling (Sect. 4.2.2). In Sect. 4.2.3 we describe how we derive the value for the permittivity of ice that we use in all further proceedings.

4.2.1 Ice core data

We use the records of the second EDC ice core (EDC99) that was drilled in the austral seasons 2000–2004. The drill site is located on the East Antarctic Plateau at 123.35° E and 75.10° S, 3233 m above sea level. It has a yearly accumulation rate of 25 kg m⁻² a⁻¹ and a mean annual surface temperature of -54.5°C. The ice thickness at this location is 3309 ± 22 m (The EPICA Dome C 2001-02, science and drilling teams, 2002). In 1999, the first drilling attempt had to be abandoned because the drill got stuck at a depth of almost 800 m. In the second attempt a depth of 3260 m was reached, with only a few meters missing to the bedrock (EPICA community members, 2004). The core was dated back to roughly 800 ka BP by, e.g., Bazin et al. (2013) and thus comprises the oldest continuously retrieved ice to date.

Dielectric profiling (DEP; Moore, 1993) measurements on the core were conducted in the field at temperatures of $-20 \pm 2^\circ\text{C}$ and a frequency of 100 kHz. The data set consists of conductivity values (σ in S m⁻¹) for the depth range of 6.80 m to 3165.20 m with a resolution of 0.02 m. The data were corrected to a temperature of -15°C and cleaned of data points where the core was broken (Parrenin et al., 2012; NOAA, 2011). The record is extended up to the surface by linear interpolation to a value of 4.05 μS m⁻¹. Gaps due to removed data points are also linearly interpolated and the record is linearly resampled to 5 mm.

The density (ρ in kg m⁻³) of the EDC99 core was measured with the γ -absorption method, which is also described in Eisen et al. (2006), at the Alfred Wegener Institute, Bremerhaven, Germany, for the depth range of 6.80 m to 112.70 m in 1 mm increments (Hörhold et al., 2011). Gaps in the record are linearly interpolated and the record is also

resampled to 5 mm. For depths outside the measurement range the density is logarithmically extrapolated up to the density of ice, $\rho_{\text{ice}} = 917 \text{ kg m}^{-3}$.

The records for density and conductivity are then combined to one record of depth, density and conductivity from the surface to 3165.2 m depth in 5 mm increments.

4.2.2 Electro-magnetic modeling of radar traces

Radar measurements are recorded in the two-way travel time (TWT) domain. The reflection peak of a reflector of a certain depth is recorded after the time a transmitted wave needs to travel to the reflector and back again. To convert the depth profile of our combined ice core record to the TWT domain of the RES data, we need the depth-dependent electro-magnetic wave speed in firn and ice,

$$c(z) = \frac{c_0}{\sqrt{\varepsilon'(z)}}, \quad (4.1)$$

with the vacuum wave speed c_0 and the real part ε' of the complex relative dielectric permittivity,

$$\varepsilon = \varepsilon' - i\varepsilon'' = \varepsilon' - i\frac{\sigma}{\varepsilon_0\omega}, \quad (4.2)$$

where σ is the conductivity, ε_0 the vacuum permittivity and ω the circular frequency. For readability we use “permittivity” hereafter for the real part of the complex permittivity (ε').

As the accuracy of the DEP measurement performed at EDC does not allow for an inversion of the complex-valued permittivity of a two-phase mixture, as described by Eisen et al. (2006), we use the real-valued dielectric mixture equation by Looyenga (1965) to calculate $\varepsilon'(z)$ from $\rho(z)$:

$$\varepsilon'(z) = \left(\frac{\rho(z)}{\rho_{\text{ice}}} \left(\varepsilon'_{\text{ice}}{}^{\frac{1}{3}} - 1 \right) + 1 \right)^3, \quad (4.3)$$

with the measured density $\rho(z)$ and the pure-ice values for density and permittivity $\rho_{\text{ice}} = 917 \text{ kg m}^{-3}$ and $\varepsilon'_{\text{ice}} = 3.17$. In Sect. 4.2.3 we describe how we derived the value for the permittivity of ice for our study. Below the depth, where the density of ice is reached we use the constant permittivity $\varepsilon' = \varepsilon'_{\text{ice}}$. It should be noted at this point that only conductivity-caused reflections and no permittivity-caused (i.e., COF and density-based) reflections can be modeled in this way (Fujita and Mae, 1994). Neglecting the complex character of the relative permittivity in the two-phase mixture leads to errors in the complex permittivity, especially in the firn (Wilhelms, 2005). However, for the purpose of reproducing the signature of the conductivity-caused IRHs as measured by radar, not the

absolute value but the changes of conductivity are important. Though reflections occur at the wrong TWTs in the synthetic trace when incorrect real permittivities are used in the model, we avoid these errors by calibrating the synthetic with the measured radar trace (see Sect. 4.2.3).

The permittivity record is smoothed with a 0.2 m running mean to prevent the masking of the conductivity-induced reflections and the too quick reduction of the propagating energy in the synthetic radar trace by a multitude of permittivity-induced reflections in the firn section. More extensive reasoning and effects of this procedure can be found in Eisen et al. (2006).

Permittivity and conductivity, processed as described above, are input parameters for the 1D-FD (One-Dimensional Finite Difference) version of the model “emice” (Eisen et al., 2004) that calculates synthetic radar traces by solving Maxwell’s equations. The depth increment of the model domain is 0.02 m. The maximum depth is 3165.20 m and an absorbing boundary is implemented in the depth direction. The time increment is 0.02 ns, which fulfills the Courant criterion that ensures the stability of the numerical calculations (Courant et al., 1928; Taflove and Hagness, 1995).

Following Eisen et al. (2006), we use a source wavelet of two and a half 150 MHz cycles. It should be noted here that, for simplicity, this wavelet is based on the burst and pulse radar systems rather than the chirp systems, which require additional post-processing like pulse compression (Sect. 4.3). However, this synthetic pulse is much shorter and the wavelet is not identical to any of the RES system ones. We chose it as trade-off between being long enough to reproduce some interference effects and being relatively short for determining reflector depth in sufficient resolution.

The envelope of the calculated trace corresponding to the reflected energy is obtained by conducting a Hilbert magnitude transformation (Hilbert, 1906; Taflove and Hagness, 1995). Finally, the trace is smoothed with a Gaussian running mean of 100 ns. The result of this step is the synthetic trace that we use for comparison with the measured RES data, as described in Sect. 4.5.

4.2.3 Assessing the permittivity of ice

To calculate the correct TWTs for reflectors in our synthetic radar trace we have to use the correct permittivities. For permittivities that are too small the wave speed is too high and a distinct reflection does thus appear too early (Eq. 4.1). This time shift increases with the absolute depth of the reflector. As the real permittivity could not directly be measured at Dome C, we are looking for an average value for the permittivity below the firn–ice transition ϵ'_{ice} that best reproduces the reflection TWTs compared to measured RES data. Above the firn–ice transition we use measured densities to calculate permittivities, as

described in Sect. 4.2.2. As reference RES data we choose the AWI data for their small distance to drill site, high vertical resolution and being a burst system which is closer represented by the source wavelet of the model than the chirp systems (see Sect. 4.3 on RES data). Note that it is not our aim to get the exact value of ϵ'_{ice} but rather a good estimate with this method, so we can easily match reflection peaks of all measured RES data with the synthetic trace in a later step. The exact permittivity is not needed throughout our study because we do not use a velocity function to calculate the depths of RES IRHs but a sensitivity study with the synthetic trace (Sect. 4.5.3).

With the trial-and-error method we compare the synthetic traces of model runs with different ϵ'_{ice} to the AWI trace, starting with the commonly used value of $\epsilon'_{\text{ice}} = 3.15$ (e.g., Rodriguez-Morales et al., 2014). We compare the TWTs of 10 distinct reflections distributed between approximately 2.3 and 24.3 μs TWT between synthetic and AWI trace. This synthetic trace shows smaller TWTs than the measured one, with increasing time lags towards greater TWTs. For this reason we repeat the procedure with an ϵ'_{ice} increased by 0.01, and so on. The best result is obtained with $\epsilon'_{\text{ice}} = 3.17$ for which we do not get TWT lags that are systematically changing with increasing TWT between synthetic and measured radar traces and for the compared IRHs. Therefore we conclude that 3.17 is a suitable estimate for ϵ'_{ice} in our study region and we will use the synthetic trace calculated with this value for our further proceedings. This value is also found reasonable by Bohleber et al. (2012) for slightly anisotropic configurations and is close to the pure isotropic ice value of $\epsilon'_{\text{ice}} = 3.16$ found in their laboratory experiments.

4.3 Radio-echo sounding data

The profiles closest to the drill site were selected from the RES data available in the Dome C area. The distance between the drill site and the furthest profile is less than 2 km. The positions of the RES profiles relative to Dome C are shown in Fig. 4.1. As the influence of different radar systems on the recorded radargram is to be examined, we use the data of five different institutes: the Alfred Wegener Institute (AWI), Bremerhaven, Germany, the British Antarctic Survey (BAS), Cambridge, UK, the Center for Remote Sensing of Ice Sheets (CReSIS) at the University of Kansas, Lawrence, USA, the Istituto Nazionale di Geofisica e Vulcanologia, Rome, Italy (INGV), and the University of Texas Institute for Geophysics (UTIG), Austin, USA. The characteristics of the different systems and the data processing are described next. The system characteristics are summarized in Table 4.1.

4.3.1 AWI

The airborne radar system of AWI is a burst system with a carrier frequency of 150 MHz that was operated in toggle mode with 60 and 600 ns bursts (Nixdorf et al., 1999). Measurements were conducted in austral season 2007/08 with the DC-3T aircraft Polar 5. We

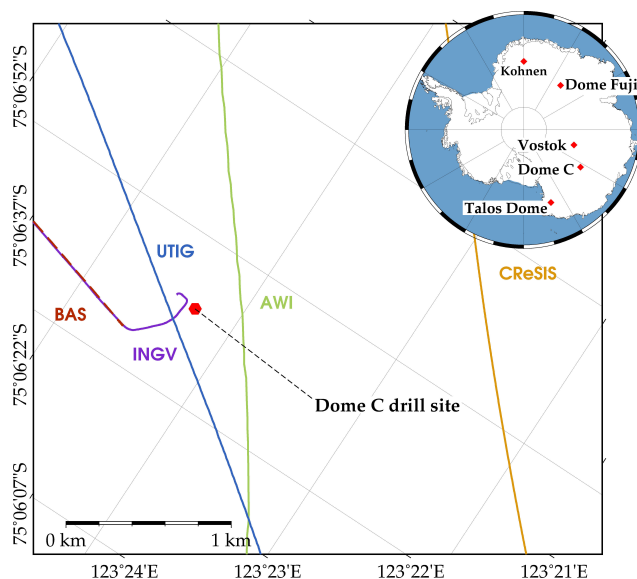


Figure 4.1. The deep drill sites in East Antarctica and close-up to Dome C with the RES profiles. The crosses mark each profile's closest trace to the drill site. The location of the EDC drill site is marked by the red hexagon.

use the data with 60 ns bursts and stack them 10-fold. The stacked data have a trace distance of about 75 m and a vertical sampling interval of 13.33 ns. The profile passes the Dome C drill site at a distance of 280 m.

4.3.2 BAS

The BAS profile was recorded in season 2005/06 with an airborne radar system on a Twin Otter in 450 m distance to the drill site. The source is a 4 μ s chirp wavelet with a center frequency of 150 MHz and a bandwidth of 10 MHz. The vertical sampling interval is 45.45 ns. The data are chirp compressed and a horizontal smoothing with a 49 sample moving-average filter and 10-fold stacking is applied. The trace distance after stacking is 45 m.

4.3.3 CReSIS

CReSIS had one campaign in the Dome C area in season 2013/14, using the Multi-Channel Coherent Radar Depth Sounder (MCoRDS) on an Orion P3 aircraft (Rodriguez-Morales et al., 2014). The source wavelets are 1, 3 and 10 μ s chirps, each running linearly through the frequency range of 180 to 210 MHz (Gogineni, 2012). We use the L1B-data CSARP_standard file, processed with pulse compression, focused SAR processing and array processing with multilooking (CReSIS, 2016). The final product has a vertical sampling interval of 33 ns and a trace distance of 30 m. The profile passes the drill site at 1745 m distance.

Table 4.1. Characteristics of the five RES systems. The fourth column gives either the bandwidth B in case of the chirp systems or the pulse length in case of the pulse and burst systems. The sixth column gives the vertical resolution due to bandwidth (for distinguishing two reflectors), determined as $\frac{kc_0}{2B\sqrt{3.17}}$ for the chirp systems. For the window widening factor k we use 1.53, as given in CReSIS (2016). Further details on data recording and processing can be found in the referenced papers where the data are published.

System	Aircraft	Center freq. (MHz)	Bandwidth/pulse length	Vertical sampl. freq. (MHz)	Vertical resolution (m)	Horizontal sampl. distance (m)
AWI	DC-3T	150	60 ns	75	5.1	75
BAS	Twin Otter	150	10 MHz	22	12.9	45
CReSIS ¹	Orion P3	195	30 MHz	30	4.3	30
INGV ²	Ground based	150	200 ns	25	16.6	2
UTIG ³	DC-3T	60	15 MHz	50	8.6	22
Modeled ⁴	–	150	0.2 ns	1000	8.4*	–

* The vertical resolution of the synthetic data is controlled by the filtering of the trace as described in Sect. 4.2.2.

¹ CReSIS (2016), ² Urbini et al. (2015), ³ Cavitte et al. (2016), ⁴ Eisen et al. (2006)

4.3.4 INGV

The INGV profile was measured in December 2011 during a test of a 200 ns pulse radar system with a carrier frequency of 150 MHz, recording the envelope only. The horizontal trace distance is about 0.25 m and the vertical sampling interval is 40 ns. The 2.7 km long profile passes the drill site in 65 m distance. Spiking deconvolution, low pass filtering and gain adjustment are conducted. We stack the data 10-fold.

4.3.5 UTIG

The radar profile of the UTIG was collected with the High-Capability Radar Sounder (HICARS) in season 2008/09 from a DC-3T aircraft in 150 m distance to the drill site. The system uses a 1 μ s chirp wavelet running linearly through the frequencies from 52.5 to 67.5 MHz. The HICARS system is described in Peters et al. (2005) and the SAR processing in Peters et al. (2007). The recorded data were filtered with a 10 MHz band notch filter and a convolution. An automatic gain control is conducted and the data are stacked horizontally coherently 10 times, log detected and incoherently stacked five times so the final trace rate is 4 Hz. This gives a trace distance of about 22 m for this product. The vertical sampling interval is 20 ns (Young et al., 2011; Cavitte et al., 2016).

4.4 Assembling the data sets

Different system characteristics and processing result in different appearance of the RES data. Our aim is to compare the RES and synthetic radar data in terms of identifying distinct reflectors that can be found in all data sets and that can confidently be matched in between the different data sets. Our basis for determining the origin of the IRHs in the RES data is by relating them to the conductivity record. For this reason, we neglect the first few microseconds, i.e., the upper few hundred meters, where most reflections are due to density changes. Like Karlsson et al. (2016), we found that this matching can best be achieved manually. But additionally we use a combination of two different ways of imaging:

1. Single traces as reflected energy versus TWT (A-scope) to compare the reflection peaks' shapes and positions. For every RES profile, the trace (of stacked data) closest to the EDC drill site is selected and plotted as a single trace. This is described in Sect. 4.5.1 and shown in Fig. 4.2. To make the different data comparable, we first shift them in time so that the surface reflections are at TWT zero. Here, we use the maximum of the surface reflection peaks for the systems with chirp wavelet (BAS, CReSIS and UTIG) but its steepest slope for the pulse systems. This is motivated by the systems differing in signal generation and digitization. The depth of a reflector is depicted not by the maximum of its reflection for the chirp systems but by the rise of its reflection for pulse systems. Note that this is also valid for internal reflections. The position of the surface-reflection pick for all traces is marked by the vertical black line in the left panel of Fig. 4.2. The exponential trend is removed from every trace. The peak amplitudes of the reflections decline in a different manner for the different data, depending on the source wavelet of the radar system and the processing. For that reason, we scale the data differently for the different depth sections to make potential reflections in the basal region more visible.
2. Radar profiles of several kilometer length around the closest trace to the drill site, plotted as TWT vs. trace number with amplitude values in grayscale (Z-scope), as shown in Fig. 4.3 and described in Sect. 4.5.2. This way of imaging is especially suitable to compare specific sequences of reflections and to check whether the reflections matched in the A-scope image are spatially coherent and representative over larger regions, e.g. for extrapolation. Again, the surface reflections are shifted to TWT zero and we plot the logarithm of the amplitudes for all RES data. For the deepest third (bottom panel) we use differently processed, i.e., 2-D-focused, CReSIS and UTIG, data for an improved visibility of the deep internal structure.

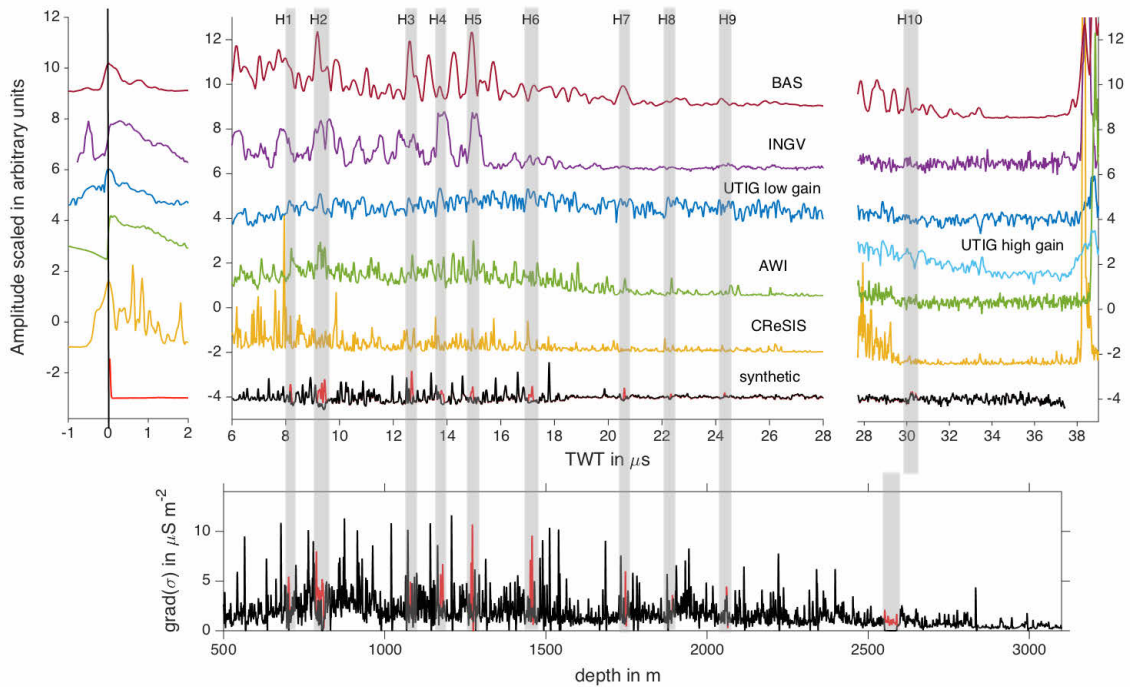


Figure 4.2. A-scopes for traces of the five radar systems (positions indicated by crosses in Fig. 4.1) and synthetic trace. The amplitudes are scaled individually and the exponential trend is removed. The surface reflection of each trace is shifted to time zero (left panel). Some distinct reflections that can be seen in some or all of the traces are gray shaded. The bottom panel shows the envelope of the gradient of the conductivity profile. The peaks that are plotted in red cause the identified reflections H1–H10 in the synthetic trace.

4.5 Results

In this section we compare the different RES data and the synthetic radar data in order to match some reflections or reflection patterns distributed over the depth range. In Sect. 4.5.3 we determine the depth origin of the identified horizons by means of sensitivity studies with the conductivity record.

4.5.1 Single traces, A-scope

Figure 4.2 shows the traces closest to EDC of all RES profiles and the synthetic trace. The positions of the measured traces are marked by crosses in Fig. 4.1.

The left panel of Fig. 4.2 shows the reflections of the air–ice interface, which marks TWT zero for each trace.

The upper middle part of Fig. 4.2 shows the traces for the majority of the ice column. In this section we find a number of distinct reflections that can be identified in some or all

of the traces. We highlight 10 of them (H1–H10), shaded in gray, for which we are confident to have them matched correctly and use them for further discussion. Those events are also used for the sensitivity studies with the conductivity record. It should be noted here that the peaks do not have the same relative amplitudes or width in the various data. Furthermore, not all IRHs can be found in all the data. The envelope of the gradient of the conductivity profile that is used for calculating the synthetic trace is plotted in the bottom panel of Fig. 4.2. The peaks of the gradient of the conductivity represent the greatest discontinuities in the dielectric properties and thus are associated with the reflection peaks in the radar data. The parts of the profile plotted in red color are the conductivity signals that have to be removed for the identified reflections to disappear from the synthetic trace. In that way, we are able to assign the reflections with their depth and age, as described in Sect. 4.5.3. What is striking, when comparing the different RES traces, is the comparatively low vertical resolution of the INGV and BAS data. Multitudes of peaks from the other data are not separately resolved by the INGV and BAS systems but rather combined to wider peaks. However, it is not always obvious which peaks join together into one peak. Nevertheless, there are still reflections that are visibly similar to those in the other traces. For example, the INGV and BAS peaks at about $15\ \mu\text{s}$ (H5) can be matched with the one in the AWI data or the INGV peak just before $14\ \mu\text{s}$ (H4) and the double peak at $17\ \mu\text{s}$ (H6) with the UTIG data. In between these reflections, though, the appearance differs considerably from the other data.

There are small time shifts for the identified reflections in the different RES data. In the CReSIS trace, for example, the peaks are usually about 50–100 ns earlier than in the other traces. The time differences for the peaks in between the other data are much smaller.

The third panel shows the bed reflections of the measured RES data and, just before the bed reflection, the section of the basal layer. In this last section, a reflection can be found at about $30\ \mu\text{s}$ that fits well in the CReSIS, UTIG high gain, INGV, BAS and synthetic data (H10).

The TWTs for the bed reflections fit well for AWI and UTIG data, with the UTIG reflections having a longer slope than the AWI, and the UTIG high gain a longer one than the low gain bed reflection. In the BAS, INGV and CReSIS trace the bed reflections occur a few hundred nanoseconds earlier. Possible reasons for the differences in the timing of the bed reflections and internal reflections are discussed in Sect. 4.6.1.2.

4.5.2 Radargrams, Z-scope

Figure 4.3 shows Z-scopes of the five RES profiles. Unlike in Fig. 4.2, here the TWT serves as the vertical axis.

In the leftmost panel the synthetic trace is shown. In the second panel this trace is adjacently plotted 200 times with the amplitude in grayscale. White noise is superimposed

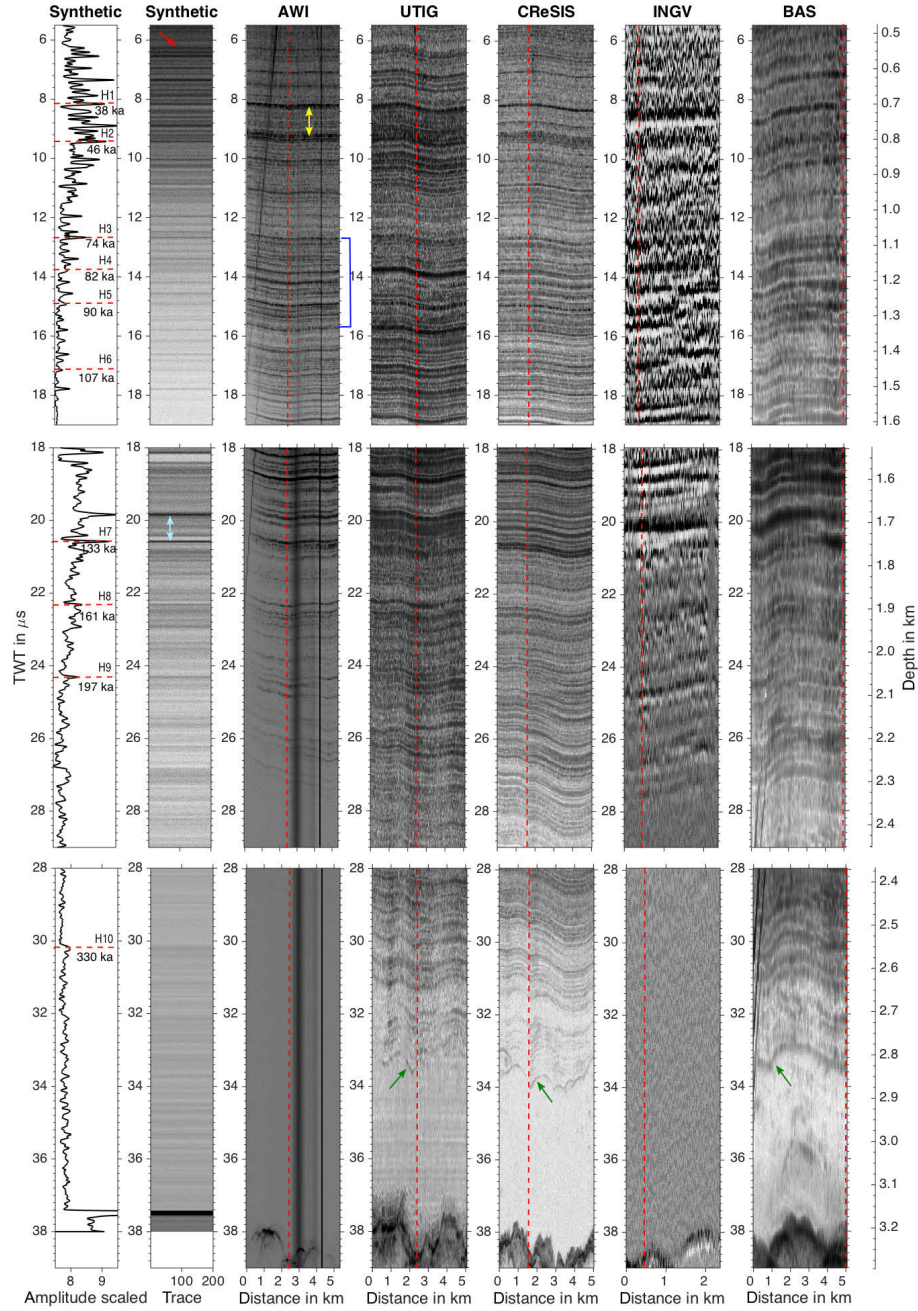


Figure 4.3. Z-scopes for synthetic and RES data sets of the five radar systems. The surface reflections are shifted to time zero as shown in Fig. 4.2 and the vertical red lines mark the positions of the traces of Fig. 4.2. The length of the RES profiles is indicated on the horizontal axes. For the depth axis we convert TWT to depth with a wave velocity of $c = 168.5 \text{ m } \mu\text{s}^{-1}$ and a firm correction of 10 m. For the bottom UTIG and CReSIS panels a 2-D-focused processing is applied. The colored arrows and lines mark distinct reflector patterns, described in detail in Sect. 4.5.

on each synthetic trace to get the appearance of a measured radargram. The other panels show the measured radar data of the five radar systems, processed as described in Sect. 4.3. We use an approximately 5 km profile length for all of the images with the exception of the INGV profile, which is only 2.7 km long.

Like with the single traces, again some reflectors can be matched nicely. Here, especially sequences of IRHs are striking – for example, the three closely spaced reflectors at about $6.5 \mu\text{s}$ TWT in the synthetic radargram (red arrow in Fig. 4.3) that can also be found in the measured data, although with a slightly different appearance. In the AWI data, the first reflector is the most pronounced one, and in the UTIG data they are rather blurred into one broad reflector. Another nice example is the strong reflector just below $8 \mu\text{s}$, followed by the wider sequence below $9 \mu\text{s}$ (H1 and H2, yellow double arrow) that catch one's eye in all of the RES data. Those can also be matched with events in the synthetic data, whereas in the latter there exist more strong reflectors in between. Hereby, the one at $9 \mu\text{s}$ is especially distinct and has a counterpart only in the CReSIS data. The section from about 13 to $16 \mu\text{s}$ TWT (blue lines), with densely spaced, relatively strong reflectors, is also similar in all of the RES data. It starts with a double reflection, corresponding to H3 in Fig. 4.2, that can also be found in the synthetic radargram. In the middle section of Fig. 4.3 the reflectors at 19.8 and $20.5 \mu\text{s}$ (H7) are the most striking ones in the synthetic data (light blue double arrow). The most alike counterpart of this sequence is to be found in the BAS data. But there is also a match in the other RES data. Notable is that the first of the two reflectors is more pronounced in the UTIG and INGV data, whereas it is the second in the CReSIS data.

Striking differences between the RES systems exist in the quality of recording reflections from the basal region, shown in the lowermost panels of Fig. 4.3. In the AWI data, where the IRHs are nicely resolved in the upper two thirds, the visibility of reflectors ceases at 28 to $29 \mu\text{s}$. The only distinct reflector after that is the bed reflection $10 \mu\text{s}$ later, leaving about 800 m without IRHs. The same is the case for the INGV data. In contrast, IRHs are clearly visible down to about 33.5 to $34.0 \mu\text{s}$ TWT in the BAS, CReSIS and UTIG data, ending with a relative strong continuous reflector with strong vertical variation (green arrows). In the BAS data there are even some signals, spatially coherent for a few kilometers, as deep as approximately $36 \mu\text{s}$ TWT. The same can be found in the CReSIS and UTIG profiles a few tens of kilometers away from EDC, which are not shown here.

At the very bottom of the figure, the bed reflections of the RES data can be seen. These measured bed-reflection depths are not to be compared with the strong reflection at the bottom of the synthetic radargram. The latter marks solely the margin of the model, which is equal to the end of the DEP record. At least 100 m are missing from the synthetic trace to the actual bed, which makes a difference of more than $1 \mu\text{s}$ in TWT.

4.5.3 Depths of the RES reflectors

To determine the depths of the IRHs, identified in Figs. 4.2 and 4.3, we conduct a sensitivity study of the synthetic trace as described in Eisen et al. (2006). By sensitivity study we mean that we remove certain peaks from the measured conductivity profile (the gradient of which is shown in the bottom panel of Fig. 4.2) and run the model with the changed input conductivity profile. As a result the respective reflection peaks disappear from the synthetic trace. As the synthetic trace closely resembles the conductivity profile, the conductivity peaks of interest can be identified with relatively small effort. An exception is the very uppermost part (~ 400 m), where the reflectivity is influenced not only by conductivity but also by density variations. The bottom trace of Fig. 4.2 shows the synthetic trace calculated with original (red) and changed (black) conductivity profile, and the bottom panel shows the gradients of the corresponding conductivity profiles. If a reflection in the RES data can confidently be matched with one of the synthetic radar-gram, the depth of the reflection can immediately be transferred from the conductivity profile. It has to be taken into account, however, that the determined depth is the horizon's depth at the ice core location and may differ from its depth at the RES trace. Even so, the horizon can be assigned with an age. Due to the conductivity-induced IRHs being isochronous, their age is the same at the position of the RES profile, even if the depth is somewhat different. If matched correctly, the uncertainty of the reflector's age depends only on the width and number of the reflection-causing conductivity peaks and the accuracy of the age scale. The advantage of the sensitivity approach over converting TWT to depth using ice core densities and a velocity function is that the depth uncertainties do not accumulate with depth but are independent of the absolute depth.

We remove sections from the conductivity record so that the gray-shaded reflections from Fig. 4.2 disappear from the synthetic trace. In that way we find, e.g., that reflection H1 is caused by the conductivity peaks in the depth range of 700.54–702.64 m or that the sequence H2 is caused by a multitude of conductivity peaks, spanning about 22 m depth. All identified reflections, the depth ranges of their inducing conductivity sections and their age ranges with standard deviation according to the AICC2012 timescale (Veres et al., 2013; Bazin et al., 2013) are listed in Table 4.2. Age uncertainties for the IRHs due to reflector width or shifts in TWT are discussed in Sect. 4.6.2.2.

4.6 Discussion

In the sections below we discuss the results of our comparison of the different data sets. Section 4.6.1 addresses the comparison of the measured RES data among each other and gives possible reasons for differences between the data. In Sect. 4.6.2 we look at the connection of the RES data with the synthetic radar trace and thus the ice core data, including an uncertainty assessment.

Table 4.2. Identified layers of Figs. 4.2 and 4.3, their approximate TWTs, depth ranges of their inducing conductivity sections and corresponding age with age uncertainties (average of published AICC2012 age uncertainties of the top and bottom depth) on the AICC2012 timescale (Veres et al., 2013; Bazin et al., 2013).

Horizon	TWT (μs)	Depth top (m)	Depth bottom (m)	Age top (ka)	Age bottom (ka)	Uncertainty (ka)
H1	8.0	700.54	702.64	38.17	38.30	0.58
H2	9.5	786.84	808.80	45.49	47.22	0.78
H3	12.5	1078.90	1081.36	73.66	73.96	2.00
H4	13.5	1172.04	1179.06	82.03	82.58	1.53
H5	15.0	1267.34	1271.30	90.04	90.40	1.60
H6	17.5	1447.58	1458.16	106.32	107.49	1.88
H7	20.5	1745.80	1746.02	132.74	132.77	2.13
H8	22.5	1891.54	1892.98	160.96	161.24	3.50
H9	24.5	2060.14	2060.40	197.17	197.23	1.96
H10	30.0	2549.88	2588.34	328.97	337.96	2.74

4.6.1 Comparability of RES data

As pointed out in Sects. 4.5.1 and 4.5.2, there are some common features notable in all of the RES data and the synthetic trace (e.g., the strong IRH at 8 μs). Especially the AWI, BAS, CReSIS and UTIG radargrams show similar patterns of reflectors, like many densely spaced reflectors (e.g., starting from 13 μs), or of lacking reflectors (22, 32 μs) at the same depths. The distinct reflectors (that are usually chosen for tracing) can be identified and traced (at least for the lengths of the investigated profile sections) in those RES data. However, there are conspicuous differences, when comparing the data with respect to resolution and penetration depth. The differences and reasons are discussed in the sections below.

4.6.1.1 Vertical and horizontal resolution

There are dissimilarities in the RES data in markedness and vertical expansion of the reflectors. Those can partly be explained by the different range resolutions of the various radar systems due to different source wavelets, receiver bandwidths, sampling rates and post-processing. The sampling intervals vertically range from 13.33 ns (AWI) to 45.45 ns (BAS) (see Sect. 4.3). This gives one sample every 1.1 and 3.8 m, respectively, in the ice of the Dome C region. The vertical resolution due to source wavelet and received-antenna system bandwidth ranges from about 3 to 17 m, as listed in Table 4.1. To some extent, the differences in the RES data can therefore be attributed to the varying range resolution of the different systems. The systems with lower range resolution are not able to capture

multiple closely spaced conductivity changes, and these closely spaced layer variations are only represented by a single reflector (of potentially complex shape). Regarding the vertical resolution of IRHs at intermediate depths, we attest the AWI, CReSIS and UTIG systems to be of best quality, which is expected per the higher range resolution identified in Table 4.1. The CReSIS system shows the most detailed structure, while the AWI system has the least penetration depth of the three systems. Due to their lower vertical resolution, the INGV and BAS radargrams, but also the AWI and UTIG data, show examples (at 10 and 20 μs) where a series of reflectors in CReSIS data are depicted as only one wider reflection. The detailed structure in the CReSIS data is advantageous for synchronizing IRHs at a specific location in high resolution, like we do in this study. However, Cavitte et al. (2016), who use several radar data sets to connect the EDC and Vostok drill sites, point out that the high vertical resolution might make it difficult to trace the IRHs over wide distances because the IRHs can thin out more easily than for systems with lower vertical resolution and therefore more robust IRH returns. As for the compatibility of the data sets, we assume that there are no major issues in combining AWI, CReSIS and UTIG data at one location where the profiles are close to each other, due to their very similar reflector patterns. However, the additional vertical resolution of the CReSIS data could add ambiguity to combined data interpretations that include tracing of IRHs (Cavitte et al., 2016). A similar problem arises when the lower resolved BAS and INGV data are included, as it might become difficult to decide which reflector to continue with when going from lower to higher resolution data. In Fig. 4.4 we show the intersection of AWI and UTIG radargrams, the location of which can be inferred from Fig. 4.1.

Two example IRHs (H1 and H4) are marked by red arrows. All strong IRHs can be traced smoothly across the transect. This supports our point that those data are well combinable.

The horizontal resolution of the bed reflection is best in the CReSIS data. Whereas in the other data the bed reflection is somewhat blurred, we get a well-defined bedrock topography from the CReSIS data. However, these quality differences could easily be induced solely by the different processing techniques or to some extent influenced by the different locations of the profiles. Thus a comparison at this stage is of little help for judging the actual systems' capabilities in depicting the bed topography. If a more quantitative comparison of this aspect is required, we propose a survey with all systems measuring a common profile with a length of 5 to 10 ice thicknesses.

4.6.1.2 Differences in IRH depth and strength

Other reasons for the reflector dissimilarities is that the measurements were not conducted at exactly the same location, with different measuring frequencies and the measurements have different path orientations as well. The depth of an isochronous IRH is dependent on surface mass balance, ice thickness and ice flow. Urbini et al. (2008) and

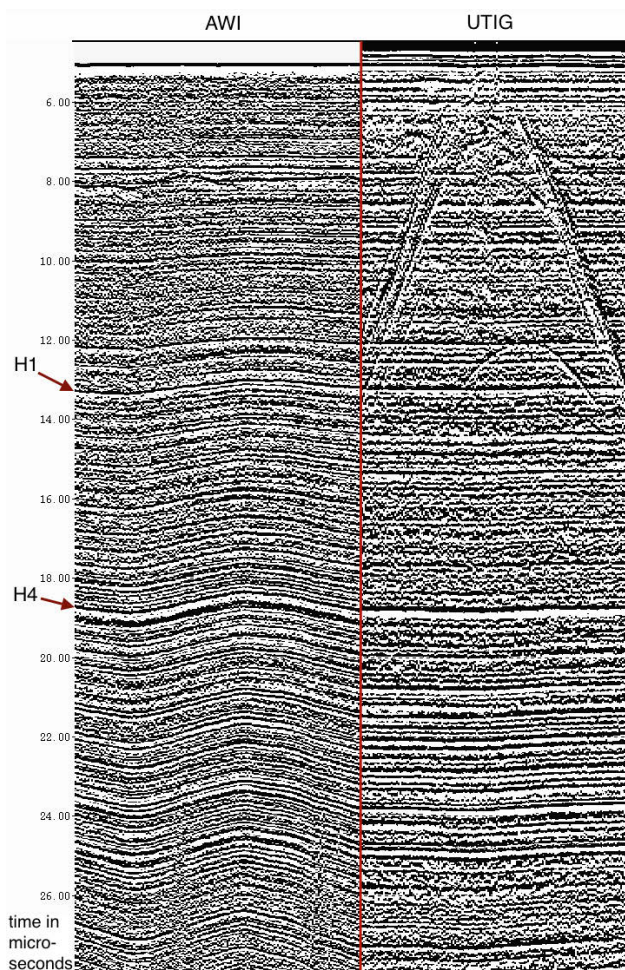


Figure 4.4. Intersection of AWI and UTIG profiles about 1 km north-east of the drill site (see Fig. 4.1) for direct visual comparison. Two examples of identified IRHs are indicated by red arrows. Note that the air-ice reflection is shifted to $5 \mu\text{s}$. All strong horizons can be traced smoothly across the intersection.

Frezzotti et al. (2005) found significant spatial variability in snow accumulation on the scale of a few kilometers around Dome C (2% within 2 km in direction SW-NE, inferred from Urbini et al., 2008, Fig. 7b). This can have the effect that some layers may be thicker in one profile than in another, leading to different appearances of the according reflections in the radargrams. It is also possible that some signals are missing completely at one location due to erosion processes (Frezzotti et al., 2005). When stationary, even small spatial accumulation variations cause spatial variations in reflector depths. This is certainly the case for greater depths, where the effect accumulates over thousands of years. We see the reflector-depth variations as TWT shifts of identified reflections in the traces in Fig. 4.2 and in the slopes of IRHs in Fig. 4.3. For instance the reflector at $11 \mu\text{s}$ in the

CRISIS data has a slope of about $0.1 \mu\text{s km}^{-1}$, corresponding to about 8.4 m km^{-1} . For the reflector at $26 \mu\text{s}$ in the same data the slope is $0.15 \mu\text{s km}^{-1}$ or 12.6 m km^{-1} . The spatial variations are thus big enough to explain the differences in TWT for the identified IRHs in the different RES data, e.g., about $0.1 \mu\text{s}$ TWT shifts for reflectors in the CRISIS profile, which is more than 1.5 km apart from the other data.

Since ice thickness is a factor for IRH depths, the slopes of IRHs are also influenced by the bed topography. We find quite steep slopes in the bed reflections in Fig. 4.3. The ice thickness varies significantly, even on the scale of the distances between the RES profiles. The bed reflection varies about $1.0 \mu\text{s}$ TWT over 1 km profile length at the steepest slopes of the bed reflections. This variation corresponds to approximately 80 m km^{-1} in bed elevation change. This is consistent with results by Rémy and Tabacco (2000), who established a $50 \text{ km} \times 50 \text{ km}$ bedrock map for the Dome C region with 1 km horizontal resolution. They found valleys, a few tens of meters deep, close to the Dome C drill site. So, again, the differences in the RES data, e.g., the $0.5 \mu\text{s}$ earlier bed reflection or earlier IRH reflections in the CRISIS trace (Fig. 4.2), can be explained by their spatial separation. Furthermore, the RES profiles have different orientations. This could be the reason that some reflectors, fully or partly induced by COF changes, are weaker or not existent in some of the data, as the power, reflected by those horizons, is dependent on the electric-polarization direction (Matsuoka et al., 2003; Eisen et al., 2007). Another factor that is worthwhile considering are the different measuring frequencies of the RES systems, the center frequencies of which range from 60 to 195 MHz . The reflection coefficient of conductivity-caused horizons is frequency dependent (Fujita and Mae, 1994). This leads to different reflection amplitudes or reflector strength of one certain horizon in radar data measured with different frequencies, in case the corrected relative returned power (in dB) is plotted. According to MacGregor et al. (2015b) also the conductivity itself is slightly frequency dependent. This causes a signal to be more or less attenuated, depending on its frequency. This does not influence the TWTs or inferred depths of IRHs and thus is not so relevant for studies of the age structure of the ice sheets. However, the frequency dependence of conductivity certainly is a factor that should be closely examined when using RES data to deduce attenuation rates and ice temperature.

4.6.1.3 Penetration depth

The IRHs cease to be visible at different depths in the bottom section of Fig. 4.3. This happens in a different manner for the different RES data. In the AWI and INGV data it is a rather slow process, with IRHs gradually becoming weaker. The weaker IRH response is due to the attenuation of the RES signal as it propagates through the ice. As such, weak internal reflectors are difficult to detect, whereas the strong return from the ice–bedrock interface can still be detected. In contrast, the UTIG, CRISIS and BAS data clearly show

reflectors down to approximately 33 μs , with comparably strong “last” reflectors (green arrows) and below that depth no continuous IRHs are visible. The lack of continuous IRHs below is not an issue of the systems’ power, but rather it means that the former horizons are in some way deformed, amalgamated or disrupted into small-scale structures, not resolvable by the radar systems. This basal region, indicated by a sudden drop of returned power in the radar data, is described as echo-free zone (EFZ) by Fujita et al. (1999) and Drews et al. (2009). The lack of IRHs in this range not being an issue of the systems’ power is also supported by the fact that there are regions with to some extent spatially coherent signals almost down to the bedrock, like in the BAS data and also in the UTIG and CReSIS profiles, outside the 5 km range shown in Fig. 4.3. It is difficult to give a comparing judgement on the quality of the three RES systems in this deepest part. The profiles were not measured at the same location and the internal structure in the ice close to the bed differs strongly. However, as we still see some small-scale structures and coherent signals, we are confident that all three systems are able to image structures in the basal layer reliably. As the basal layer comprises the old ice, this is a crucial factor for oldest ice reconnaissance surveys. The lower range resolution of the BAS system, comparative to the other two systems, applies also for the basal layer.

4.6.2 Synchronization of RES and ice core data

We find that distinct patterns of IRHs in the RES data can also be found in the synthetic trace. The pronounced reflectors that are identified in all RES data can also be matched with the synthetic data. In this way their depth origin at the drill site and thus their age can be determined, as described in Sect. 4.5.3. However, like for the measured RES data, there are also pronounced differences in appearance between the RES and synthetic data. Possible reasons are discussed in Sect. 4.6.2.1. The uncertainties on depth and age are discussed in Sect. 4.6.2.2.

4.6.2.1 Differences between modeled and measured data

The dissimilarities in the appearance of reflectors described for the comparison of the different RES data are even stronger when comparing any of the measured RES data with the synthetic trace. This is consistent with the explanation by different measuring sites and spatial variability in accumulation and ice thickness. The synthetic trace is calculated from the ice core data. The EDC99 core and the RES profiles are a few hundred to 2000 m apart. Additionally, the core, with its 0.1 m diameter, samples a much smaller area than a radar system that averages over a footprint on the 100 m scale. There were discussions about the spatial significance of ice core signals (e.g., Fisher et al., 1985; Richardson and Holmlund, 1999; Veen and Bolzan, 1999). Palais et al. (1982) and Münch et al. (2016) examine the representativity of cores, using snow accumulation variability and stable-water isotope variations, respectively. Frezzotti et al. (2005), too, get slightly different

accumulation rates from ice core and radar measurements and explain them with the different sample area. However, they find that for the Dome C region the differences of core and radar measurements of 3 % and the spatial variability of accumulation are relatively small compared to other East Antarctic regions, and the smallest of their Dome C–Terra Nova Bay traverse.

Wolff et al. (2005) compare the conductivity record of the EDC99 core with the one of the first drilling attempt (EDC96) that is 10 m away. They find that only in 45 % of the cases the largest conductivity peak in a 10 m section is also the largest peak in a 10 m section of the parallel core. This is typical of low accumulation sites, because significant parts of a single year’s signal can be lost at a location by post-depositional processes like snow drift. Gautier et al. (2016) evaluate the variability of the volcanic signal at the EDC site, using five 100 m firn cores, drilled 1 m apart from each other. They found that the probability of missing volcanic events is 30 % when using only a single core. The Tambora event (1815 CE), for instance, is not detected by their algorithm in two out of five cores. Wolff et al. (2005) suggest using methods that sample a larger volume of ice to smooth out the spatial inhomogeneity. RES being such a method explains that the RES data are more similar among each other than RES versus synthetic data. This implies also that a very strong RES reflector does not necessarily have to be a large peak in the conductivity profile or synthetic trace.

For some quantitative comparison of amplitudes, e.g., for deriving the attenuation rate, again, the different source wavelets have to be taken into account. The synthetic trace is calculated with a monochromatic burst wavelet. We neither scaled reflection amplitudes to the differing center frequencies of the CReSIS and UTIG systems nor accounted for the finite bandwidths of the chirp systems. Furthermore, conductivity itself is frequency dependent (MacGregor et al., 2015b). This implies that also the different measuring frequency of the DEP compared to the source wavelet (100 kHz vs. 150 MHz) effects the reflection amplitudes of the synthetic trace. However, the uncalibrated conductivity profile of the Dome C core and the simple model itself do not allow to quantitatively analyze the reflection amplitudes, but only the signature of reflection patterns in our study. In addition to these factors, all related to the intrinsic frequency dependence of the dielectric properties, the frequency-dependent thin-film interference also influences the measured and modeled amplitudes. The signals from interfaces between layers with constant dielectric properties can be strengthened or weakened by constructive or destructive interference, depending on the thickness of the layers and the source frequency. This may complicate any data combination that is dependent upon amplitudes yet further.

4.6.2.2 Uncertainty assessment

Uncertainties incorporated in the synthetic data are the uncertainties from the ice core measurements, inaccuracies in determining the permittivity and the neglect of temperature and anisotropy. The uncertainties on the density decrease with depth due to higher absolute densities, and Hörhold et al. (2011) give a value of 0.66 % at 100 m depth. The errors in the permittivity, induced by neglecting the complex character in the air–ice mixture, are negligible, as we exclude the firn section and look only at depths greater than 600 m, where the air partition is minor. Uncertainties on wave velocity due to the dependence of the permittivity on temperature and anisotropy both stay below 1 % (Gough, 1972; Matsuoka et al., 1997; Fujita et al., 2000).

The errors in the synthetic trace have an influence only on the TWT of the synthetic reflectors, and thus eventually on matching those with the RES reflectors, but not on the actual depth and age assignment. Sensitivity studies with the conductivity profile define the depth range in which a synthetic reflection peak has its origin. Thus the depth uncertainties of the IRHs are given by the depth uncertainties of the DEP measurements and the vertical resolution of IRHs in the synthetic trace. The latter is adjustable, as it is defined by the bandwidth of the source wavelet and the smoothing filter, as shown by, e.g., Cavitte et al. (2016). The depth uncertainties of the DEP measurement are reported as about 2 mm by Wolff et al. (1999). Added to that comes the depth uncertainty of the ice core itself, which is difficult to quantify. Due to breaks in an ice core, an inclined borehole and core relaxation after drilling the logged ice core length is always different from the true depth. Parrenin et al. (2012, Sect. 2.2.1) estimate the offset to reach up to several meters for a deep drilling. The direct transfer of reflector depths by the sensitivity studies is not completely true for the RES reflectors. Because of different bandwidths used in the RES data, there is an uncertainty associated in matching the peaks between the synthetic and RES data sets. All of the BAS and INGV reflections, for example, are wider than the ones in the synthetic trace and thus it is not clear which conductivity peaks are incorporated in one RES reflector. The age uncertainties due to reflector width increase with depth and can be inferred from Fig. 4.5, which shows the gradient of age with depth (blue curve) and with TWT (black), respectively.

Added to that comes the age uncertainties from the AICC2012 age scale itself, given in Table 4.2 (Veres et al., 2013; Bazin et al., 2013). The curves of Fig. 4.5 also give the magnitude of error in age that is avoided by our method compared to using only a RES profile, in some distance to the core, and the age scale of the core. For example, the RES profile is 1 km away from the core and the IRH of interest has a slope of 10 m km^{-1} in the direction drill site–RES profile. When using only the RES profile, we would assign the reflector with an age off by 10 m on the ice core timescale. For a reflector at about $10 \mu\text{s}$ TWT that would correspond to an age shift of about 1 ka, for a reflector at $32 \mu\text{s}$ of about 8 ka. This

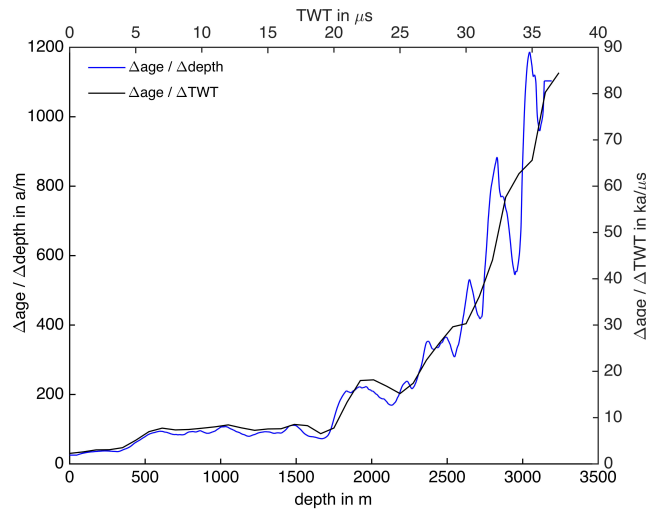


Figure 4.5. Gradient of the age from the AICC2012 age scale with depth (blue, left and bottom axes) and TWT (black, right and top axes) to infer age uncertainties due to reflector width and slope.

shows the advantage of our approach of first matching the RES IRHs with the synthetic radargram and only then determining the depth and age of the reflectors at the ice-core location, as it eliminates one possible source of error. The extent of error reduction, however, does depend on IRH slopes and distances of the RES profiles to the ice-core site.

4.7 Conclusions

In our study we compared the data sets of five different RES systems, addressing the questions of their compatibility for combined usage and suitability for informing potential “oldest ice” site characterization. All RES profiles were recorded within a 2 km radius around the EPICA Dome C drill site, where the current oldest ice sample was retrieved. We found that the data are broadly comparable at that location and that the most-pronounced reflectors can be found in the RES data. The main differences between the RES systems are constituted by their resolution of englacial structure and bedrock and their quality in imaging the basal layer. The CReSIS data have the best horizontal resolution in the depth of the bed and are thus providing a well-defined subglacial bedrock topography. At this stage it is inconclusive whether this can be attributed to the CReSIS system or rather to the different processing technique and profile location. If interested in vertically well resolved IRHs at intermediate depths, the AWI, CReSIS and UTIG systems are the most suitable due to their comparably high vertical resolution. However, we did not investigate the continuity of the IRHs beyond the 5 km profile lengths. Based on their close similarity in reflection patterns at the investigated location we assume that the AWI, CReSIS and UTIG data are smoothly combinable for common interpretation, which

is supported by the direct comparison of AWI and UTIG radargrams at their profiles' crossover point. However, the even higher vertical resolution of the CReSIS data might cause some difficulties for the transfer of certain IRHs, as they might transition into multiple peaks. However, this has to be checked directly at the crossover points for the IRHs of interest. The CReSIS, UTIG and BAS systems have the largest penetration depth and are able to image some structures in the basal region. Nevertheless, due to the comparably low vertical resolution of the BAS data, we attest the CReSIS and UTIG systems the best overall suitability in our comparison for oldest ice reconnaissance surveys. The AWI and INGV data in the current version are not as convenient for this purpose, as they fail to depict the internal structure in the deepest approximately third of the ice thickness at EDC. Nevertheless, the profiles could be used to close data gaps with respect to IRHs at intermediate depths and ice thickness.

In addition to the comparison of the RES data, we synchronized the measured RES data with a synthetic radar trace for depth conversion. Input for the forward model for the synthetic trace were the EDC ice core conductivity and density. We found that the RES data are more similar among each other than compared to the synthetic trace. This can be explained by the spatial variability of the strengths of single conductivity signals as sampled by ice cores and the smoothing effect of RES measurements due to their larger footprint and lower vertical resolution. Another reason for the differences is the partly differing frequencies and source types of synthetic and RES data, which have an influence on the reflection amplitudes. This factor needs to be examined more closely for quantitative amplitude analysis, which is necessary for inferring the attenuation rate and ice temperature from IRHs. Such analysis, however, is not feasible with the data available for this study, as the DEP measurements do not allow for correctly reproducing reflection amplitudes. Despite the differences we were able to match 10 pronounced reflectors in the RES and synthetic data. We identified the causative conductivity peaks of the matched IRHs and in this way determined their depth and age. Since the identified IRHs are caused by conductivity and thus isochronous, they can be used to extend the age structure, provided by the Dome C ice core, to regions of interest for an oldest ice drill site.

The combining of different RES data and the dating of horizons is requisite for a large-scale mapping of the age structure of the East Antarctic ice sheet, where no reasonable coverage or resolution is obtained with only one data set. The age architecture in turn facilitates the inference of spatial and temporal variations of mass balance and provides boundary conditions or parameters for large-scale ice-flow models.

4.8 Acknowledgements

Operational support was provided by the US Antarctic Program, the Institut Polaire Français Paul-Emile Victor (IPEV), the Italian Antarctic Program (PNRA and ENEA) and

the Japanese National Institute of Polar Research (NIPR). We acknowledge that several CReSIS faculty, staff and students contributed to the development of radars and antenna arrays used to collect data reported here. The UTIG line was funded as part of NSF's International Polar Year activities (grant ANT-0733025) to the University of Texas at Austin and the UK's NERC grant NE/D003733/1 to University of Edinburgh. Additional support was provided by the French ANR Dome C project (ANR-07-BLAN-0125). We would like to thank T. Jordan and one anonymous reviewer for their comments which greatly improved the original manuscript and R. Bingham for handling our submission. This is UTIG contribution 3088.

The article processing charges for this open-access publication were covered by a Research Centre of the Helmholtz Association.

Edited by: R. Bingham

Reviewed by: T. Jordan and one anonymous referee

5 Deducing large-scale age distribution and paleo-accumulation rates from radiostratigraphy in East Antarctica

This chapter is in review for the Journal of Glaciology.

Abstract

We derive the age-depth stratigraphy from radio-echo sounding data, in combination with ice-core age scales, for large parts of the East Antarctic Ice Sheet. The age scales of different East Antarctic deep drill sites are connected with several radio-echo sounding horizons, dating back to the penultimate glacial. In Dronning Maud Land, including Dome Fuji, we use isochrones with ages of 38 ka and 74 ka. In the central region of East Antarctica around Dome Concordia, Vostok, and Dome Argus, the isochrone ages are 38 ka, 48 ka, 90 ka, and 161 ka. Horizons were traced along a combined profile length of more than 40,000 km. Based on the dated stratigraphy and using a flow-divergence correction calculated from a continental-scale ice-sheet model, we derive mean accumulation rates for two time intervals. We analyze the spatial distribution of horizon depths and accumulation rates and evaluate the usability of the large-scale model and the comparably simple approach for deriving paleo-accumulation rates.

5.1 Introduction

The stratigraphy of the large ice sheets is relevant for understanding the dynamic history of the ice sheet as well as the climate archive contained within those layers. An established accurate age-depth stratigraphy can inform and constrain or be used to test ice-flow models (Waddington et al., 2007; Hindmarsh et al., 2009; Leysinger Vieli et al., 2011; Parrenin et al., 2017). In ice coring, the stratigraphic information is crucial for drill-site selection in order to provide information about age resolution, maximum expected

age and to ensure an undisturbed layering at the coring location (Fischer et al., 2013). Furthermore, it is valuable for interpreting the core records after the drilling, as it can inform the age-depth scale development (e.g., Fahnestock et al., 2001) or possibly hint at a disordered ice-core stratigraphy, like in the NEEM ice core (NEEM community members, 2013).

Radio-echo sounding (RES) provides a powerful tool to gain insight in the ice-sheet stratigraphy. It is a widely used method to investigate bed topography and condition, internal structure and accumulation rates (e.g., Fujita et al., 2012; Urbini et al., 2015; Robin et al., 1970; Drews et al., 2009; Steinhage et al., 2013; Cavitte et al., 2016; Hawley et al., 2014; Karlsson et al., 2016). In the last decades substantial work has been done and great progress made in RES-system development (e.g., Gogineni et al., 1998; Rodriguez-Morales et al., 2014), data acquisition and data interpretation (e.g., Karlsson et al., 2012; Bell et al., 2014; Sime et al., 2014; MacGregor et al., 2015b).

Based on the by now reasonable RES-data coverage of Greenland, the 3D-stratigraphy and subsequently other glaciologically important parameters can be derived on an ice-sheet wide scale (MacGregor et al., 2015a, b, 2016).

Due to the remoteness and spatial extent of Antarctica and the high cost of field logistics for surveys, the data coverage of the East Antarctic Ice Sheet (EAIS) is sparser and interpretation more difficult. The EAIS is the largest ice sheet on Earth and consequently could have the greatest influence on sea level projections. Furthermore, it is the only place, where chances are good to find a suitable drill site for an “Oldest Ice” ice core, dating back to 1.5 Ma BP (Fischer et al., 2013; Parrenin et al., 2017; Young et al., 2017). The retrieval of such an ice core is outlined as a future goal in ice-core research by the Steering Committee of the International Partnerships in Ice Core Sciences (IPICS), and the currently running European project Beyond EPICA - Oldest Ice is designed to fulfill this goal within a few years. This study aims at establishing a broad mapping of the stratigraphic architecture of the EAIS, thus providing spatially distributed estimates of age, and at inferring first-order approximations of accumulation.

We use airborne RES data that have been collected by the Alfred Wegener Institute (AWI) in numerous campaigns during the last 20 years, and RES data collected as a part of the Antarctica’s Gamburtsev Province (AGAP) Project by the Lamont-Doherty Earth Observatory (LDEO), Columbia University, in collaboration with the Center for Remote Sensing of Ice Sheets (CRISIS), University of Kansas. We trace the most distinct and continuous internal reflection horizons (IRHs) along these RES profiles across the ice sheet. The IRHs are assigned with their ages at the drill sites of deep ice cores. In a next step, we derive accumulation rates from the established age stratigraphy. To account for the thinning of accumulated ice by ice kinematics, we make use of ice-flow modeling with the Parallel Ice Sheet Model (PISM) (Winkelmann et al., 2011). Our aim is not to develop the

most sophisticated model or method to get the exact accumulation rates in high spatial and temporal resolution. We rather try to find a simple and fast method, applicable to large areas and using already available tools, to evaluate whether we can capture the large-scale paleo-accumulation patterns. Our study provides a method that can easily be extended to increasing data sets and combinations of data from different RES systems.

5.2 Study region

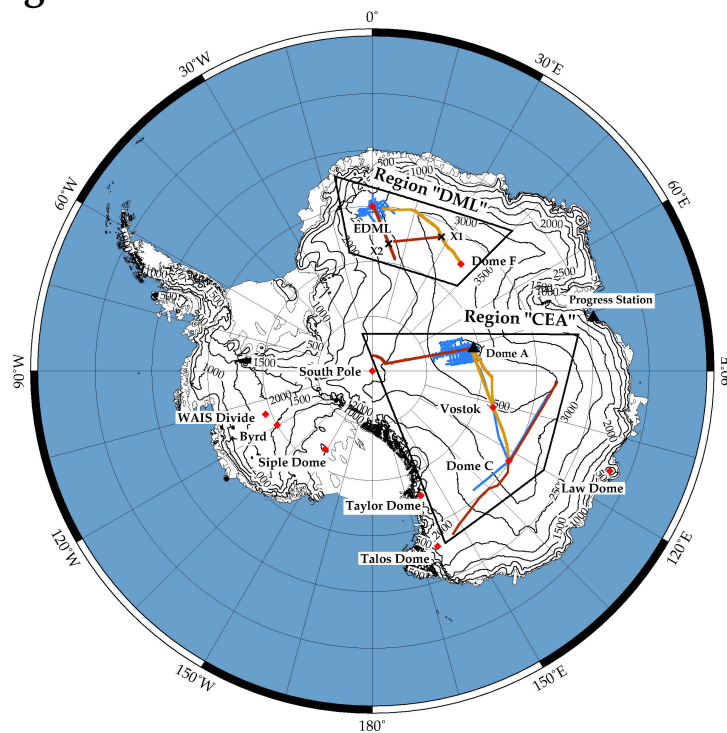


Figure 5.1. Blue, yellow and red lines indicate the RES profiles along which we continuously traced at least one horizon from a deep drill site, separated in the regions Dronning Maud Land (DML) and Central East Antarctica (CEA). Red diamonds mark the deep drill sites. Figures 5.2a and 5.2b, and Fig. 5.2c, 5.2d and 5.2e show results for the yellow and red profiles, respectively.

Our investigations are focused on the interior of East Antarctica, where we consider two separate regions. Within each region, all RES profiles are connected to a deep drill site via crossing profiles. Hereafter, we refer to the region including the EPICA (European Project for Ice Coring in Antarctica) Dome Concordia (EDC) and Vostok drill sites as Central East Antarctica (“CEA”). The Dronning-Maud Land (DML) region, including the Dome Fuji (DF) and EPICA DML (EDML) drill sites is named “DML”. Figure 5.1 gives an overview of the RES profiles in the two regions and the deep drill sites in East Antarctica.

The profiles of the CEA region are mostly located on the plateau near the ice divides. The central locations of the RES surveys are Dome Concordia (DC) for the AWI data and Dome Argus (DA) for the AGAP-South grid. This grid of RES profiles densely covers

the Gamburtsev Mountain Province, a mountainous region where presumably the EAIS nucleated (DeConto and Pollard, 2003; Bo et al., 2009). The grid has a line spacing of 5 km and 33 km in east–west and north–south direction, respectively (Bell et al., 2011). The DML region is located in the Atlantic-Indic sector of East Antarctica, roughly 20° W to 40° E. It includes the coastal region and the plateau of DF. There is a high coverage of AWI RES data in this region, especially around the EDML drill site.

5.3 Data and Methods

5.3.1 RES data

We use RES data of two different systems with accordingly different characteristics. All our RES profiles (Fig. 5.1), except for the AGAP-South grid, were collected by AWI between 1998 and 2008. The radar system is a burst system with a carrier frequency of 150 MHz, mostly operated in toggle mode, where it alternates between 60 ns and 600 ns bursts lengths (Nixdorf et al., 1999). We use the 600 ns data for ice-thickness picks and the 60 ns data for IRH interpretation. The data were recorded with 13.33 ns vertical and 20 Hz horizontal sampling. We stack the data 10-fold horizontally, which results in an average trace distance of 75 m in toggle mode. To increase the visibility of IRHs, we differentiate the data, apply a low-pass filter of 150 MHz and an automatic gain-control filter in vertical direction. The range resolution of the processed data in ice is 5 m. The AGAP-South data were collected in austral season 2008/2009. The RES system is based on the Multi-Channel Coherent Radar Depth Sounder (MCoRDS), developed by CReSIS, with a center frequency of 150 MHz and a bandwidth of 20 MHz (Lohofener, 2006). Synthetic-aperture migration was applied. The range resolution of the processed data is 7 m in ice (Wolovick et al., 2013; Creyts et al., 2014). The data are available on the AGAP web page (Antarctica’s Gamburtsev Province Project - South, 2008/09). We additionally stack the data to an average trace distance of 13 m and differentiate them. The last step before tracing the IRHs is to shift the onset of each recorded shot to time zero. We find this to be the easiest way to ensure consistency in the surface, bed and IRHs at profile crossovers, as the radar-system delay is unknown for some profiles and thus there are biases in the measured travel times of the reflections. With this flattened ice surface we do not get the absolute elevations of traced IRHs, but only the depths below the surface. However, this has the advantage that the resulting stratigraphy can be adjusted to elevation models of higher precision afterwards, e.g. derived from satellite altimetry.

5.3.2 RES internal reflection horizons

After assuring a good visibility of the IRHs in our data, we semi-automatically trace them in the two-way travel-time (TWT) domain, using the commercial seismic-processing software Landmark. We choose the most distinct IRHs that can be traced continuously along

all profiles. The IRHs are transferred from one profile to another at crossover points by comparing the TWTs in both profiles and visually comparing the reflection patterns at the respective locations. We omit IRHs that cannot be transferred with sufficient certainty or that are truncated or lost in a profile without a circumvention.

The IRHs are assigned with ages at their intersections with deep drill sites. At these locations, IRHs are converted from TWT domain to depth, using the measured ice-core densities in firn. The age of the IRHs is then taken from the ice core age-depth scale. In the DML region we use the same IRHs that were used by Huybrechts et al. (2009) and Steinhage et al. (2013) to connect the DF and EDML drill sites. Compared with them, we use the more recent age scales DFO-2006 (Kawamura et al., 2007) and AICC2012 (Bazin et al., 2013; Veres et al., 2013) for the dating and take the mean of the respective IRH ages from the DF and EDML age scales. The TWT-to-depth conversion and age assignment in the CEA region has been carried out by Winter et al. (2017), who use the ice-core density and conductivity measurements from the EDC ice core to calculate synthetic radar traces. The synthetic traces are synchronized with measured RES data from the vicinity of the drill site to identify distinct IRHs. The depths of those are then determined by sensitivity studies of the synthetic trace, where peaks are removed from the conductivity profile. In this way the depth uncertainties of the IRHs depend only on the depth uncertainty of the conductivity measurements and the width of the reflection-causing conductivity section. Due to this accurate IRH dating at the EDC ice core, we do not use the ages from the Vostok ice core on the IRHs. At all places other than EDC, the depth uncertainty of the IRHs is the sum of the radar-system and picking uncertainty (we assume an accuracy of two samples $\hat{=}$ ± 2.2 m) and the uncertainty on the TWT-to-depth conversion. The latter is de facto the uncertainty of the density-depth function in the firn or the firn correction and the uncertainty of the electro-magnetic wave speed in ice. Fujita et al. (2000) give a range from $168.0 \text{ m}^{-1}\text{s}$ to $169.5 \text{ m}^{-1}\text{s}$ for the wave speed in ice, therefore, we use an uncertainty of $\pm 0.44\%$. This results in an increasing depth uncertainty with increasing IRH depth. The age uncertainty of an IRH is the RMS (root-mean square) of the depth-uncertainty related age uncertainty and the age-scale uncertainty.

Keeping only the most extensively traceable IRHs leaves us with two dated IRHs in each region. In DML these are the 38.1 ± 0.7 ka, and 74.2 ± 1.7 ka IRHs. The latter is most probably caused by the Toba eruption (Eisen et al., 2006; Svensson et al., 2013). In CEA we use the IRHs with ages of 38.2 ± 0.6 ka and 161.1 ± 3.5 ka. To increase the age resolution in this region, we use two more IRHs inbetween with ages of 48.3 ± 1.2 ka (this one is not listed in Winter et al. (2017) and is slightly deeper than their horizon H2) and 90.2 ± 1.6 ka. They could not be traced in all profiles in the CEA region, but along the central profile DC-DA (yellow in Fig. 5.1) and to some extent in the AGAP grid around DA. The Toba

horizon is not continuously traceable all the way from DC to Vostok (see Discussion). For that reason we do not use this IRH for the CEA region.

5.3.3 Deriving accumulation rates

We next derive mean accumulation rates for the dated layers. The term layer is used as the ice layer that is bound by two IRHs or one IRH and the ice surface, respectively. We label the layers according to the time periods the bounding horizons span as Hc–LG (0–38 ka), LG (38–74 ka), LG–PG (38–161 ka) (abbreviations Hc: Holocene, LG: Last Glacial and PG: Penultimate Glacial). To account for the effect of non-parallel ice flow, we make use of the velocity field calculated with PISM (v0.6.2) (The PISM authors, 2016; Winkelmann et al., 2011).

The model solves the non-sliding shallow ice approximation (SIA) and the shallow shelf approximation (SSA). The grounded ice flow speed is computed with a hybrid scheme based on a weighted superposition of both shallow solutions (SIA + SSA), where the SSA solution acts as a sliding law. (See Bueler and Brown (2009) for details.) The enthalpy gradient method (Aschwanden et al., 2012) is used to solve for temperature and moisture content.

The simulation is conducted in a series of subsequent grid refinements (all based on the initial 1 km BEDMAP2 geometry (Fretwell et al., 2013)) using 40, 20 and 10 km horizontal resolution and 41, 81 and 101 vertical layers (refined towards the bed), respectively. The geometry, including ice thickness, calving front and grounding line, is free to evolve in the spin-up. For all spin-up stages the boundary conditions are held constant over time, thus forming a present-day climate equilibrium model realization. We use surface skin temperature and surface mass balance from RACMO 2.3/ANT (Van Wessem et al., 2014) and the geothermal heat flux data set from Shapiro and Ritzwoller (2004). Basal melt rates underneath the ice shelves are calculated based on the method described by Beckmann and Goosse (2003). Parameters within the PISM model are the same as used for the SeaRISE Antarctica project (see ‘Potsdam’ model in Nowicki et al. (2013)), where the model was also forced with a steady present-day climate.

The model run gives us the ice-sheet velocity (v_x, v_y, v_z) in 10 km horizontal resolution, which we bi-linearly interpolate to 1 km in the horizontal.

We use the ice thickness evolution equation (Greve and Blatter, 2009, sec. 5.1.3):

$$\frac{\partial H}{\partial t} = - \left(\frac{\partial}{\partial x} \int_{z_b}^{z_s} v_x dz + \frac{\partial}{\partial y} \int_{z_b}^{z_s} v_y dz \right) + \dot{b}_s - \dot{b}_b, \quad (5.1)$$

with the total ice thickness H , the time t , the surface mass balance \dot{b}_s , the basal mass balance \dot{b}_b (positive for melting), the elevation of the ice surface z_s and the elevation of the bed z_b . The total horizontal volume flux divergence is given in large parentheses in Eq. (5.1). If the total ice thickness H is replaced by the layer thickness $H_h = z_s - z_h$, where z_h is the elevation of the horizon of interest, Eq. (5.1) can be reorganized for the mean surface accumulation rate for this layer:

$$\dot{b}_{s,[z_h,z_s]} = \frac{H_h}{a_h} + \left(\frac{\partial}{\partial x} \int_{z_h}^{z_s} v_x dz + \frac{\partial}{\partial y} \int_{z_h}^{z_s} v_y dz \right) + \dot{b}_h. \quad (5.2)$$

The first term on the right side is the ice thickness above the horizon of interest, divided by its age a_h . The part in brackets, the horizontal volume flux divergence, describes the removal or adding of mass above the horizon by horizontal ice flow. The melt rate at the base of the layer \dot{b}_h is zero, because this is a material surface where no ice flows through the surface. The mean accumulation rate for a time interval (depth interval) that does not start at present day (surface), can be obtained by

$$\dot{b}_{s,[z_{h2},z_{h1}]} = \frac{a_{h2} \dot{b}_{s,[z_{h2},z_s]} - a_{h1} \dot{b}_{s,[z_{h1},z_s]}}{a_{h2} - a_{h1}}. \quad (5.3)$$

To assess horizontal volume flux divergence, we find the nearest neighbor of each RES-profile point on the resampled PISM grid. Following Eq. (5.2), we numerically integrate the horizontal velocity components $v_{x,i}$ and $v_{y,i}$ from the respective horizon elevation $z_{h,i}$ to the surface at the four neighboring points, i , of the nearest neighbor. We then calculate the gradients of the velocity-component integrals with respect to the respective horizontal direction.

The accumulation rate \dot{b}_s in Eq. (5.2) is given in units of meter ice equivalent per year. We multiply this value with the mean density for the interval $[z_h, z_s]$ derived from the EDC and EDML ice cores for the CEA and DML regions, respectively. This accounts for the thinning by densification and results in a specific accumulation rate in units: $\text{kg m}^{-2} \text{a}^{-1}$. Finally we smooth the result with an moving average of 35 km, which is about 10 times the ice thickness.

It should be noted here that our approach does not take into account the horizontal movement of the particles, i.e. that the snow was not deposited at the location we are looking at (i.e. the trajectory) and might have undergone changing accumulation rates and changing flow divergence along the way. Potential shortcomings of this approach are discussed below.

5.4 Results

5.4.1 Age stratigraphy

Two dated IRHs are continuously traced in all profiles (Fig. 5.1), delivering their depth distribution for a good part of the EAIS. In the DC–DA profile we use four IRHs and thus have a higher age resolution. The top panel of Fig. 5.2 a shows the traced IRHs and the ice-surface and bedrock elevation along this profile.

The shallower IRHs are comparably smooth. They follow the surface topography, except for some locations with very steep bed topography, e.g., at kilometer 550, shortly before the Vostok drill site. The deeper the IRHs, the more they follow the bed topography. The relatively smooth depression in the ice–bedrock interface around kilometer 600 marks Lake Vostok. The known feature of the deep IRHs dipping downwards above the lake (Studinger et al., 2003) is clearly noticeable. The depths of the four IRHs with uncertainties at EDC, Vostok and DA and their ages from the EDC and Vostok AICC2012 ice-core age scales (Bazin et al., 2013; Veres et al., 2013) with uncertainties are listed in Table 5.1. The top panel of Fig. 5.2 b shows the surface, bed and IRHs, traced along the EDML–DF

Table 5.1. The depths d below ice surface of the four IRHs and the bed at DC, Vostok and DA with depth uncertainties Δd and their ages a from the EDC and Vostok AICC2012 ice-core age scales (Bazin et al., 2013; Veres et al., 2013). The age uncertainties are separated in contributions from depth uncertainties $\Delta a(d)$ and age-scale uncertainties $\Delta a(a)$.

IRH	DC					Vostok					DA	
	d m	Δd m	a ka	$\Delta a(d)$ ka	$\Delta a(a)$ ka	d m	Δd m	a ka	$\Delta a(d)$ ka	$\Delta a(a)$ ka	d m	Δd m
H1	702	2	38.2	0.2	0.6	571	5	38.1	0.4	1.2	625	5
H2	820	6	48.3	0.6	1.0	699	6	48.9	0.4	1.4	757	6
H5	1269	4	90.2	0.4	1.6	1283	8	90.4	0.6	1.6	1101	7
H8	1892	2	161.1	0.3	3.5	2146	12	161.8	1.4	2.5	1424	9
bed	3240	17	–	–	–	3742	19	–	–	–	2075	12

profile. This profile is composed of two RES flights of different surveys. The part from EDML to X1 was flown in season 1999, the part X1 to DF in 2003. This time difference causes a slight change in IRH depth. However with accumulation rates of about 30 to $40 \text{ kg m}^{-2} \text{ a}^{-1}$ in this region the maximum gain in this period is less than 0.2 m of ice. As this is less than 10% of our uncertainty for IRH picking, no measures were taken to account for the difference. The middle panels of Fig. 5.2 a and 5.2 b show the variation of relative layer thicknesses along the respective profiles. The normalized thickness of each layer, bound by two IRHs, or surface and shallowest IRH, is divided by the normalized thickness of this layer at the EDC and DF drill sites, respectively. Especially in the DF–EDML profile the layer thicknesses systematically change from DF towards the coast.

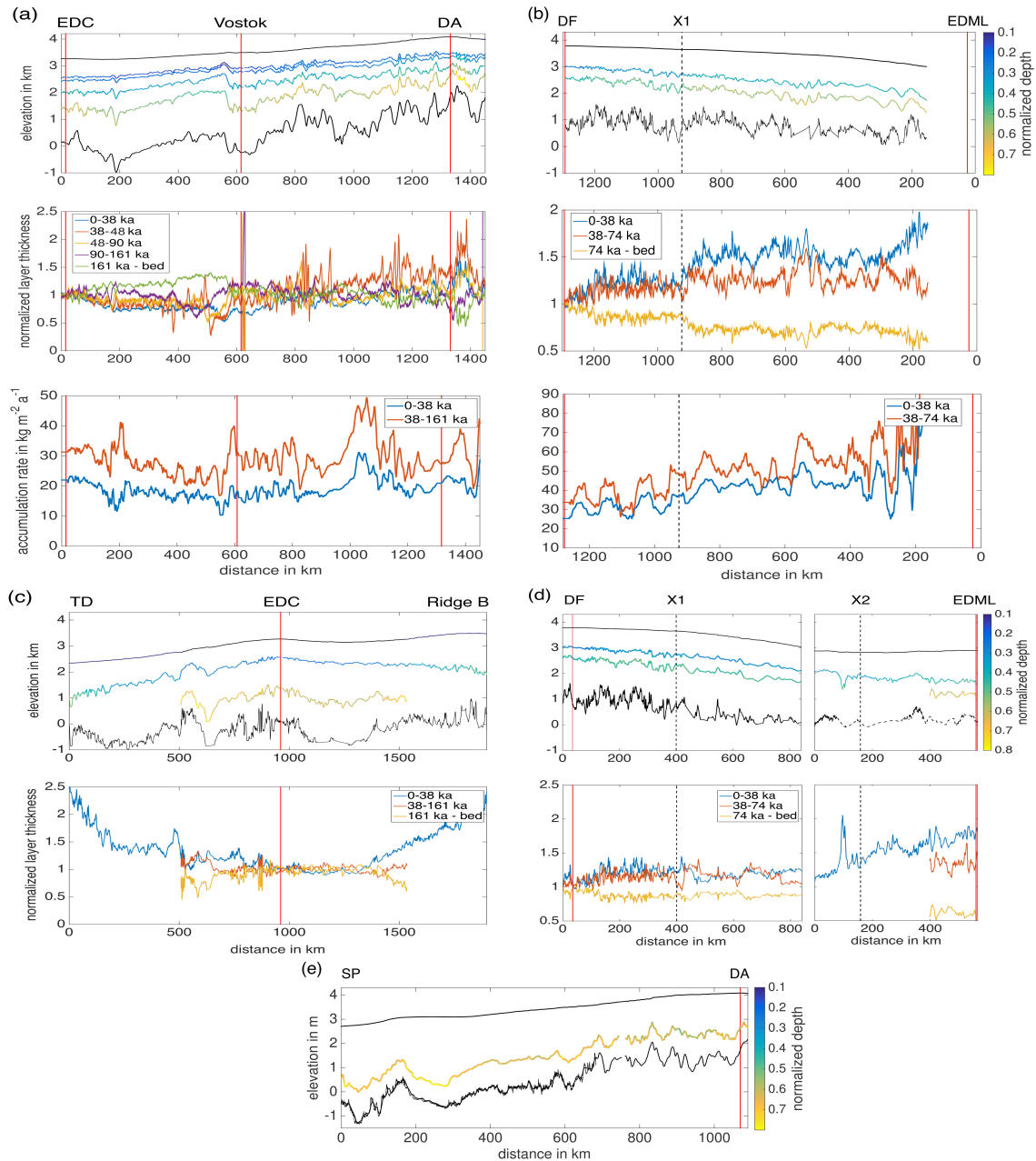


Figure 5.2. Sections of some example profiles. The profile locations can be identified via the drill sites and crossing points (vertical lines and labels at top of sub-figures). Profiles are marked by red ((a) and (b)), and yellow lines ((c), (d) and (e)) in Fig. 5.1. Top panels show the elevations (WGS84) of ice surface, bed and IRHs. Colors scale with normalized IRH depths. The second panels show normalized layer thicknesses, with respect to their normalized thicknesses at EDC (a and c), and DF (b and d), respectively. The bottom panels of (a) and (b) show the mean accumulation rates along these profiles from the two most extensively interpreted layers.

The relative thicknesses of the uppermost and bottom layers are overlaid by a trend of increasing and decreasing layer thickness, respectively, from DF to EDML. This is equivalent with a larger normalized IRH depth (this is also seen from the brighter IRH color in the top panel) The IRHs dive deeper below the surface and the maximum age at depth decreases towards EDML.

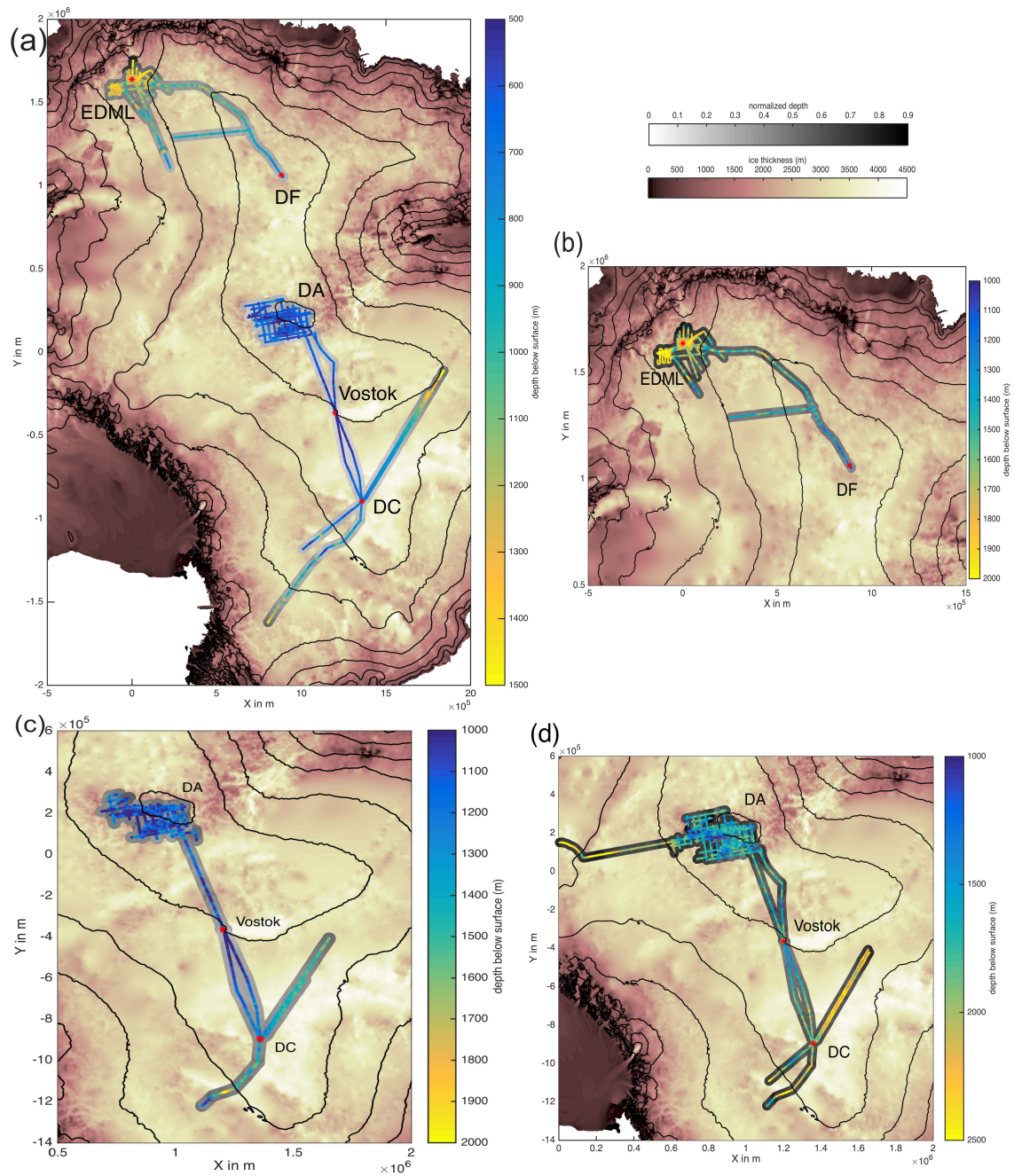
Figure 5.2 c shows the IRH depths and normalized layer thicknesses (relative to the DC layer thicknesses) for the profile from TD towards Progress Station (red profile in CEA in Fig.5.1), which is intersecting the DC–DA profile at the EDC drill site and ending approximately on the northern part of Ridge B. The IRH colors get brighter and the bottom layer (yellow) thinner with increasing distance from DC in both directions, TD and Ridge B. Again, this means the IRHs move closer to the bed and the extrapolated maximum age is younger than at DC. The same applies towards South Pole, as seen in the IRH elevation and normalized depth for the 161 ka IRH in the SP–DA profile (Fig. 5.2 e). The normalized IRH depth towards SP is in the same range or deeper than at DA, where in turn the normalized thickness of the bottom layer is smaller than at DC. Figure 5.2 d shows IRH depths and layer thicknesses for the profile from DF via crossing point X1 towards X2, concatenated with the approximately perpendicular profile towards EDML via X2 (red profiles in region DML in Fig. 5.1). The IRH depths and layer thicknesses confirm the trend of IRHs moving deeper from the plateau towards the coast.

Figures 5.3 a– 5.3 d show the spatial distribution of the absolute and normalized depths of the IRHs for all RES profiles. The normalized depths show smooth lateral variations, with a broad pattern of deepening IRHs (darker gray) towards the ice-sheet margins and towards South Pole (see 161 ka IRH, Fig. 5.3 d). The absolute depths are also overlaid by this trend of deeper IRHs at the margins. Hints about the maximum age are provided by the distribution of the normalized depth of the 161 ka IRH (Fig. 5.3 d). The brighter the gray, the thicker the ice fraction that is older than 161 ka.

5.4.2 Mean accumulation rates

5.4.2.1 Profile Dome Concordia – Vostok – Dome Argus

For deriving accumulation rates, we only use the two most extensively traceable IRHs in the CEA region. These are the shallowest (38 ka) and the deepest (161 ka) IRHs of the top panel of Fig. 5.2 a. The bottom panel of Fig. 5.2 a shows the mean accumulation rates derived from these two IRHs along the DC–DA profile. DC has Hc-LG accumulation rates of about $22 \text{ kg m}^{-2} \text{ a}^{-1}$, with a decreasing trend towards the south-west. The region with the highest accumulation rates along this profile is about half-way between Vostok and DA, where Hc-LG accumulation rates are about $30 \text{ kg m}^{-2} \text{ a}^{-1}$. The LG-PG accumulation rates show more or less the same pattern, however with 5 to $10 \text{ kg m}^{-2} \text{ a}^{-1}$ higher values



and stronger variations. Especially the pronounced maximum between Vostok and DA is much more distinct.

5.4.2.2 Profile Dome Fuji – EDML

The bottom panel of Fig. 5.2b shows the mean accumulation rates in the Hc-LG and LG intervals for the RES profile in the DML region, starting a few kilometers east of EDML (reversed x-axis) and following the ice divide to DF. In general, the trend in this profile goes towards higher accumulation rates ($70 \text{ kg m}^{-2} \text{ a}^{-1}$, and $60 \text{ kg m}^{-2} \text{ a}^{-1}$ for the LG, and Hc-LG intervals, respectively) towards EDML. At the beginning of the profile (close to EDML) there are huge variations on a short horizontal scale. In the direction of DF the accumulation rates constantly decrease. At DF we get $26 \text{ kg m}^{-2} \text{ a}^{-1}$, and $34 \text{ kg m}^{-2} \text{ a}^{-1}$, respectively for the Hc-LG and LG intervals. The LG accumulation rates stay around $10 \text{ kg m}^{-2} \text{ a}^{-1}$ above the Hc-LG ones along the whole profile. Especially for the older time interval and towards DF, there are some abrupt jumps of about $10 \text{ kg m}^{-2} \text{ a}^{-1}$ in the accumulation rate values in relatively regular horizontal distances (about 50 km). These jumps might be induced by the divergence correction based on PISM results and are discussed below.

5.4.2.3 Spatial distribution of accumulation rates

The spatial distribution of Hc-LG mean accumulation rates (Fig. 5.4a) reveals smaller accumulation rates in the center of the ice sheet, i.e. the DC-DA profile and the AGAP grid. From DC towards the coast, the accumulation rates increase with decreasing distance to the ice-sheet margins. In the DML region the accumulation rates are generally higher than in the CEA region, and likewise show an increasing trend towards the coast.

The accumulation rates from the LG-PG interval in the CEA region show a similar pattern to the Hc-LG ones, with increasing accumulation towards the ice-sheet margins (Fig. 5.4b). The absolute values of the accumulation rates are generally higher for this time interval (about 1/2 times higher). In the profiles towards the ice-sheet margins, there are some particular features, with accumulation rates jumping from low to high and back to low values for several times over a short distance.

The large-scale pattern of LG mean accumulation rates in DML (Fig. 5.4c) resembles the one of the Hc-LG interval. But like in the CEA region, the absolute values of the accumulation rates of the older time interval are slightly higher (about 1/5 times), compared to the Hc-LG ones.

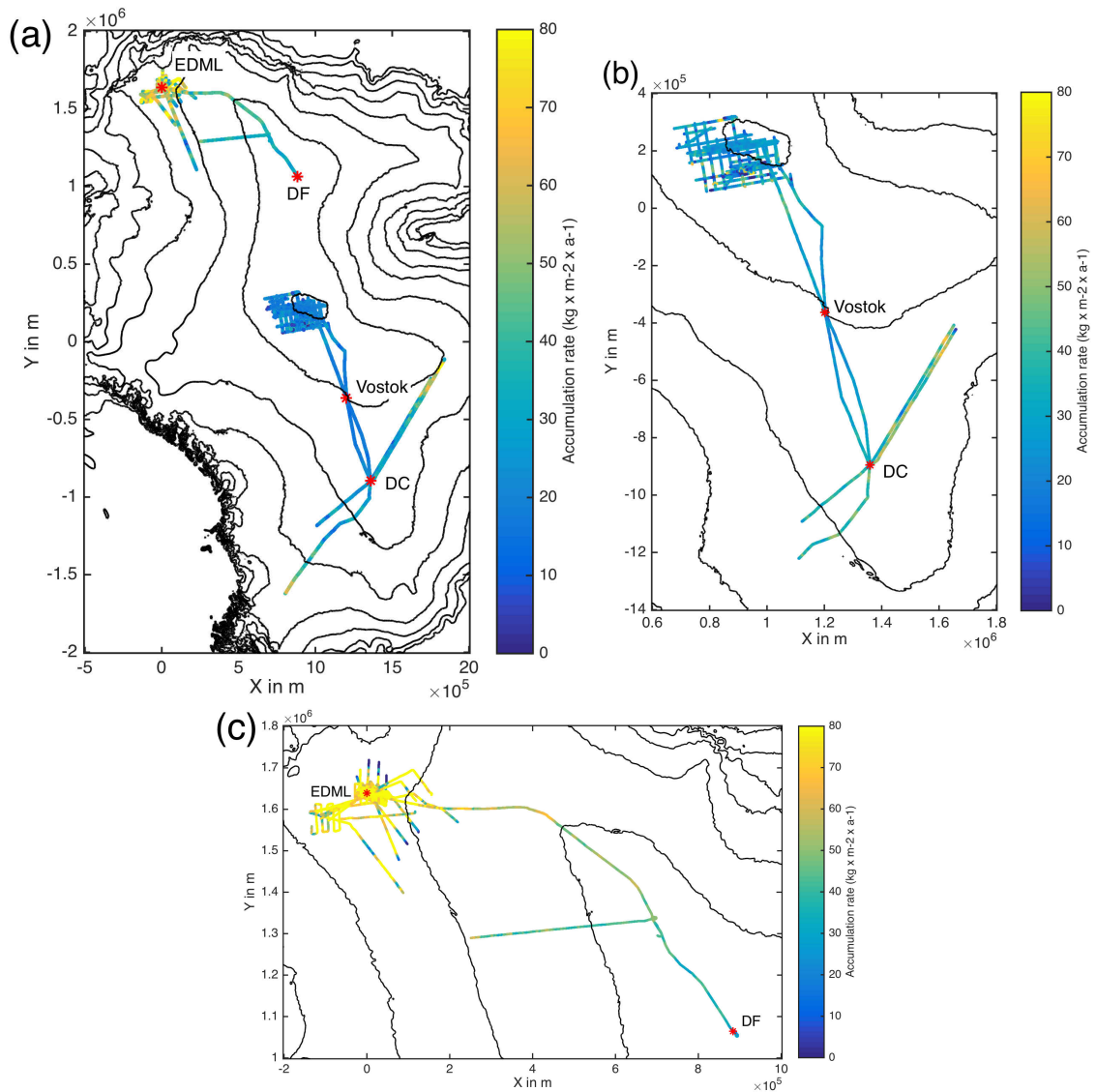


Figure 5.4. The mean accumulation rates we derived for the different time intervals: (a) Hc-LG (0 – 38.2 ka) accumulation rates in both regions, (b) LG-PG (38.2 – 161.1 ka) accumulation rates in the CEA region, and (c) LG (38.2 – 74.2 ka) accumulation rates in the DML region.

5.5 Discussion

5.5.1 Age stratigraphy

We derived the age-depth stratigraphy of a substantial part of the East-Antarctic inland. With the central profile of the CEA region passing EDC and Vostok, we are able to connect the two deep ice cores with four isochronous IRHs and to compare their age scales. Overall, we find a very good agreement of the IRH ages at EDC and Vostok (Table 5.1). The differences lie within the uncertainties of the age scales. Moreover, we are able to expand the age-depth distribution further to the DA region and into the AGAP-South grid.

In the AGAP-South grid we lose two of the IRHs, due to discontinuities in the stratigraphy in regions of former surface erosion by wind scour, changing flow directions or too steep IRHs. The effect of such processes on the IRH stratigraphy are described e.g., by Das et al. (2013), Cavitte et al. (2016) and Holschuh et al. (2014). The EDC age stratigraphy can also be extended along the profiles towards the ice-sheet margins. Furthermore, we achieve a good coverage of the DML region with three long (500–1000 km) profiles inland and a relatively dense grid around the EDML drill site. Especially the combination of all profiles shown in Fig. 5.2 and the spatial distribution of the 38 ka IRH (Fig. 5.3 a) illustrate the extent of the presented age stratigraphy.

We find a broad trend of IRHs deepening towards ice-sheet margins, as seen in the spatial depth distribution (Fig. 5.3) and the profiles DF–EDML and TD–Progress Station (Fig. 5.2 d and 5.2 c). The most obvious explanation is an increase in accumulation rates towards the coast. However, nonuniform bedrock topography or a changing flow mode (e.g., transition to higher basal sliding or plug flow) can also induce the deepening IRHs (Weertman, 1976; Frezzotti et al., 2005; Leysinger Vieli et al., 2011).

The depths of the IRHs with respect to ice thickness gives a good first-order indication where old ice is likely or less likely to be found. Assuming a similar spatial pattern of accumulation rates and flow speeds over the last glacial-interglacial cycles, the distance of the 161 ka IRH from the bed can be considered a proxy of the age at the bed, compared to the age at EDC (i.e. $< \approx 800$ ka). Applying this criterion to our data set, we can likely exclude the locations at Ridge B, DA and South Pole (where covered by our data) to be viable for Oldest Ice.

The constraining factor for the age resolution of our stratigraphy is the traceability/continuity of the IRHs. It was not possible to reliably trace further distinct IRHs between the ones we chose all the way between EDC and Vostok, and Vostok and DA, respectively. Of interest would e.g., be the IRH related to the Toba eruption 74 ka ago, which is relatively distinct in records all over East Antarctica and shows a prominent radar signature in the DML region. One reason for the more discontinuous and weaker expression in our data could be the large-scale erosional features in the DC–Vostok region, which partly even truncate the IRHs. Further illustrative example radargrams and a detailed description of such features between DC and Vostok can be found in Cavitte et al. (2016).

Another region where we had difficulties to continuously trace IRHs is the Gamburtsev Mountain Province. Either due to steeper topography or changing flow regimes the IRHs are disrupted or become too steep themselves to be detectable by RES at some locations (Holschuh et al., 2014). Moreover, megadunes and wind scour further deteriorate the quality of RES stratigraphy in this region (Das et al., 2013). What turned out to be very

beneficial our purposes was the survey design of a dense grid of profiles, with many alternatives to circumvent the locations of truncated horizons.

In DML the IRHs cannot be traced very far from the EDML drill site towards the ice-sheet margin before they are disrupted or disappear. These disturbances are induced by non-uniform bedrock topography and by the onset of the faster ice flow towards ice streams (Karlsson et al., 2012; Rippin et al., 2003b; Bingham et al., 2007; Leysinger Vieli et al., 2011).

What sticks out in our compilation and is somewhat impeding a full continental interpretation, is the ~ 900 km long gap between DF and DA. So far, no attempt to close this gap has been successful, mainly for logistic reasons. With this gap being closed, four deep drill sites and their age scales would be connected all at once and a zonal section of the age stratigraphy through the whole EAIS made available. We therefore recommend to tackle this gap in some joint community efforts.

Data quality is the primary constraint for obtaining reliable age stratigraphies of ice sheets. However, another constraining factor, in particular when it comes to the lateral extent, is the efficiency of methods used to trace IRHs. Especially manual and, to a lesser degree, also semi-automatic tracing schemes of IRHs in large data sets, are very time consuming. The overall yield of the number of IRHs that are continuous over a full data set is comparatively small. In view of the ambitions to finally deriving a large-scale stratigraphy of the whole of East Antarctica by combining multiple available data sets, more efficient methods need to be used. This could be fully automatic tracing (e.g. Sime et al. (2011); Panton (2014)), e.g., by determining signal phase gradients or using additional IRHs that do not directly intersect ice cores, as successful carried out by MacGregor et al. (2015a) for the Greenland Ice Sheet. The dating can then either be accomplished in relation to other, more continuous IRHs, or by using educated age guesses from ice-flow models incorporating age tracers. However, whereas it is possible for the Greenland Ice Sheet to separate distinct age sequences by their radiostratigraphic expression alone, especially the dating of IRH segments which cannot be directly related to ice-core sites could be more challenging for East Antarctica, as the dating relies on horizontally overlapping dated IRHs and thus good RES-data coverage. As a technical requirement, the tracking of signal phases in radar data is only possible with coherent radar data with preserved phase information. This would exclude all older data without phase information, as we use for the DML region.

Regarding the age stratigraphy, our data provides a basis compilation of age-depth distribution of the EAIS. We therefore suggest that this compilation can provide useful constraints for the evaluation of those ice-flow models which incorporate age tracers.

5.5.2 Accumulation rates

Beyond using the age-depth stratigraphy as a constraint for ice-flow models or the qualitative description of flow disturbances, the layers themselves could be used to estimate past accumulation rates. However, as pointed out above in comparison to approaches which only use shallow layers, deeper layers require the consideration of flow history and especially flow divergence. In this section we will discuss the comparison of our accumulation estimates to other, already published ones. We want to stress that our objective is not to provide a better estimate of accumulation, but to evaluate the usability of a state-of-the-art continental ice-flow model with a simple approach to extract accumulation rates for this purpose.

Our Hc–LG accumulation rates at EDC and Vostok are in the same range as the accumulation rates derived from the ice cores (Veres et al., 2013; Bazin et al., 2013). At EDC we get a value of $22.0 \text{ kg m}^{-2} \text{ a}^{-1}$. The mean value of the accumulation rate, derived from the EDC core down to the depth of the 38 ka horizon, is $0.0224 \text{ m(i.e.) a}^{-1}$ or $20.5 \text{ kg m}^{-2} \text{ a}^{-1}$ (density of ice $\rho_{ice} = 917 \text{ kg m}^{-3}$). The mean accumulation rate for the same time interval from the Vostok ice core is $15.9 \text{ kg m}^{-2} \text{ a}^{-1}$. We get a value of $18.1 \text{ kg m}^{-2} \text{ a}^{-1}$ at this location. For the LG–PG time interval, however, we get substantially higher mean accumulation rates, compared to the ice cores' accumulation rates. At EDC we get a value of $31.3 \text{ kg m}^{-2} \text{ a}^{-1}$ and at Vostok $30.6 \text{ kg m}^{-2} \text{ a}^{-1}$. The mean values derived from the EDC and Vostok ice cores for the respective depth intervals are $18.2 \text{ kg m}^{-2} \text{ a}^{-1}$ and $15.6 \text{ kg m}^{-2} \text{ a}^{-1}$, respectively.

In Fig. 5.5 we compare our results for the mean accumulation rates along the EDML–DF profile with those from Huybrechts et al. (2009) (dashed lines). Huybrechts et al. (2009) derived accumulation rates for the same profile, using a more complex nested model for the specific flow conditions applicable at an ice divide. In that way they took into account the horizontal movement of the ice that was originally deposited further upstream and therefore might have experienced accumulation rates that differed from those at the current location. The larger scale pattern of our Hc–LG results fits well with the according time intervals from Huybrechts et al. (2009), with our values being slightly higher and with stronger variations. Our values for the older LG interval are higher than the Hc–LG results. In contrast, Huybrechts et al. (2009) get considerably smaller accumulation rates for their oldest three time intervals, which match our LG interval when taken together.

The stronger variations in our results, which get especially strong towards the EDML ice-core site, could indicate that our method is more sensitive to strong bedrock undulations on the scale of the PISM resolution. At 10 km resolution the model might not be optimally suited to capture the small-scale ice-flow patterns and divergence variations that occur above a rugged bed topography. Additionally, we did not take into account the horizontal flow of particles for correction of divergence, which has an impact in regions with strong

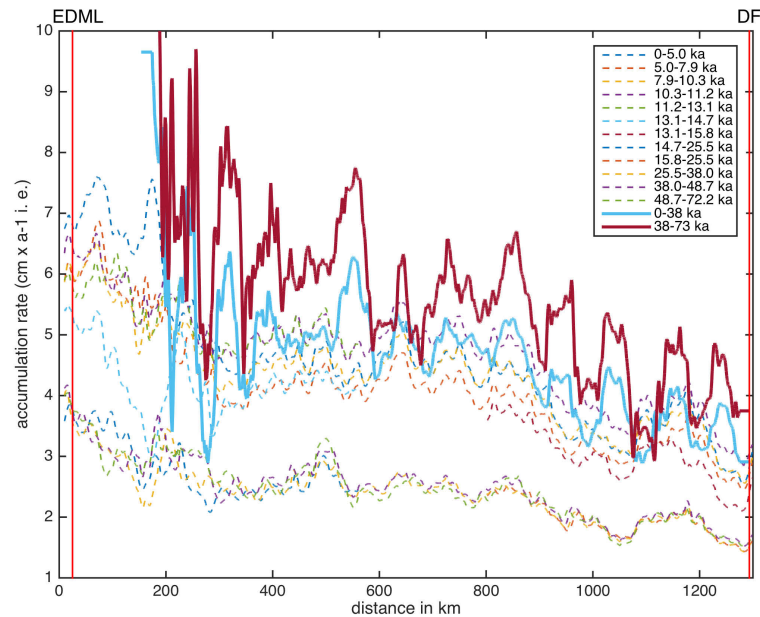


Figure 5.5. Our results (solid lines) for the mean accumulation rate for the profile connecting EDML and DF in the DML region (yellow lines in Fig. 5.1). The dashed lines show accumulation rates derived by Huybrechts et al. (2009) from the same RES profile.

bedrock features such as deep troughs. In those areas the divergence field might change considerably on short horizontal scales as potentially also on vertical scales. This effect increases with older IRHs. Another factor contributing to the differences could be that the location of the ice divide is not exactly reproduced by the PISM run. This could also result in wrong divergence corrections.

A comparison of our results with those of Le Meur et al. (2018) for a profile from EDC about 200 km in the direction of Vostok shows that we get the same trend of decreasing accumulation rates with increasing distance from EDC. Their absolute accumulation rate values are slightly higher than ours. This is to be expected as our Hc–LG layer includes the LGM with lower-than-Hc accumulation. The oldest IRH of Le Meur et al. (2018) has an age of about 600 a and thus their results exclusively comprise the Holocene.

Cavitte et al. (2017) use RES IRHs and a 1D pseudo-steady ice-flow model to investigate temporal changes in the accumulation-rate pattern around EDC. Their results for a profile close to the first 250 km of our EDC–DA profile also show the pattern of decreasing accumulation rates towards the south-west. They show that the accumulation rates decrease from the Holocene to the Last Glacial Maximum, are smallest for the layers bounded by the 10–38 ka and 38–46 ka IRHs, and then slowly increase to higher than Holocene values. Our Hc–LG accumulation rates lie inbetween their Holocene and 10–38 ka values. Our LG–PG accumulation rates are not directly comparable, as we use different time intervals. We have an older ‘oldest’ IRH (161 ka compared to 127 ka), but Cavitte et al.

(2017) use more IRHs and thus get a higher temporal resolution in this time range. Our values are slightly higher (about $3 \text{ kg m}^{-2} \text{ a}^{-1}$) than their maximum values, which they derived for the 121–127 ka interval.

The comparison of our results with other studies, that concentrate on more constrained areas, shows that we seem to get systematically too high accumulation rates, especially for the LG and LG–PG time intervals. We assume that the correction for divergence, which were calculated from the PISM ice-flow velocities (Eq. (5.2)) are too large. With the large-scale objective of our data we cannot constrain the model to a specific region or assumptions like horizontally uniform ice flow. Those would be only valid in the targeted focus region, e.g., in close proximity to dome or ice-divide positions, as shown e.g., by Leysinger Vieli et al. (2011). Such site-specific optimizations in general do require further information on ice-sheet properties, which are not available on a continental scale. Thus, such optimizations result in limitations regarding complexity and resolution of the model due to the computational cost, the basic nexus between resolution and extent.

The obvious next step regarding the application of continental ice-flow models to deduce paleo-accumulation rates from radar stratigraphies would be the consideration of particle trajectories. Such a treatment would account for the spatially changing horizontal divergence to get more realistic values of ice-flow divergence that the ice has experienced since its deposition. The problem with divergence becomes more important with increasing IRH age. Beyond using steady-state velocity fields, improvements could also be achieved by incorporating the time dependence of the flow field and the ice thickness in the model, or at least adjust the divergence correction for layers of different climatic condition. However, paleo spin-ups of ice-flow models rely on the input of paleo-accumulation rates. Hence, the problem of deriving accumulation rates from RES isochrones of different climatic periods is actually an inverse problem.

Although we can neither provide snapshots of past ice-sheet geometry nor flow behavior, a set of ice-sheet internal markers, as those discussed in the previous section, to which the model results could be compared will be of great value to improve the separation of the main factors for paleo-surface submergence, ice-flow velocity, past accumulation and basal melting. With the availability of ever increasing amounts of computing power, formal inverse approaches with data assimilation techniques could use EAIS' present-day age stratigraphy to improve the replication of the ice sheet history by models and reduce uncertainties for runs into the future. Yet, solving this inverse problem for our spatial and temporal scale is computationally not possible by present-day means.

We therefore propose two approaches. First, for dedicated regional studies of paleo accumulation we find it advisable to stick to smaller regions. Within those regions, ice-flow models could be optimized to various ice-sheet characteristics to best represent those conditions. Second, for studies on the continental scale, interpretation of reconstructed

accumulation should be treated with caution, especially at locations where the accumulation rates show abrupt changes.

5.6 Conclusions

We provide a broad age-depth stratigraphy of two separate regions of the East Antarctic Ice Sheet. In Dronning Maud Land we used two isochronous RES IRHs with ages of 38.1 ± 0.7 ka and 74.2 ± 1.7 ka, in Central East Antarctica IRHs with ages of 38.2 ± 0.6 ka and 161.1 ± 3.5 ka. For some profiles in the latter region we could add two more IRHs with ages of 48.3 ± 1.2 ka and 90.2 ± 1.6 ka, yielding four IRHs that are directly connecting the EDC and Vostok drill sites and DA. The broad picture indicates shallower IRHs on the plateau between DA, Vostok and EDC and deepening IRHs towards the ice-sheet margins and South Pole. Some variation of IRH depths also occurs on a smaller scale, which we mostly attribute to distinct, long-wavelength (tens of ice thicknesses) topographic features. Example locations of such topographic features are the Gamburtsev Mountains or the deep trough east of EDC.

We applied a comparatively simple method to infer a large-scale distribution of accumulation rates across East Antarctica. Although the results do partly agree well with published values of accumulation, in some regions our method might be too simplified to get correct absolute accumulation rates for the time intervals in distant past. Even if spatial patterns of accumulation rates seem to be still valid, we consider them rather qualitative indicators than reliable quantitative values at this stage. Improving those estimates requires methodological improvements with more advanced models running in higher spatial resolution.

To further improve the broad interpretation of the East-Antarctic age-depth architecture it would be required to close the gap between DF and DA. This would allow a direct comparison of age scales of the EDC, Vostok, DF and EDML ice cores. This could also facilitate the common interpretation of our two separate regions. For a more complete overview, it would be beneficial to additionally include already existing data from other RES surveys, where possible. This includes, for example, the most recent extensive Oldest-Ice reconnaissance surveys around EDC and DF, the AGAP-North survey and data collected around South Pole. Moreover, several rather coastal surveys might also cover parts of the interior ice sheet and thus be valuable towards a full coverage of the East Antarctic Ice Sheet. Joining different data sets for different regions holds the potential to improve the age resolution, either by providing more crossing profiles to circumvent problematic regions, where many horizons are truncated, or complementing strength and weakness of different radar systems.

5.7 Acknowledgements

This publication was generated in the frame of Beyond EPICA - Oldest Ice (BE-OI). The project has received funding from the European Union's Horizon 2020 research and innovation programme under grant agreement No. 730258 (BE-OI CSA). It has received funding from the Swiss State Secretariate for Education, Research and Innovation (SERI) under contract number 16.0144. It is furthermore supported by national partners and funding agencies in Belgium, Denmark, France, Germany, Italy, Norway, Sweden, Switzerland, The Netherlands and the United Kingdom. Logistic support is mainly provided by AWI, BAS, ENEA and IPEV. The opinions expressed and arguments employed herein do not necessarily reflect the official views of the European Union funding agency, the Swiss Government or other national funding bodies.

The development of PISM is supported by NASA grant NNX17AG65G and NSF grants PLR-1603799 and PLR-1644277.

A considerable part of this survey was acquired during the International Polar Year as part of the project TASTE-IDEA. We thank the logistics field team from various nations and flight crews for support during those expeditions.

T.T.C. was supported by the US NSF grant PLR-1643970

This is BE-OI publication number xxx.

6 Basal roughness of the East Antarctic Ice Sheet and its indications for ice flow and basal thermal state

This chapter is a manuscript in preparation for submission.

Abstract

Basal motion of the East Antarctic Ice Sheet, dependent on the roughness and material of the subglacial bed and the occurrence of water, represents a large uncertainty in ice-flow models. Yet, it is the part of the total flow speed that can change most rapidly and can therefore facilitate rapid variations in the mass balance and stability of the East Antarctic Ice Sheet. In this study we investigate the subglacial properties of the East Antarctic Ice Sheet by statistically analyzing the roughness of the bed topography, which is inferred from radio-echo sounding measurements. The roughness analysis with two roughness parameters enables a classification of the subglacial landscapes below the ice sheet. The roughness parameters are correlated with the flow speed of the ice and basal temperatures. The observed relationships lead to the conclusion that one of the roughness parameters might indicate the thermal condition at the base of the ice sheet. If confirmed by more testing and temperature measurements, this could be used as a new method for basal thaw prediction. Basal thaw from ice-flow models could be validated with this method as it is independent of the models.

6.1 Introduction

Basal motion of the East Antarctic Ice Sheet (EAIS), sliding of the ice over the bed and deformation of the bed itself, is a key factor in the control of ice-flow velocities and thus recognized for its importance in the mass balance of the EAIS (e.g. Shepherd et al., 2006; Ritz et al., 2015; Podolskiy and Walter, 2016). Yet, it is one of the largest uncertainties

in ice-flow models and projections of the ice-sheet response to a warming climate (Ritz et al., 2015). The basal motion is rarely parameterized on physically justified grounds in ice-sheet models, because direct measurements and precise process understanding stay elusive (Roeoesli et al., 2016). Instead, it is mostly constrained by inversion methods for the surface flow speed (Wilkens et al., 2015). The basal motion of the ice depends on small-scale (~ 0.05 m – 10 m) roughness of the bed topography, thermal state (occurrence of water) of the bed and lithology (Weertman, 1957; Nye, 1970; Kamb, 1970; Winsborrow et al., 2010). Li et al. (2010) show that spectral roughness parameters of the topography can be used to deduce the formation (marine or continental) and erosion history of the respective landscape. This allows for drawing inferences about the bed lithology. Jordan et al. (2017) provide a framework that puts subglacial bed roughness and basal thermal state into relation. Therewith, all influencing factors of basal motion are linked by the roughness parameters, which can be obtained from radio-echo sounding (RES) measurements on regional to continental scales.

We calculate two spatial roughness parameters, the root-mean-square (RMS) deviation of the bed elevation $\nu(\Delta x)$, and the Hurst exponent H . H expresses the scaling behavior of ν with increasing point distance Δx . ν and H parameterize the vertical roughness amplitude, and the dominance of long- or short-wavelength roughness, respectively. We therefore synonymously use the names amplitude roughness and wavelength roughness for ν and H , respectively. They have the same prescriptive implication as the more commonly used spectral roughness parameters, the amplitude and frequency roughness parameters (often named ξ and η) (e.g. Taylor et al., 2004; Li et al., 2010; Gudlaugsson et al., 2013), but are easier to obtain from non-uniformly spaced data (Malinverno, 1990). Jordan et al. (2017), also using the spatial parameters, show that the Hurst exponent is related to the waveform abruptness and the scattering behavior of the ice–bedrock interface. They compare the distributions of the abruptness and the Hurst exponent to modeled basal temperatures in north-west Greenland. Their results show low and high bed-reflection abruptness, and high and low H -values at locations with thawed, and frozen bed, respectively. Jordan et al. (2017) emphasize that their method should not be seen as a new diagnostic for basal-water detection. However, their results put into question the previously used method for thawed–frozen bed discrimination by bed-reflection amplitude/abruptness (e.g., Oswald and Gogineni, 2012). We now use a large radio-echo sounding (RES) data set from different regions in East Antarctica. We compare the roughness parameters to flow speed and modeled basal temperatures. Our aim is to investigate if the correlation between roughness and basal temperature (thawed–frozen bed), as derived by Jordan et al. (2017), can be transferred to Antarctica, or is specific of the observed region in northern Greenland and if it could possibly be used as a diagnostic for basal condition in some circumstances.

6.2 Data and method

6.2.1 Radio-echo sounding data

We use a compilation of radio-echo sounding data from more than 20 years of surveying (1994–2017) by the Alfred Wegener Institute (AWI). The source signal is a burst wavelet with a carrier frequency of 150 MHz. The system can be operated in toggle mode, where it is alternating between shots with 60 ns and 600 ns burst lengths. The vertical resolution of each of these bursts in ice is approximately 5 m and 50 m, respectively. The recorded data are stacked to an average trace distance of 75 m and a vertical sampling interval of 13.33 ns. The bed reflection is traced in the differentiated and band-pass-filtered 600 ns data. After one iteration of manual picking on a subset of the data, an auto-picker routine is applied to obtain the maximum horizontal along-track resolution allowed for by the data. The algorithm detects the maximum within a certain time window around the manual picks and also detects the bed reflection between the manual picks, wherever there are manual picks within a distance of 30 traces. The ice thickness at the location x is then

$$d(x) = \frac{c_{ice} 2t(x)}{2}, \quad (6.1)$$

with the two-way travel time (TWT) $2t(x)$ of the radar signal through the ice. We use a radar-wave velocity in ice of $c_{ice} = 168.0 \text{ m } \mu\text{s}^{-1}$. The ice thickness is subtracted from the BEDMAP2 surface elevation (Fretwell et al., 2013) at the respective location to get the bed elevation $z(x)$ (WGS84). Since only relative elevation differences are important for our method (Sect. 6.3.1, Eq. 6.3), we can neglect the higher wave velocity in firn (firn correction). The justifying assumption to do so is that the firn thickness does not substantially change within 1 km, which is the maximum point distance we use for our roughness calculations. For the same reason, the uncertainty in c_{ice} does not affect our results, as we do not expect c_{ice} , averaged over the ice thickness, to change over a horizontal distance of 1 km. The uncertainty on bed-elevation differences thus depends on the uncertainty on surface elevation, the vertical resolution of the radar system and picking accuracy. To assess the accuracy of the derived bed elevation, we conduct crossover analyses at locations of crossing RES profiles. The root-mean-square (RMS) error on the elevation differences, which are equal to the difference in ice thickness Δd at crossover points, for the AWI data is

$$\sigma = \sqrt{\frac{1}{N} \sum_{i=1}^N (\Delta d - \overline{\Delta d})^2} = 45 \text{ m}, \quad (6.2)$$

with a mean elevation difference $\overline{\Delta d} = 56 \text{ m}$ from $N = 3441$ measurements.

Additionally to the AWI data, we recalculate the roughness values with our method for a number of publicly available RES data sets. Our intention is to achieve a consistent

processing flow for all the data sets, covering a large portion of the EAIS when combined. Some of these data have already been interpreted with respect to bed roughness and radar scattering behavior (e.g., Young et al., 2011; Wright et al., 2012; Bellot, 2012; Creyts et al., 2014; Young et al., 2016, 2017). However, we re-interpret them as part of the combined product. The data we incorporate in our evaluation are:

1. The final ice-thickness product of the Antarctica’s Gamburtsev Province Project (AGAP) -South data, collected by the Lamont-Doherty Earth Observatory (LDEO) (Antarctica’s Gamburtsev Province Project - South, 2008/09; Wolovick et al., 2013). The data were pulse compressed and then migrated with a 1D synthetic-aperture algorithm, which assumes point scattering targets following Hélière et al. (2007). The final resolution of the processed data is 13 m in the horizontal and 7 m in the vertical. The bed was picked with a semi-automatic system using the steepest vertical gradient. The output is filtered along track at 60 m (Wrona et al., 2018). The RMS error on elevation from crossover analysis is $\sigma = 69$ m, with $\overline{\Delta d} = -3$ m (N=721) (Creyts et al., 2014).
2. Bed picks of the AGAP-North data (Antarctica’s Gamburtsev Province Project - North, 2008/09; Bell et al., 2011; Ferraccioli et al., 2011), collected by the British Antarctic Survey (BAS) with the PASIN (Polarimetric Airborne Survey Instrument) radar system. Average horizontal sampling and vertical resolution (calculated from 12 MHz signal bandwidth) are both 10 m. The RMS error is $\sigma = 46$ m, with $\overline{\Delta d} = 28$ m (N=2081).
3. Operation IceBridge HiCARS 1L2 Geolocated Ice Thickness product (Blankenship et al., 2011, updated 2017), from data collected as part of the ICECAP (International Collaborative Exploration of the Cryosphere through Airborne Profiling, Young et al., 2011) project. The data were pulse compressed and synthetic-aperture processing was applied. TWT-to-depth conversion was conducted with a wave velocity of $c_{ice} = 168.5 \text{ m } \mu\text{s}^{-1}$. The average horizontal sampling and vertical resolution of the processed data is 20 m and 8 m, respectively. The maximum uncertainty on ice thickness is given as $\sigma = 70$ m.
4. Ice thickness from the Old Ice A site (OIA) survey around Dome C in 2016. This survey was part of the US–Australian ICECAP follow-up project ICECAP II (Young et al., 2017). The data were range compressed and 1D focused synthetic-aperture processing, following Peters et al. (2007) was applied. The data were resampled to an average along-track sampling of approximately 22 m and the vertical resolution is 8.4 m in ice. The RMS error on ice thickness/bed elevation is $\sigma = 80$ m (Cavitte et al., 2016; Young et al., 2017).

The different horizontal sampling and vertical resolution of the different data sets impact on the uncertainty on roughness parameters, whereby the RMS errors on bed elevation directly propagate into the roughness-parameter uncertainty. However, the error estimates are very conservative, especially for the data with synthetic-aperture processing applied, i.e., the AGAP, IceBridge and OIA data. The large differences in ice thickness at crossover points in these data arise mainly from the different directions of the RES profiles, because synthetic aperture migration only works in the along-track direction. This effect is described in more detail in Young et al. (2017). The accuracy for along-track interpretations of these data should therefore be higher than for the AWI data, due to their higher vertical resolution. Different horizontal sampling results in slightly different values for the roughness parameters. Nevertheless, we decided to keep the original horizontal sampling of the ice-thickness data instead of resampling all data sets to the AWI sampling interval (which is the coarsest), in order to retain all the information contained in each data set. The effect of different horizontal sampling on the roughness parameters and the implication of this approach for our interpretation is described in more detail in Sect. 6.4.2.

6.2.2 Roughness parameters

We derive the roughness parameters $\nu(\Delta x)$ and H from the bed elevation as statistical values for 10 km windows with a 1 km along-track sampling. The first step is to remove the long-wavelength trend from each 10 km window by computing a linear least-square fit in that window. Afterwards, all pairs of points in each window are binned by their distance (lag) Δx . We choose a widths of 100 m, so that the smallest bin still contains points for the data with the coarsest horizontal sampling (AWI data with average trace distance of 75 m), and a maximum lag of 1 km. The trace distance of the AWI data corresponds to about 2 times the first Fresnel zone of radar system for an ice thickness of 3 km. Despite the different horizontal sampling of the data sets, we use the same parameters for all data. The RMS deviation ν is calculated for each bin:

$$\nu(\Delta x) = \sqrt{\frac{1}{N} \sum_{i=1}^N (z(x)' - z(x + \Delta x)')^2}. \quad (6.3)$$

$z(x)'$ is the bed elevation after the long-wavelength trend removal. The elevation differences of all pairs of points (N : number of pairs) in the 10 km window which have a lag Δx within one bin (e.g. 1–100 m, 101–200 m, etc.) are included in the calculation of ν of this specific lag bin. Results for bins with five or less pairs of points are discarded. The detrending of the profiles before the calculation of ν prevents an over-estimation of large-wavelength roughness, when e.g. only the rise of a hill is included in the window (Shepard et al., 2001; Siegert et al., 2005). The effect of the detrending process on our results is small, as we only use small lag sizes, compared to the window sizes. However,

the roughness values for the larger lags become slightly smaller, compared to the results without trend removal.

The results for ν are then used to calculate the Hurst exponent H for each 10 km window. H is the slope of ν over lag distance in a log–log plot. We use all 10 lags, i.e. the results for ν from the 50–950 m bins, to derive the slope.

$$\nu(\Delta x) = \nu(\Delta x_0) \left(\frac{\Delta x}{\Delta x_0} \right)^H, \quad (6.4)$$

with a reference horizontal lag Δx_0 . We only use the H of windows containing more than 5 measuring points of ν in all 10 bins.

6.3 Results

6.3.1 Roughness parameters

We derive ν for 10 different lag bins for the combined data set. The spatial distribution of the 250 m lag results (lags in the range 201–300 m) is shown in Fig. 6.1 c. Regions with different roughness are readily identifiable. The Dronning-Maud uplands show comparatively high ν values. The region with the largest vertical roughness amplitudes is the Gamburtsev-Mountain province around Dome A. South-west of Kohonen Station (EPICA Dronning Maud Land (EDML) drill site), there is an area which is very smooth compared to the surrounding regions. The pattern of high and low roughness values (ν) is similar for all lags, but the absolute values increase with increasing lag.

The spatial distribution of the Hurst exponent is shown in Fig. 6.1 d. The distribution seems slightly smoother than that of ν . The region south-west of EDML again stands out as having very low values for H . The Gamburtsev Mountains and the mountain range in DML show high H values (long-wavelength dominance).

6.3.2 Landscape classification

Li et al. (2010) introduce a way to classify landscapes geomorphically by means of the two roughness parameters. Classes I and II are characterized by small roughness amplitudes, which, according to Li et al. (2010), gives an implication of comparably warm and fast ice flow with high erosion. The long-wavelength dominance of Class I points towards a marine setting, as substantial deposition is necessary to drape the short-wavelength roughness. Class II, in contrast, with a roughness dominated by short wavelengths, is interpreted as a continental setting or a setting with less sediment deposition. The high roughness amplitudes of Class III and Class IV indicate a mountainous region with little erosion, as present at locations with cold bed and slow ice flow. Class IV landscapes

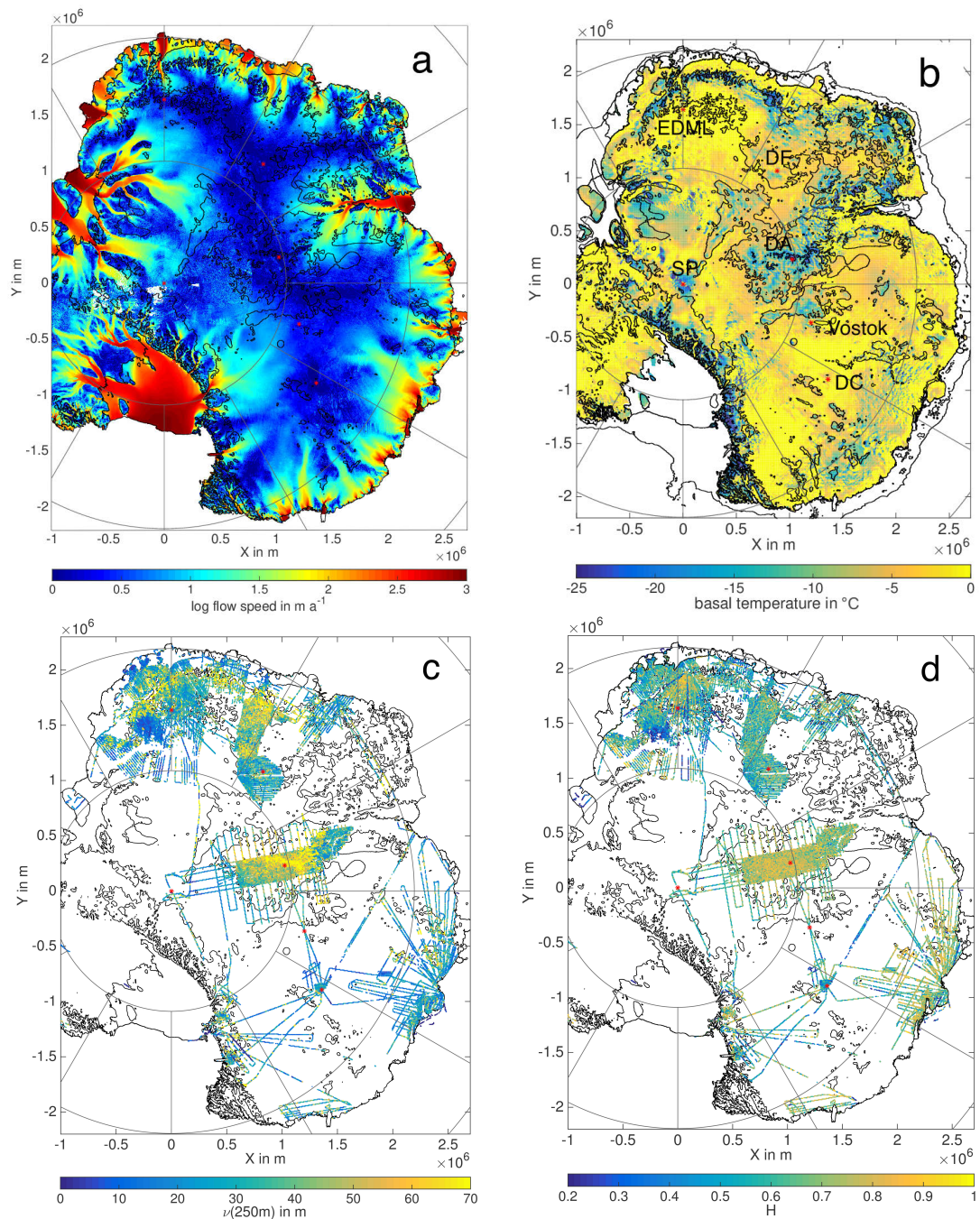


Figure 6.1. East Antarctica with (a) MEaSUREs flow speeds (Mouginot et al., 2017a, b), (b) basal temperatures relative to the pressure melting point (Liefvering and Pattyn, 2013), (c) results for ν for the 250 m bin (Δx in 201–300 m), and (d) results for H . Contour lines indicate topographic features. Red points mark Dome A (DA) and the drill sites Dome C (DC), Vostok, South Pole (SP), Dome F (DF) and EPICA Dronning Maud Land (EDML).

show some indication that erosion and deposition must have taken place, as the short-wavelength roughness is diminished compared to Class III landscapes.

For a large-scale characterization of the East-Antarctic subglacial landscape, we combine the two roughness parameters, ν and H . The distribution of H versus ν for all data is given in a scatter plot in Fig. 6.2. We adjust the x-axis to $3.5\nu/\Delta x$ to get a normalized range. The distribution shows that for small amplitude roughness (ν), all wavelengths appear

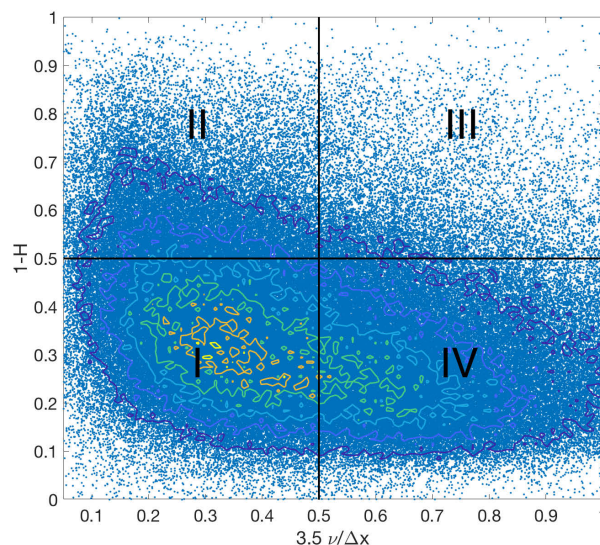


Figure 6.2. Scatter plot of $1 - H$ over $3.5\nu/\Delta x$ and landscape classes after Li et al. (2010). The colored contour lines indicate the density of points.

in an equal measure. The higher the roughness amplitude, the higher the ratio of long-wavelength dominance (high H , small $1 - H$). The number in each quadrant gives the landscape class after Li et al. (2010), derived from the combination of high and low values for ν and H . The normalization of the roughness-amplitude values means that the values can only be judged high or low with respect to other regions covered by our data, rather than high or low in general. However, there is no universal scale for all landscapes and we have presumably covered a good part of the roughness range, as we investigate a large area with different settings from sub-sea-level basins to high mountain ranges. H should always be in the range 0–1 for time or space series with self-affine scaling behavior, which is observed from all natural topography (Malinverno, 1990; Shepard et al., 2001). Self-affinity is a more general form of self-similarity where the statistical characteristics stay the same for various length scales, but horizontal and vertical coordinates need different scaling factors. Figure 6.2 shows that the majority of our data can be assigned to Classes I, II and IV.

The spatial distribution of landscape classes for our data are shown in Fig. 6.3. Negative

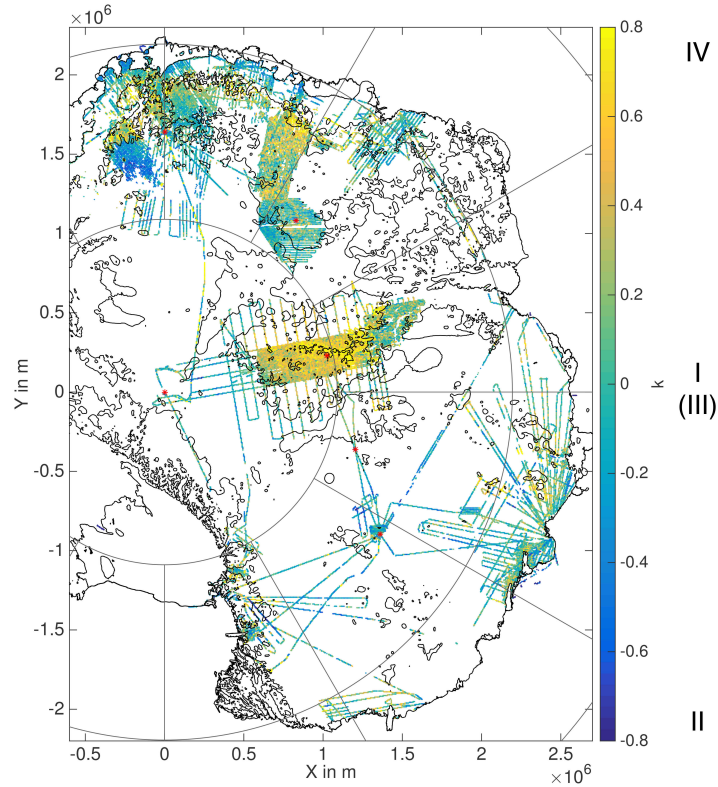


Figure 6.3. Spatial distribution of the parameter $k = 3.5\nu/\Delta x - (1 - H)$ for landscape classification. Roman numerals give the classes after Li et al. (2010). k values around zero indicate either Class I or Class III landscapes, however, Class III hardly occurs in our data set (see Fig. 6.2).

values of the parameter $k = (3.5\frac{\nu}{\Delta x}) - (1 - H)$ indicate Class II landscapes, positive values indicate Class IV, and values around zero indicate Class I. Values around zero can also indicate Class III, but this class comprises only a minor proportion of our data. Class III can be separated from Class I by its high roughness amplitudes in Fig. 6.1 c. The distribution shows that the majority of our study area can be assigned to Class I. The high uplands in DML, and the Gamburtsev Mountains show Class IV properties. A few regions, mostly basins or regions with low bed elevations, are Class II landscapes, most prominently the smooth region south-west of Kohnen.

6.3.3 Hurst exponent and basal temperature

Jordan et al. (2017) show that the Hurst exponent is inversely proportional to the waveform abruptness of the bed reflection. They then compare the abruptness and H to modeled basal temperatures with the result of a rather high abruptness and low H at frozen, and low abruptness and high H at thawed/temperate locations. This contradicts the former interpretation of RES data with respect to thawed region detection by strong and

specular bed reflections. We investigate if we can find the same relation between H and bed condition for our data, or if it is distinctive of the region investigated by Jordan et al. (2017). The large amount and spatial extent of our combined data set, with profiles from regions of different glaciological and geomorphical settings is an excellent test case for this. We analyze our roughness results with respect to their relation to basal temperature T , using modeled temperatures from Liefvering and Pattyn (2013) for the comparison. All temperatures we state below are given relative to the pressure melting point (pmp). Figure 6.4 shows the distribution of H and ν for different temperature bins. The mean values of both H and ν decrease with increasing temperature. The mean and standard deviation of H for the whole data set are $\bar{H} = 0.65$ and $\sigma_H = 0.17$.

Figure 6.5 shows the behavior of the mean of H with temperature. The error bars indicate double the standard deviation of the mean (95%-confidence interval). The temperature bins are the same as for Fig. 6.4 plus one small bin with $-0.01^\circ\text{C} \leq T < 0^\circ\text{C}$, chosen to catch the negative temperatures close to the pmp. Furthermore, we subdivide the data by the three landscape classes to trial a geomorphic dependence on the relation between H and T . The behavior of H with T varies for the three landscape classes. Taking all the data together, there is a slight increase in H when temperatures rise above the pmp. Of the binned data sets this increase is only existent in the Class II data. As a whole, analysis of this data set cannot confirm the significantly higher H values in regions with basal temperatures above the pmp, compared to regions with temperatures below the pmp, that are found by Jordan et al. (2017) in north-west Greenland. Our results show higher values for H at locations with basal temperatures below -5°C than above 0°C .

6.3.4 Roughness and flow speed

For application in ice-flow models a physically justified parametrization of the subglacial roughness is needed to reliably calculate the basal drag and its influence on flow speed. To investigate the relation of roughness and flow speed, we compare our roughness results with the MEaSUREs ice-flow velocities (Mouginot et al., 2017a, b). Because of a significant difference in the roughness parameters for different basal temperatures (Sect. 6.3.3), we bin our data by temperature. The relationship between the roughness parameters and flow speed are shown in Fig. 6.6. The data points of these curves are the mean values of all points in the respective temperature and flow speed bin. Flow-speed bin width are 2 m a^{-1} . The error bars give the 95%-confidence interval.

Both roughness parameters show strong variation at high flow speeds ($v > 100\text{ m a}^{-1}$). At flow speeds below $\sim 20\text{ m a}^{-1}$, ν is decreasing with increasing flow speed. The behavior of H with increasing flow speed is strongly dependent on basal temperature. Fig. 6.6 c shows that H decreases with increasing flow speed at cold-bed locations with temperatures below -5°C relative to pmp. At thawed-bed locations, in contrast, H increases with

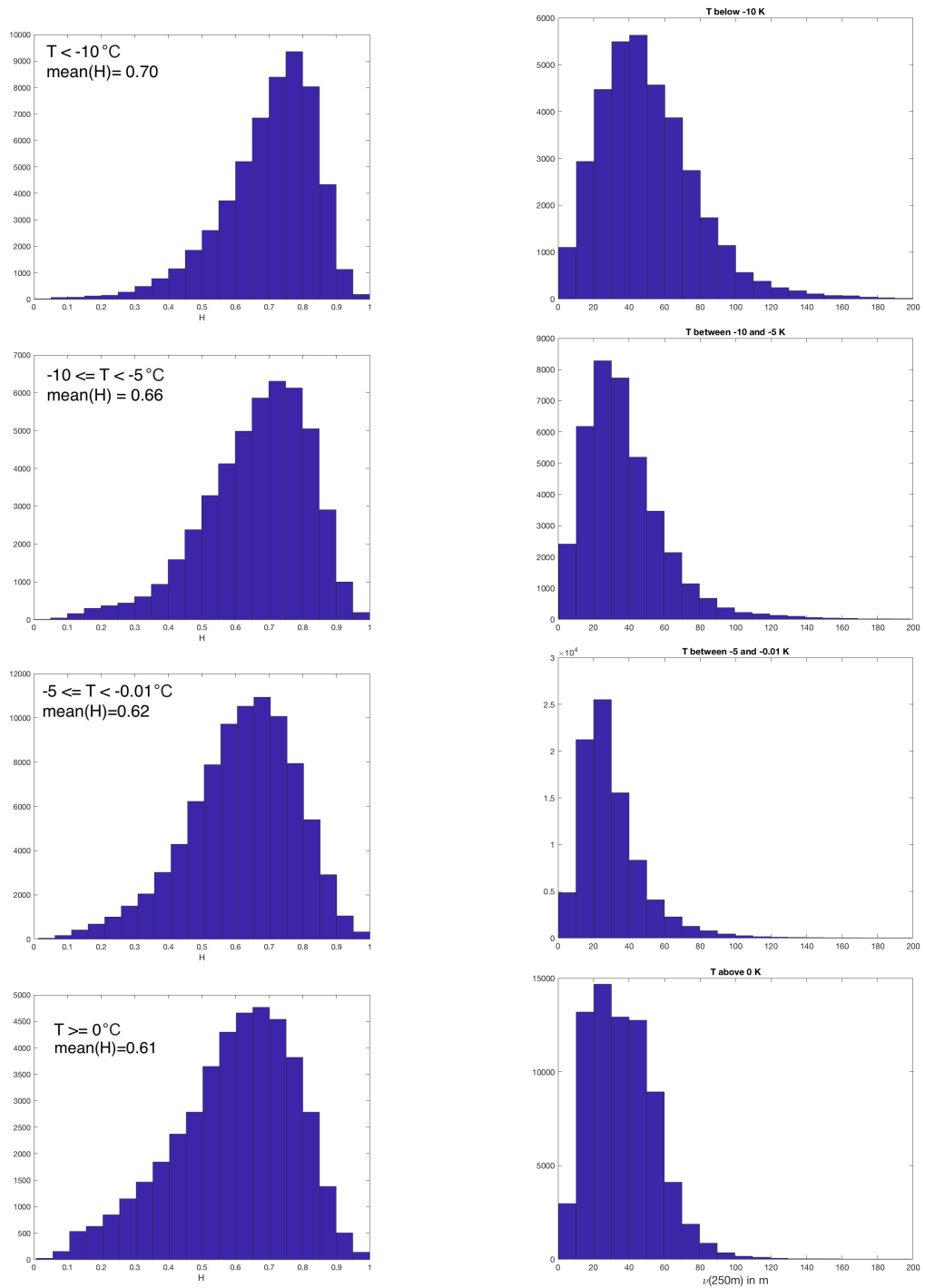


Figure 6.4. Frequency of H (left column) and ν (right column) values for different bins of basal temperature. Temperatures are relative to the pressure melting point. Y-axis is frequency.

increasing flow speed. Furthermore, these curves show that the mean of H is systemati-

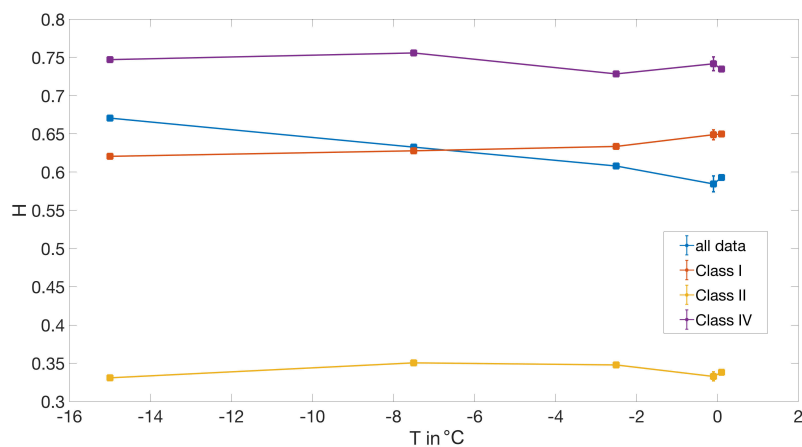


Figure 6.5. Behavior of H with basal temperature for all data, and data subdivided by landscape classes. Temperatures are given relative to the pressure melting point.

cally decreasing with increasing T at locations with flow speeds below 15 m a^{-1} . This is opposite to the relationship that Jordan et al. (2017) found. The relationship in our data flips between flow speeds of $50\text{--}100 \text{ m a}^{-1}$, however, with strong variation in H at high flow speeds and for all temperature ranges.

6.4 Discussion

6.4.1 Landscape classification

Our results show that most regions inland can be assigned to Class I (green in Fig. 6.3). According to Li et al. (2010), these landscapes are characterized by a warm bed or fast ice flow with some erosion taking place and were probably exposed to a marine setting with significant sediment deposition. However, Wright et al. (2012) and Rippin et al. (2014) argue that the diminished short-wavelength roughness does not necessarily indicate a thick covering of sediment, but can also arise from very intense erosion.

The large mountain ranges of the Gamburtsev Mountains and the range bordering DML in the North are classified as Class IV. This class is characterized by a high roughness amplitude, indicating a cold bed and slow ice flow with almost no erosion. This confirms the work of Jamieson et al. (2010) and Creyts et al. (2014), who found the Gamburtsev Mountains have been preserved by a cold ice sheet with almost no erosion. However, the long-wavelength dominance (large H) indicates slight deposition or erosion of small-wavelength topography since the orogeny of the Gamburtsev Mountains. This could indicate that the location was exposed to warmer, faster ice flow for a short time in the past or it is the result of marginal erosion acting over a longer time frame.

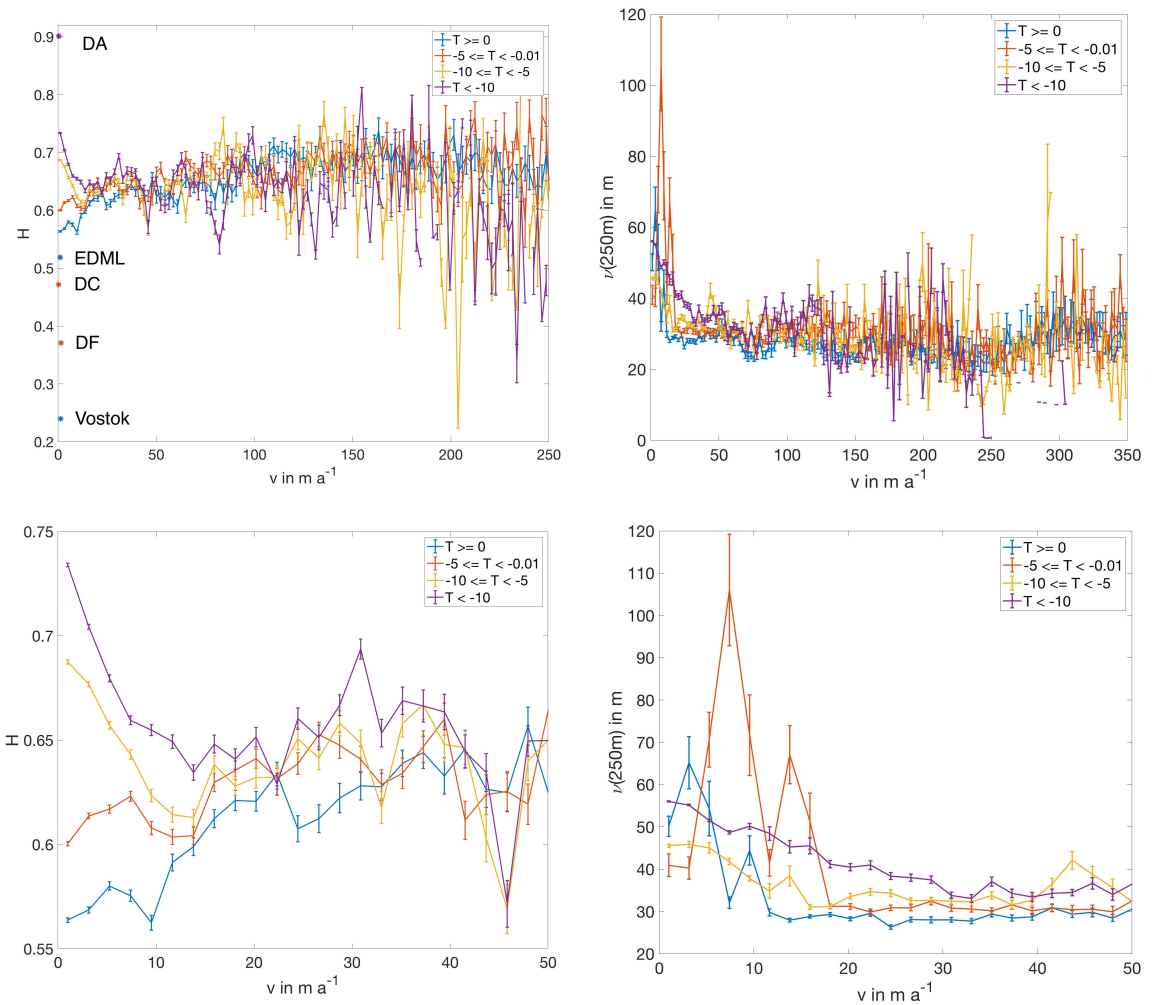


Figure 6.6. Variation of (a) H and (b) ν with flow speed for three different temperature (relative to pmp) ranges. (c) and (d) are zooms on small flow speeds.

The basin south-west of Kohlen is a prominent Class II region. It is probably a marine basin, filled with sediment and therefore being extremely smooth. According to Li et al. (2010), marine deposition would be associated with Class I (long-wavelength dominance). However, Rippin et al. (2014) also found the Class II signature for the Robin Subglacial Basin next to the Institute Ice Stream and argue that H is not very meaningful at extremely smooth locations. Simply speaking, if there is close-to-zero amplitude roughness, the predominating wavelength of the roughness is meaningless. The interpretation of a marine basin south-west of Kohlen is strengthened by the bed being situated below sea level in this region. The results of an extensive geophysical survey, including RES, gravimetrics and magnetics, just south of this region indicate a 3km-thick sediment layer under the northern tributary of Slessor Glacier (Rippin et al., 2003a; Shepherd et al.,

2006). Thick sediment cover is also detected by Diez et al. (2018) at this location. These studies cover only the southernmost part of the smooth area in our data, however, it is reasonable to assume that the sedimentary basin continues to the north. To confirm this assumption, further geophysical surveying (seismics, magnetics, gravimetry) is required. Other regions classified as Class II are the region south of Dome C and some deep parts of the Aurora and Wilkes Subglacial Basins. The channel and fjord structures, and the paleo-hydrological systems of these basins, including the potential influence on ice-sheet stability and mass balance, are described in detail in Young et al. (2011); Wright et al. (2012) and Jordan et al. (2010).

6.4.2 Does the Hurst exponent indicate thermal conditions at the base?

Both roughness parameters show some dependence on flow speed and basal temperature. The decrease in amplitude roughness ν with increasing flow speed (Fig. 6.6 b and d) means either that the ice can flow faster over a smooth bed, or that the bed is smoothed by the erosion from fast ice flow; it is probable that both processes coexist in a positive feedback. The behavior of H with flow speed, at low flow speeds (e.g., $v < 10 - 15 \text{ m a}^{-1}$), can be increasing or decreasing, depending on the predominant basal temperature (Fig. 6.6 a and c). Furthermore, these H - v curves hint at a systematic decrease of H with increasing basal temperature at flow speeds below 15 m a^{-1} .

Figure 6.7 shows the behavior of H with temperature for low ($v < 10 \text{ m a}^{-1}$) and high ($v \geq 100 \text{ m a}^{-1}$) flow speeds. The curve for $v < 10 \text{ m a}^{-1}$ confirms that H decreases with increasing temperature (for $T > -15^\circ\text{C}$). For high flow speeds, H seems to increase with temperature, but variation in H (jumps of up to 0.25 per 0.3°C) is too large for a conclusive statement. Possibly the regions with fast flow are too different, due to preglacial topography and erosion history, to exhibit a common roughness pattern.

Based on the inferred relations, we formulate the following hypothesis: At locations with small flow speeds, a small Hurst exponent hints at a likely temperate bed, a high Hurst exponent at a likely cold bed. This should only be applied to clusters of low or high Hurst exponents and not to single measurements, because H shows relatively large fluctuations. An application of this hypothesis to our data set predicts a temperate bed for the region around Kohnen, parts of the Aurora Subglacial Basin, the South of the OIR survey around Dome Fuji, the location of crossing profiles close to South Pole, and east of Dome C. These results are strengthened by the modeled basal temperatures (Liefvering and Pattyn, 2013) at these locations, which are plotted in Fig. 6.8 a.

This match is not very surprising, as the same temperatures were also the input data to come up with the hypothesis. However, results from the Parallel-Ice-Sheet Model (PISM) (Winkelmann et al., 2011) (model results submitted to the Ice Sheet Model Intercomparison Project (ISMIP6) (see Nowicki et al., 2016, for project description) by Kleiner, T.,

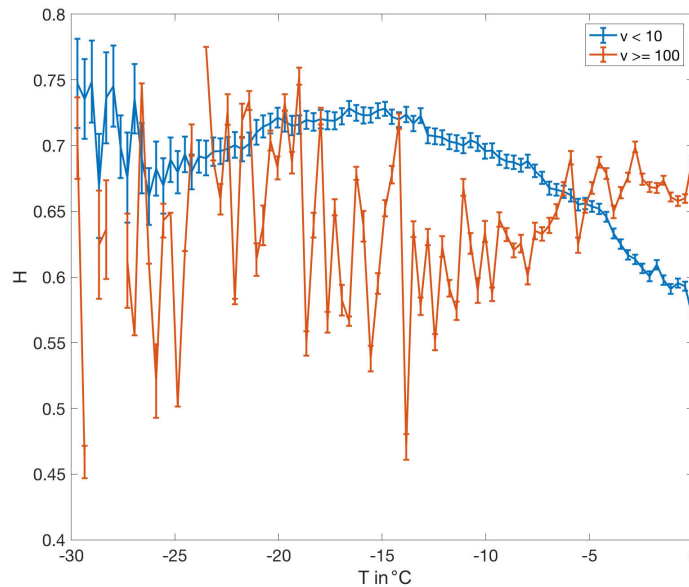


Figure 6.7. Variation of H with basal temperature for small ($v < 10 \text{ m a}^{-1}$) and large ($v \geq 100 \text{ m a}^{-1}$) flow speeds.

Sutter, J. and Humbert, A. in June 2017) show a similar temperature distribution at the hypothesized thaw locations (Fig. 6.8 b). Careful testing of our hypothesis with measured basal temperatures is necessary in a next step. If the hypothesis were to be confirmed by extensive measurements, this method would provide a new independent measure for validating modeled basal thaw/temperate bed. The only obvious location where the modeled basal temperatures contradict our prediction is south-west of Dome C (including little Dome C, Candidate A site). Despite the cluster of low H values modeled temperatures indicate a cold bed with 6°C to 7°C below pmp at this location. On the other hand, there are studies indicating a warm bed and a formerly more dynamic ice sheet with subglacial erosion at Dome C (Siegert et al., 2005; Bingham and Siegert, 2009). And there is also some indication of water in the same region covered by our data at present day. Apart from the many lakes in this region revealed by early surveys (e.g., Oswald and Robin, 1973; Tabacco et al., 2006; Wright and Siegert, 2012), Young et al. (2017) detected 54 lakes in the area covered by exactly the same RES survey that we also use. (Lefebvre et al., 2008, borehole temperatures extrapolated to bed suggest basal melt at DC).

A question that remains open is why we obtain a H - T relation opposite to that derived by Jordan et al. (2017) for north-west Greenland. A good portion of that Greenlandic region has also slow flow speeds below 10 m a^{-1} and the mean and variance of H values is approximately the same as ours. Nevertheless, Jordan et al. (2017) show that H is significantly higher at thawed-bed locations, compared to frozen ones. Possible explanations

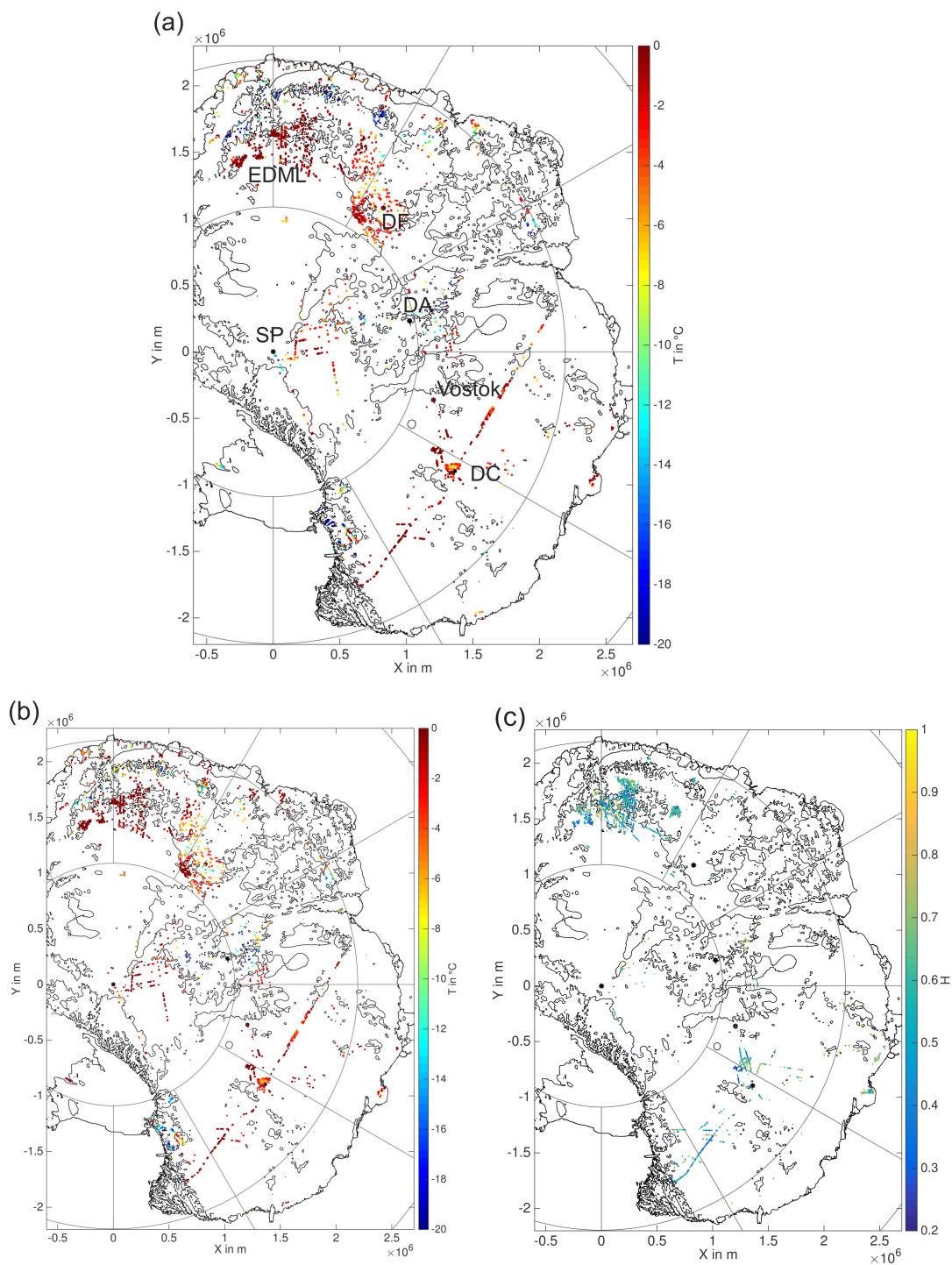


Figure 6.8. The pressure corrected, modeled basal temperatures by (a) (Lieffering and Pattyn, 2013), and (b) with PISM, plotted at locations with small flow speed ($v < 5 \text{ m a}^{-1}$) and small Hurst exponent ($H < 0.4$). (c) shows H at all locations, covered with RES data, where the model by Lieffering and Pattyn (2013) predicts a thawed bed.

can aim for two directions: The differences are induced by the changed parametrizations for roughness-parameter calculations, or actual differences in the glacial or subglacial settings of the investigated regions exist and cause a different scattering behavior. Jordan et al. (2017) use smaller bin widths of 30 m and maximum lags of 150 m (compared to our 100 m bin widths and 1 km maximum lag). We chose the parametrization according to the horizontal sampling of the AWI data, which we cannot increase. Down-sampling tests of AGAP/OIR data show that coarser horizontal sampling leads to a higher H . However, the increase is divergent for the different surveys (OIR: 0.01, AGAP: 0.1-0.2). It still needs to be tested by what exactly these survey-dependent differences are caused and if they are related to the basal thermal state. Moreover, the influence of smaller bin widths and maximum lags (50-450 m), and if any of these aspects could invert the H - T relation need further evaluation. Another explanation could be a specific topographic or glaciological setting of the north-western Greenlandic region, different to that of the bulk of regions covered by our data in East Antarctica. Jordan et al. (2017) propose that the high H at thawed-bed locations in their data could be due to a specific hydrological system, characterized by channels and not having so many deep, large lakes, which leads to more diffuse RES-signal scattering and high H values. The absence of such a channelized drainage system in thawed regions, and a possible replacement with water being collected in large lakes with specular, abrupt reflection signatures, would diminish H . This would also explain why our method is not predicting a temperate bed for parts of regions with modeled thaw in the Aurora Subglacial Basin (Fig. 6.8c compared to Fig. 6.8a). The draining system in this basin was also identified as consisting of channels and fjord-like structures by Young et al. (2011) and Wright et al. (2012). Following this chain of reasoning would imply that any conclusions about basal thermal state stay elusive if the subglacial topography and water-system characteristics are unknown. When comparing the distribution of high and low H values from Jordan et al. (2017) with flow speeds in north-west Greenland, it becomes apparent that H is higher at locations with faster flow. The derived relationship could possibly be rather a relationship between H and flow speed than the stated one between H and thermal state. The influence of flow speed then needs to be decoupled for an investigation of the H -thermal-state relationship.

6.5 Conclusions and outlook

We derived two spatial roughness parameters, the vertical roughness amplitude ν and its horizontal scaling exponent H , for a large compiled RES data set, covering a good part of the EAIS. By combining both roughness parameters, we classified different landscapes by their pre-glacial setting and erosion history.

A comparison of the roughness parameters with flow speed and basal temperatures resulted in some known, respectively more or less intuitive relationships like more erosion

at faster ice flow or faster flow at smoother bed locations. Apart from this, we noticed that H shows a substantially different behavior with flow speed for different basal temperatures. Furthermore, H is smaller at thawed than at frozen bed locations at flow speeds below 10ma^{-1} . This is opposite to the relationship obtained by Jordan et al. (2017) for north-west Greenland, the validity of which we wanted to test also for East Antarctica. The observed relationships lead to the conclusion that in some circumstances the Hurst exponent might indicate the thermal state at the ice-sheet base. We state the hypothesis that at locations with slow ice flow ($v < 5 - 10\text{ma}^{-1}$), clusters of low H (we used $H < 0.4$) indicate a temperate bed. The hypothesis needs careful testing/ground truthing with measurements for verification. If confirmed, this statistical examination of bed elevation would be a simple and fast way of large-scale thermal-state prediction, that is independent of modeling and of radar-wave attenuation in the ice column.

While potentially being of high value, some aspects of this method still need thorough testing before its usage for any basal-state interpretation. One thing is the testing with measured, and not modeled, basal temperatures. But also the influence of altering the parameters of the roughness calculation needs to be further evaluated. First tests of resampling the along-track intervals in the radar data hint at higher values for H with coarser horizontal sampling, however, in a different measure for different surveys. It needs to be examined where the regional or system dependence of the shifting H comes from, and if it goes in the same direction at all length and roughness scales. Furthermore, the effect of different maximum lag sizes and bin widths for the calculations should be evaluated. Additionally to the method testing, a larger-scale roughness analysis of Greenlandic bed topography would be of great interest. This should be relatively expeditious given the huge amount and good spatial coverage of RES data of Greenland (e.g., from the Center for Remote Sensing of Ice Sheets (CReSIS), University of Kansas, Lawrence, USA) and would elucidate if the H -thermal-state relationship observed by Jordan et al. (2017) is caused by a regional setting (e.g. the draining system in this region), or if there are substantial differences between Greenland and East Antarctica in how the basal thermal state influences H . Moreover, as we showed that H varies with basal temperature as well as with flow speed, it would be interesting to remove the influence of flow speed from the investigation of Jordan et al. (2017), and maybe also to compare their results with other thermal-state masks or proxies (like the basal water distribution derived by the same first author, but not yet peer-reviewed: Jordan et al., 2018), because the used mask from MacGregor et al. (2016) itself is strongly dependent on flow speed (Jordan et al., 2018).

7 Conclusions and perspectives

My thesis provides a solid basis for future common analyses of multiple RES data sets, which is a key requirement for the facilitation of continent-wide interpretations of the Antarctic ice sheets' dynamic and climatic history. Comparison of measurements from five different radar systems and synthetically calculated radar traces showed that the most distinct IRHs and IRH patterns are detected by all systems, although in slightly different ways. Differences between the systems are mainly found for the amplitude of the single IRHs as well as the vertical resolution of the internal ice structure, i.e., how many permittivity contrasts are condensed into one reflection in the radar data. Nevertheless, isochronous conductivity IRHs can be transferred between those data that make a good portion of the RES measurements from East Antarctica. Some distinct IRHs could also be matched with conductivity signals in the EDC ice core, which validates their isochronicity and allows for an accurate age assignment. It is feasible to combine the stratigraphic information from multiple RES surveys and thereby enlarge the spatial extent of the mapped age-depth distribution.

Following on from my work, further studies comparing more radar systems are needed. Also, we need to work in other regions within East Antarctica, where RES stratigraphy characteristics are different to the Dome C region. For example, regions with a disrupted stratigraphy or with a very rough bed topography would make interesting test sites. Furthermore, reflection amplitudes and their dependence on measuring frequencies need to be included in future comparison studies, to enable extended interpretation of ice properties, e.g., attenuation rates and temperature distribution in the ice.

My work on the combination of the IRH information from several RES data sets has facilitated large-scale mapping of the age-depth stratigraphy across the EAIS. First order estimates about spatial accumulation-rate distribution, maximum age of the deep ice, and regions of changing flow regime can be obtained from the established stratigraphy. However, such estimates are of qualitative nature, but can support the reconstruction of the 'big picture' of the ice sheet. Our tests of quantitatively deducing paleo accumulation and its temporal variation over climate cycles from the RES isochrones revealed that more

effort needs to be made to integrate RES stratigraphy into ice-flow models to obtain specific, quantitative statements about past accumulation rates on large spatial and temporal scales. Accumulation rate calculation with the tested simple method is limited to regions with negligible horizontal ice flow, like ice divides and domes. In regions with faster ice flow, the (possibly even temporally changing) horizontal flow path of the ice since its deposition as well as the temporal variation of accumulation rates have to be taken into account. Neglecting any of these processes generates unrealistic temporal development of accumulation rates, as the errors increase with older isochrones and accordingly longer flow paths.

There is still a lot of work to be done to achieve a continent-wide interpretation of age-depth stratigraphy to inform paleo-climate reconstruction and ice-sheet models. Additional studies incorporating further RES data have to be carried out to increase the spatial coverage and temporal resolution of the age-depth stratigraphy, especially the latter is fairly sparse in our study. In future studies, accumulation rates and variations in ice-flow dynamics could perhaps be derived from inversions for the internal RES stratigraphy in ice-flow models with age tracers of paleo surfaces, as has already been performed for very localized areas. These models could use the dated RES isochrones to assimilate the depth distribution of the age tracers of the respective paleo surfaces. However, such continental-scale models are only just able to perform forward calculations for time scales of several 100 ka, which takes several weeks of computation time. The required computation time for the inversion process in a continental-scale model will be many times higher.

Interpreting the bedrock topography beneath the EAIS has provided a lot of valuable information about the evolution and geologic condition of different subglacial landscapes. Statistical two-parameter roughness analysis, with one parameter characterizing the amplitude, the other the wavelength of bed topography, is a convenient method to disclose extensive, glacially preserved mountain ranges, basins with thick sediment cover, and the extent of glacial erosion. Beside facilitating geomorphological interpretation, basal roughness acts as a key control on, and is at the same time affected by, ice flow in a positive feedback mechanism. Moreover, a relationship between the wavelength roughness parameter and basal temperatures can be observed. The significant change of the roughness parameter with temperature leads to the hypothesis that basal roughness can, under some circumstances, be used to predict the thermal conditions at the base of the ice sheet. It is important to first separate the influence of ice flow on the roughness parameter, which we accomplished by considering only regions of slow ice flow. In that case, small values of the roughness parameter are located, where models predict a temperate bed. These observations are incentive to further evaluate this potential method of thaw prediction. If confirmed, this would be a useful way to validate modeled temperatures, as it is completely independent of modeling and all needed information is readily accessible.

The basal roughness parameters we derived for the EAIS could be further used, together with information (from a hydrological model) on the occurrence of water at the bed, to parameterize the basal sliding in ice-sheet models. The hypothesis of basal roughness being indicative of the thermal state of basal ice is only in the early stages of development and needs thorough testing in additional studies. The influence of RES data characteristics, for instance the horizontal sampling interval, and altering parameters for roughness calculation need further assessment. Moreover, the results should be compared to measured basal temperatures or to other measurable proxies for basal thaw. By such a comparison, we can confirm that the behavior of the wavelength roughness parameter is related to the thermal state, and not linked to another factor, affecting both, roughness parameter and modeled temperatures.

The combination of the outcomes of Paper II and Paper III, i.e., the internal stratigraphy and basal condition, offers great potential for further evaluation of ice-sheet dynamics. For example, the bedrock properties and basal temperatures can be investigated at locations with a disrupted or buckled stratigraphy. This helps to clarify if changing flow behavior is induced by a changing bed roughness or if it is due to different inherent properties of the ice, like temperature, grain sizes, impurities, or crystal-orientation fabric.

References

- Aitken, A., Roberts, J., Van Ommen, T., Young, D., Golledge, N., Greenbaum, J., Blankenship, D., and Siegert, M.: Repeated large-scale retreat and advance of Totten Glacier indicated by inland bed erosion, *Nature*, 533, 385, doi:10.1038/nature17447, 2016. 5
- Antarctica's Gamburtsev Province Project - North: Radio Echo Sounding ice thickness data, Available at: <https://legacy.bas.ac.uk/data/aerogeo/access/agap/> (Accessed: 20 Aug 2017), 2008/09. 74
- Antarctica's Gamburtsev Province Project - South: Radar Depth Sounder Data, Level 1, 1D Migrated SAR, Available at: http://pods.ldeo.columbia.edu:1986/legacyData/AGAP/DataLevel_1/RADAR/ (Accessed: 4 Dec 2017), 2008/09. 54, 74, 119
- Aschwanden, A., Bueler, E., Khroulev, C., and Blatter, H.: An enthalpy formulation for glaciers and ice sheets, *Journal of Glaciology*, 58, 441–457, doi:10.3189/2012JoG11J088, 2012. 56
- Bazin, L., Landais, A., Lemieux-Dudon, B., Toyé Mahamadou Kele, H., Veres, D., Parrenin, F., Martinerie, P., Ritz, C., Capron, E., Lipenkov, V., et al.: An optimized multi-proxy, multi-site Antarctic ice and gas orbital chronology (AICC2012): 120-800 ka, *Climate of the Past*, 9, 1715–1731, doi:10.5194/cp-9-1715-2013, 2013. 28, 39, 40, 46, 55, 58, 66
- Beckmann, A. and Goosse, H.: A parameterization of ice shelf-ocean interaction for climate models, *Ocean Modelling*, 5, 157 – 170, doi:10.1016/S1463-5003(02)00019-7, 2003. 56
- Bell, R. E., Ferraccioli, F., Creyts, T. T., Braaten, D., Corr, H., Das, I., Damaske, D., Frearson, N., Jordan, T., Rose, K., Studinger, M., and Wolovick, M.: Widespread persistent thickening of the East Antarctic Ice Sheet by freezing from the base, *Science*, 331, 1592–1595, doi:10.1126/science.1200109, 2011. 4, 54, 74
- Bell, R. E., Tinto, K., Das, I., Wolovick, M., Chu, W., Creyts, T. T., Frearson, N., Abdi, A., and Paden, J. D.: Deformation, warming and softening of Greenland's ice by refreezing meltwater, *Nature Geoscience*, 7, 497, doi:10.1038/ngeo2179, 2014. 4, 52
- Bellot, F.-F.: Estimates of the basal roughness of the Antarctic ice sheet in Dronning Maud Land and its implication, Master's thesis, Eberswalde University for Sustainable Development, 2012. 16, 74
- Bingham, R. G. and Siegert, M. J.: Radio-echo sounding over polar ice masses, *Journal of Environmental & Engineering Geophysics*, 12, 47–62, 2007. 9
- Bingham, R. G. and Siegert, M. J.: Quantifying subglacial bed roughness in Antarctica: implications for ice-sheet dynamics and history, *Quaternary Science Reviews*, 28, 223–236, doi:10.1016/j.quascirev.2008.10.014, 2009. 4, 85
- Bingham, R. G., Siegert, M. J., Young, D. A., and Blankenship, D. D.: Organized flow from the South Pole to the Filchner-Ronne ice shelf: An assessment of balance velocities in interior East Antarctica using radio echo sounding data, *Journal of Geophysical Research: Earth Surface*, 112, doi:10.1029/2006JF000556, 2007. 65

- Bingham, R. G., MacGregor, J. A., and Ross, N.: AntArchitecture: Towards the continent-wide integration of radar-sounded internal surfaces to reconstruct Antarctica's climate history, in: AGU Fall Meeting, San Francisco, California, USA, 2016. 7
- Blankenship, D. D., Kempf, S. D., Young, D. A., Richter, T. G., Schroeder, D. M., Greenbaum, J. S., Holt, J. W., van Ommen, T., Warner, R. C., Roberts, J. L., Young, N. W., Lemeur, E., and Siegert, M. J.: IceBridge HiCARS 2 L2 Geolocated Ice Thickness, Version 1, Boulder, Colorado USA. NASA National Snow and Ice Data Center Distributed Active Archive Center, (Accessed: 22 Nov 2017), doi:10.5067/f5fgut9f5089, 2011, updated 2017. 74
- Bo, S., Siegert, M. J., Mudd, S. M., Sugden, D., Fujita, S., Xiangbin, C., Yunyun, J., Xueyuan, T., and Yuansheng, L.: The Gamburtsev mountains and the origin and early evolution of the Antarctic Ice Sheet, *Nature*, 459, 4, doi:10.1038/nature08024, 2009. 54
- Bogorodsky, V., Bentley, C., and Gudmandsen, P.: *Radioglaciology*, Springer, doi:10.1007/978-94-009-5275-1, 1985. 9, 12
- Bohleber, P., Wagner, N., and Eisen, O.: Permittivity of ice at radio frequencies: Part II. Artificial and natural polycrystalline ice, *Cold Regions Science and Technology*, 83, 13–19, doi:10.1016/j.coldregions.2012.05.010, 2012. 31
- Bons, P. D., Jansen, D., Mundel, F., Bauer, C. C., Binder, T., Eisen, O., Jessell, M. W., Llorens, M.-G., Steinbach, F., Steinhage, D., and Weikusat, I.: Converging flow and anisotropy cause large-scale folding in Greenland's ice sheet, *Nature communications*, 7, 11 427, doi:10.1038/ncomms11427, 2016. 4
- Brook, E. J., Wolff, E., Dahl-Jensen, D., Fischer, H., Steig, E. J., et al.: The future of ice coring: international partnerships in ice core sciences (IPICS), *PAGES news*, 14, 6–10, 2006. 3, 6, 26
- Bueler, E. and Brown, J.: Shallow shelf approximation as a "sliding law" in a thermomechanically coupled ice sheet model, *Journal of Geophysical Research: Earth Surface*, 114, F03 008, doi:10.1029/2008JF001179, 2009. 56
- Cavitte, M. G., Blankenship, D. D., Young, D. A., Schroeder, D. M., Parrenin, F., Lemeur, E., Macgregor, J. A., and Siegert, M. J.: Deep radiostratigraphy of the East Antarctic plateau: connecting the Dome C and Vostok ice core sites, *Journal of Glaciology*, pp. 1–12, doi:10.1017/jog.2016.11, 2016. 4, 5, 27, 33, 41, 46, 52, 64, 74
- Cavitte, M. G. P., Parrenin, F., Ritz, C., Young, D. A., Blankenship, D. D., Frezzotti, M., and Roberts, J. L.: Stable accumulation patterns around Dome C, East Antarctica, over the last glacial cycle, *The Cryosphere Discuss.*, doi:10.5194/tc-2017-71, 2017. 67
- Christianson, K., Peters, L. E., Alley, R. B., Anandkrishnan, S., Jacobel, R. W., Riverman, K. L., Muto, A., and Keisling, B. A.: Dilatant till facilitates ice-stream flow in northeast Greenland, *Earth and Planetary Science Letters*, 401, 57–69, doi:10.1016/j.epsl.2014.05.060, 2014. 4
- Clark, P. U. and Pollard, D.: Origin of the middle Pleistocene transition by ice sheet erosion of regolith, *Paleoceanography*, 13, 1–9, doi:10.1029/97PA02660, 1998. 2

-
- Clark, P. U., Archer, D., Pollard, D., Blum, J. D., Rial, J. A., Brovkin, V., Mix, A. C., Pisias, N. G., and Roy, M.: The middle Pleistocene transition: characteristics, mechanisms, and implications for long-term changes in atmospheric pCO₂, *Quaternary Science Reviews*, 25, 3150–3184, doi:10.1016/j.quascirev.2006.07.008, 2006. 2
- Clarke, T. S., Liu, C., Lord, N. E., and Bentley, C. R.: Evidence for a recently abandoned shear margin adjacent to ice stream B2, Antarctica, from ice-penetrating radar measurements, *Journal of Geophysical Research: Solid Earth*, 105, 13 409–13 422, doi:10.1029/2000JB900037, 2000. 4
- Conway, H., Catania, G., Raymond, C., Gades, A., Scambos, T., and Engelhardt, H.: Switch of flow direction in an Antarctic ice stream, *Nature*, 419, 465, doi:10.1038/nature01081, 2002. 4
- Cook, C. P., Van De Flieddt, T., Williams, T., Hemming, S. R., Iwai, M., Kobayashi, M., Jimenez-Espejo, F. J., Escutia, C., González, J. J., Khim, B.-K., et al.: Dynamic behaviour of the East Antarctic ice sheet during Pliocene warmth, *Nature Geoscience*, 6, 765, doi:10.1038/ngeo1889, 2013. 5
- Courant, R., Friedrichs, K., and Lewy, H.: Über die partiellen Differenzgleichungen der mathematischen Physik, *Mathematische Annalen*, 100, 32–74, doi:10.1007/BF01448839, 1928. 30
- Coxall, H. K., Wilson, P. A., Pälike, H., Lear, C. H., and Backman, J.: Rapid stepwise onset of Antarctic glaciation and deeper calcite compensation in the Pacific Ocean, *Nature*, 433, 53, doi:10.1038/nature03135, 2005. 6
- CRISIS: Radar depth sounder readme, ftp://data.cresis.ku.edu/data/rds/rds_readme.pdf, (Accessed: 15 Mar 2016), 2016. 32, 33
- Creyts, T. T., Ferraccioli, F., Bell, R. E., Wolovick, M., Corr, H., Rose, K. C., Frearson, N., Damaske, D., Jordan, T., Braaten, D., et al.: Freezing of ridges and water networks preserves the Gamburtsev Subglacial Mountains for millions of years, *Geophysical Research Letters*, 41, 8114–8122, doi:10.1002/2014GL061491, 2014. 54, 74, 82
- Cuffey, K. M. and Paterson, W. S. B.: *The physics of glaciers*, Academic Press, 2010. 1, 2, 12
- Dansgaard, W., Johnsen, S., Clausen, H., Dahl-Jensen, D., Gundestrup, N., Hammer, C., Hvidberg, C., Steffensen, J., Sveinbjörnsdóttir, A., Jouzel, J., et al.: Evidence for general instability of past climate from a 250-kyr ice-core record, *Nature*, 364, 218, doi:10.1038/364218a0, 1993. 2
- Das, I., Bell, R. E., Scambos, T. A., Wolovick, M., Creyts, T. T., Studinger, M., Frearson, N., Nicolas, J. P., Lenaerts, J. T., and Van Den Broeke, M. R.: Influence of persistent wind scour on the surface mass balance of Antarctica, *Nature Geoscience*, 6, 367–371, doi:10.1038/ngeo1766, 2013. 3, 4, 64
- DeConto, R. M. and Pollard, D.: Rapid Cenozoic glaciation of Antarctica induced by declining atmospheric CO₂, *Nature*, 421, 245–249, doi:10.1038/nature01290, 2003. 54
- DeConto, R. M. and Pollard, D.: Contribution of Antarctica to past and future sea-level rise, *Nature*, 531, 591, doi:10.1038/nature17145, 2016. 5

- Diez, A., Eisen, O., Hofstede, C., Lambrecht, A., Mayer, C., Miller, H., Steinhage, D., Binder, T., and Weikusat, I.: Seismic wave propagation in anisotropic ice—Part 2: Effects of crystal anisotropy in geophysical data, *The Cryosphere*, 9, 385–398, doi:10.5194/tc-9-385-2015, 2015. 12
- Diez, A., Matsuoka, K., Ferraccioli, F., Jordan, T. A., Corr, H. F., Kohler, J., V., O. A., and Forsberg, R.: Basal settings control fast ice flow in the Recovery/Slessor/Bailey Region, East Antarctica, *Geophysical Research Letters*, doi:10.1002/2017GL076601, 2018. 4, 84
- Dowdeswell, J. A. and Evans, S.: Investigations of the form and flow of ice sheets and glaciers using radio-echo sounding, *Reports on Progress in Physics*, 67, 1821, doi:10.1088/0034-4885/67/10/R03, 2004. 9, 11, 12, 13, 26
- Drews, R., Eisen, O., Weikusat, I., Kipfstuhl, S., Lambrecht, A., Steinhage, D., Wilhelms, F., and Miller, H.: Layer disturbances and the radio-echo free zone in ice sheets, *The Cryosphere*, 3, 195–203, doi:10.5194/tc-3-195-2009, 2009. 44, 52
- Drews, R., Martin, C., Steinhage, D., and Eisen, O.: Characterizing the glaciological conditions at Halvfarryggen ice dome, Dronning Maud Land, Antarctica, *Journal of Glaciology*, 59, 9–20, doi:10.3189/2013JoG12J134, 2013. 4, 111
- Eisen, O., Nixdorf, U., Wilhelms, F., and Miller, H.: Age estimates of isochronous reflection horizons by combining ice core, survey, and synthetic radar data, *Journal of Geophysical Research: Solid Earth*, 109, 1978–2012, doi:10.1029/2003JB002858, 2004. 27, 30
- Eisen, O., Wilhelms, F., Steinhage, D., and Schwander, J.: Improved method to determine radio-echo sounding reflector depths from ice-core profiles of permittivity and conductivity, *Journal of Glaciology*, 52, 299–310, doi:10.3189/172756506781828674, 2006. 27, 28, 29, 30, 33, 39, 55
- Eisen, O., Hamann, I., Kipfstuhl, S., Steinhage, D., and Wilhelms, F.: Direct evidence for continuous radar reflector originating from changes in crystal-orientation fabric, *The Cryosphere*, 1, 1–10, doi:10.5194/tc-1-1-2007, 2007. 12, 43
- Elderfield, H., Ferretti, P., Greaves, M., Crowhurst, S., McCave, I., Hodell, D., and Piotrowski, A.: Evolution of ocean temperature and ice volume through the mid-Pleistocene climate transition, *Science*, 337, 704–709, doi:10.1126/science.1221294, 2012. 2
- EPICA community members: Eight glacial cycles from an Antarctic ice core, *Nature*, 429, 623–628, doi:10.1038/nature02599, 2004. 3, 26, 28
- Evans, S. and Smith, B.: Radio echo exploration of the Antarctic ice sheet, 1969–70, *Polar Record*, 15, 336–338, doi:10.1017/S0032247400061143, 1970. 4
- Evans, S., Drewry, D., and Robin, G. d. Q.: Radio-echo sounding in Antarctica, 1971–72, *Polar Record*, 16, 207–212, doi:10.1017/S003224740006280X, 1972. 4
- Fahnestock, M., Abdalati, W., Joughin, I., Brozena, J., and Gogineni, P.: High geothermal heat flow, basal melt, and the origin of rapid ice flow in central Greenland, *Science*, 294, 2338–2342, doi:10.1126/science.1065370, 2001. 52

-
- Ferraccioli, F., Finn, C. A., Jordan, T. A., Bell, R. E., Anderson, L. M., and Damaske, D.: East Antarctic rifting triggers uplift of the Gamburtsev Mountains, *Nature*, 479, 388–392, doi:10.1038/nature10566, 2011. 74
- Fischer, H., Severinghaus, J., Brook, E., Wolff, E., Albert, M., Alemany, O., Arthern, R., Bentley, C., Blankenship, D., Chappellaz, J., et al.: Where to find 1.5 million year old ice for the IPICS “Oldest Ice” ice core, *Climate of the Past*, 9, 2489–2505, doi:10.5194/cp-9-2489-2013, 2013. 6, 26, 52
- Fisher, D. A., Reeh, N., and Clausen, H.: Stratigraphic noise in time series derived from ice cores, *Ann. Glaciol*, 7, 76–83, 1985. 44
- Fretwell, P., Pritchard, H. D., Vaughan, D. G., Bamber, J., Barrand, N., Bell, R., Bianchi, C., Bingham, R., Blankenship, D., Casassa, G., et al.: Bedmap2: improved ice bed, surface and thickness datasets for Antarctica, *The Cryosphere*, 7, doi:10.5194/tcd-6-4305-2012, 2013. 56, 73
- Frezzotti, M., Pourchet, M., Flora, O., Gandolfi, S., Gay, M., Urbini, S., Vincent, C., Becagli, S., Gagnani, R., Proposito, M., et al.: Spatial and temporal variability of snow accumulation in East Antarctica from traverse data, *Journal of Glaciology*, 51, 113–124, doi:10.3189/172756505781829502, 2005. 42, 44, 64
- Fujita, S. and Mae, S.: Causes and nature of ice-sheet radio-echo internal reflections estimated from the dielectric properties of ice, *Annals of Glaciology*, 20, 80–86, 1994. 12, 29, 43
- Fujita, S., Mae, S., and Matsuoka, T.: Dielectric anisotropy in ice Ih at 9.7 GHz, *Annals of Glaciology*, 17, 276–280, doi:10.3189/S0260305500012969, 1993. 10, 12
- Fujita, S., Maeno, H., Uratsuka, S., Furukawa, T., Mae, S., Fujii, Y., and Watanabe, O.: Nature of radio echo layering in the Antarctic ice sheet detected by a two-frequency experiment, *Journal of Geophysical Research*, 104, 13 013–13 024, 1999. 27, 44
- Fujita, S., Matsuoka, T., Ishida, T., Matsuoka, K., and Mae, S.: *The Physics of Ice Core Records*. Chap. A summary of the complex dielectric permittivity of ice in the megahertz range and its application for radar sounding of polar ice sheets, Hokkaido University Press, Sapporo, Japan, 185–212, 2000. 27, 46, 55
- Fujita, S., Holmlund, P., Matsuoka, K., Enomoto, H., Fukui, K., Nakazawa, F., Sugiyama, S., and Surdyk, S.: Radar diagnosis of the subglacial conditions in Dronning Maud Land, East Antarctica, *The Cryosphere*, 6, 1203–1219, doi:10.5194/tc-6-1203-2012, 2012. 52
- Gautier, E., Savarino, J., Erbland, J., Lanciki, A., and Possenti, P.: Variability of sulfate signal in ice core records based on five replicate cores, *Climate of the Past*, 12, 103–113, doi:10.5194/cp-12-103-2016, 2016. 45
- Gogineni, P.: CReSIS radar depth sounder data, Center for Remote Sensing of Ice Sheets, Lawrence, KS <https://data.cresis.-ku.edu>, 2012. 32

- Gogineni, S., Chuah, T., Allen, C., Jkzek, K., and Moore, R. K.: Instruments and Methods: An improved coherent radar depth sounder, *Journal of Glaciology*, 44, 659–669, doi:10.3198/1998JoG44-148-643-652, 1998. 52
- Golledge, N. R., Kowalewski, D. E., Naish, T. R., Levy, R. H., Fogwill, C. J., and Gasson, E. G.: The multi-millennial Antarctic commitment to future sea-level rise, *Nature*, 526, 421, doi:10.1038/nature15706, 2015. 5
- Gough, S.: A low temperature dielectric cell and the permittivity of hexagonal ice to 2 K, *Canadian Journal of Chemistry*, 50, 3046–3051, doi:10.1139/v72-483, 1972. 46
- Greve, R. and Blatter, H.: *Dynamics of ice sheets and glaciers*, Springer Science & Business Media, 2009. 56
- Gudlaugsson, E., Humbert, A., Winsborrow, M., and Andreassen, K.: Subglacial roughness of the former Barents Sea ice sheet, *Journal of Geophysical Research: Earth Surface*, 118, 2546–2556, doi:10.1002/2013JF002714, 2013. 72
- Gudmandsen, P.: Notes on radar sounding of the Greenland ice sheet, in: *Proc. of the International Meeting on Radar Glaciology*, vol. 124, p. 127, 1970. 4
- Gudmandsen, P.: Layer echoes in polar ice sheets, *Journal of Glaciology*, 15, 95–101, doi:10.3189/S0022143000034304, 1975. 4
- Gulick, S. P., Shevenell, A. E., Montelli, A., Fernandez, R., Smith, C., Warny, S., Bohaty, S. M., Sjunneskog, C., Leventer, A., Frederick, B., et al.: Initiation and long-term instability of the East Antarctic Ice Sheet, *Nature*, 552, 225, doi:10.1038/nature25026, 2017. 5
- Hammer, C. U., Clausen, H. B., and Dansgaard, W.: Greenland ice sheet evidence of post-glacial volcanism and its climatic impact, *Nature*, 288, 230, doi:10.1038/288230a0, 1980. 12
- Harrison, C.: Radio echo sounding of horizontal layers in ice, *Journal of glaciology*, 12, 383–397, doi:10.3189/S0022143000031804, 1973. 4, 12
- Hawley, R. L., Courville, Z. R., Kehrl, L. M., Lutz, E. R., Osterberg, E. C., Overly, T. B., and Wong, G. J.: Recent accumulation variability in northwest Greenland from ground-penetrating radar and shallow cores along the Greenland Inland Traverse, *Journal of Glaciology*, 60, 375–382, doi:10.3189/2014JoG13J141, 2014. 52
- Hays, J. D., Imbrie, J., and Shackleton, N. J.: Variations in the Earth's orbit: pacemaker of the ice ages, *Science*, 194, 1121–1132, 1976. 2
- Heinrich, H.: Origin and consequences of cyclic ice rafting in the northeast Atlantic Ocean during the past 130,000 years, *Quaternary research*, 29, 142–152, doi:10.1016/0033-5894(88)90057-9, 1988. 2
- Hélière, F., Lin, C.-C., Corr, H., and Vaughan, D.: Radio echo sounding of Pine Island Glacier, West Antarctica: Aperture synthesis processing and analysis of feasibility from space, *IEEE Transactions on Geoscience and Remote Sensing*, 45, 2573–2582, doi:10.1109/TGRS.2007.897433, 2007. 74

-
- Helm, V., Humbert, A., and Miller, H.: Elevation and elevation change of Greenland and Antarctica derived from CryoSat-2, *The Cryosphere*, 8, 1539–1559, doi:10.5194/tc-8-1539-2014, 2014. 5
- Herron, M. M. and Langway, J.: Firm densification: an empirical model, *Journal of Glaciology*, 25, 373–385, 1980. 12
- Hilbert, D.: Grundzüge einer allgemeinen Theorie der linearen Integralgleichungen. Vierte Mitteilung, *Nachrichten von der Gesellschaft der Wissenschaften zu Göttingen, Mathematisch-Physikalische Klasse*, 1906, 157–228, 1906. 30
- Hindmarsh, R. C., Leysinger Vieli, G. J., Raymond, M. J., and Gudmundsson, G. H.: Draping or overriding: the effect of horizontal stress gradients on internal layer architecture in ice sheets, *Journal of geophysical research: earth surface*, 111, doi:10.1029/2005JF000309, 2006. 12
- Hindmarsh, R. C., Leysinger Vieli, G. J., and Parrenin, F.: A large-scale numerical model for computing isochrone geometry, *Annals of Glaciology*, 50, 130–140, doi:10.3189/172756409789097450, 2009. 51
- Holschuh, N., Christianson, K., and Anandakrishnan, S.: Power loss in dipping internal reflectors, imaged using ice-penetrating radar, *Annals of Glaciology*, 55, 49–56, doi:10.3189/2014AoG67A005, 2014. 4, 64
- Hörhold, M., Kipfstuhl, S., Wilhelms, F., Freitag, J., and Frenzel, A.: The densification of layered polar firn, *Journal of Geophysical Research: Earth Surface*, 116, 2003–2012, doi:10.1029/2009JF001630, 2011. 12, 28, 46
- Huybrechts, P., Steinhage, D., Wilhelms, F., and Bamber, J.: Balance velocities and measured properties of the Antarctic ice sheet from a new compilation of gridded data for modelling, *Annals of Glaciology*, 30, 52–60, doi:10.3189/172756400781820778, 2000. 1
- Huybrechts, P., Rybak, O., Steinhage, D., and Pattyn, F.: Past and present accumulation rate reconstruction along the Dome Fuji–Kohnen radio-echo sounding profile, Dronning Maud Land, East Antarctica, *Annals of glaciology*, 50, 112–120, doi:10.3189/172756409789097513, 2009. 55, 66, 67
- Intergovernmental Panel on Climate Change (IPCC): Synthesis Report, in: *Climate Change 2014: Contribution of Working Groups I, II and III to the Fifth Assessment Report of the Intergovernmental Panel on Climate Change*, edited by The Core Writing Team, R. P. and Meyer, L., p. 151 ff, IPCC, Geneva, Switzerland, 2014. 1
- Jacobel, R., Scambos, T., Nereson, N., and Raymond, C.: Changes in the margin of Ice Stream C, Antarctica, *Journal of Glaciology*, 46, 102–110, doi:10.3189/172756500781833485, 2000. 4
- Jacobel, R. W. and Hodge, S. M.: Radar internal layers from the Greenland summit, *Geophysical Research Letters*, 22, 587–590, doi:10.1029/95GL00110, 1995. 4

- Jacobel, R. W., Scambos, T. A., Raymond, C. F., and Gades, A. M.: Changes in the configuration of ice stream flow from the West Antarctic Ice Sheet, *Journal of Geophysical Research: Solid Earth*, 101, 5499–5504, doi:10.1029/95JB03735, 1996. 4
- Jamieson, S. S., Sugden, D. E., and Hulton, N. R.: The evolution of the subglacial landscape of Antarctica, *Earth and Planetary Science Letters*, 293, 1–27, doi:10.1016/j.epsl.2010.02.012, 2010. 82
- Jamieson, S. S., Stokes, C. R., Ross, N., Rippin, D. M., Bingham, R. G., Wilson, D. S., Margold, M., and Bentley, M. J.: The glacial geomorphology of the Antarctic ice sheet bed, *Antarctic Science*, 26, 724–741, doi:10.1017/S0954102014000212, 2014. 7
- Johari, G. P. and Jones, S.: Dielectric properties of polycrystalline D₂O ice Ih (hexagonal), in: *Proc. R. Soc. Lond. A*, vol. 349, pp. 467–495, The Royal Society, 1976. 10, 15
- Jordan, T., Ferraccioli, F., Corr, H., Graham, A., Armadillo, E., and Bozzo, E.: Hypothesis for mega-outburst flooding from a palaeo-subglacial lake beneath the East Antarctic Ice Sheet, *Terra Nova*, 22, 283–289, doi:10.1111/j.1365-3121.2010.00944.x, 2010. 84
- Jordan, T., Bamber, J., Williams, C., Paden, J., Siegert, M., Huybrechts, P., Gagliardini, O., and Gillet-Chaulet, F.: An ice-sheet wide framework for englacial attenuation and basal reflection from ice penetrating radar data, *The Cryosphere*, 10, 1547–1570, doi:10.5194/tc-10-1547-2016, 2016. 27
- Jordan, T. M., Cooper, M. A., Schroeder, D. M., Williams, C. N., Paden, J. D., Siegert, M. J., and Bamber, J. L.: Self-affine subglacial roughness: consequences for radar scattering and basal water discrimination in northern Greenland, *The Cryosphere*, 11, 1247, doi:10.5194/tc-11-1247-2017, 2017. 4, 24, 72, 79, 80, 82, 85, 87, 88
- Jordan, T. M., Williams, C. N., Schroeder, D. M., Martos, Y. M., Cooper, M. A., Siegert, M. J., Paden, J. D., Huybrechts, P., and Bamber, J. L.: A constraint upon the basal water distribution and basal thermal state of the Greenland Ice Sheet from radar bed-echoes, *The Cryosphere Discuss.*, in review, doi:10.5194/tc-2018-53, 2018. 88
- Joughin, I., Smith, B. E., and Medley, B.: Marine ice sheet collapse potentially under way for the Thwaites Glacier Basin, West Antarctica, *Science*, 344, 735–738, doi:10.1126/science.1249055, 2014. 5
- Kamb, B.: Sliding motion of glaciers: theory and observation, *Reviews of Geophysics*, 8, 673–728, doi:10.1029/RG008i004p00673, 1970. 72
- Karlsson, N. B., Rippin, D. M., Bingham, R. G., and Vaughan, D. G.: A ‘continuity-index’ for assessing ice-sheet dynamics from radar-sounded internal layers, *Earth and Planetary Science Letters*, 335, 88–94, doi:10.1016/j.epsl.2012.04.034, 2012. 4, 27, 52, 65
- Karlsson, N. B., Eisen, O., Dahl-Jensen, D., Freitag, J., Kipfstuhl, S., Lewis, C., Nielsen, L. T., Paden, J. D., Winter, A., and Wilhelms, F.: Accumulation Rates during 1311–2011 CE in North-Central Greenland Derived from Air-Borne Radar Data, *Frontiers in Earth Science*, 4, 97, doi:10.3389/feart.2016.00097, 2016. 21, 34, 52

- Kawamura, K., Parrenin, F., Lisiecki, L., Uemura, R., Vimeux, F., Severinghaus, J. P., Hutterli, M. A., Nakazawa, T., Aoki, S., Jouzel, J., et al.: Northern Hemisphere forcing of climatic cycles in Antarctica over the past 360,000 years, *Nature*, 448, 912–916, doi:10.1038/nature06015, <http://www.nature.com/nature/journal/v448/n7156/suppinfo/nature06015.html>, 2007. 55
- Kennett, J. P.: Cenozoic evolution of Antarctic glaciation, the circum-Antarctic Ocean, and their impact on global paleoceanography, *Journal of geophysical research*, 82, 3843–3860, doi:10.1029/JC082i027p03843, 1977. 6
- Kipfstuhl, S., Pauer, F., Kuhs, W. F., and Shoji, H.: Air bubbles and clathrate hydrates in the transition zone of the NGRIP deep ice core, *Geophysical Research Letters*, 28, 591–594, doi:10.1029/1999GL006094, 2001. 3
- Konrad, H., Shepherd, A., Gilbert, L., Hogg, A. E., McMillan, M., Muir, A., and Slater, T.: Net retreat of Antarctic glacier grounding lines, *Nature Geoscience*, p. 1, doi:10.1038/s41561-018-0082-z, 2018. 5
- Kovacs, A., Gow, A. J., and Morey, R. M.: The in-situ dielectric constant of polar firn revisited, *Cold Regions Science and Technology*, 23, 245–256, doi:10.1016/0165-232X(94)00016-Q, 1995. 10
- Le Meur, E., Magand, O., Laurent, A., Fily, M., Frezzotti, M., Cavitte, M., Mulvaney, R., and Urbini, S.: Spatial and temporal distributions of surface mass balance between Concordia and Vostok stations, Antarctica, from combined radar and ice core data: first results and detailed error analysis, *The Cryosphere*, 12, 1831, doi:10.5194/tc-12-1831-2018, 2018. 67
- Lear, C., Elderfield, H., and Wilson, P.: Cenozoic deep-sea temperatures and global ice volumes from Mg/Ca in benthic foraminiferal calcite, *Science*, 287, 269–272, doi:10.1126/science.287.5451.269, 2000. 6
- Lefebvre, E., Ritz, C., Legrésy, B., and Possenti, P.: New temperature profile measurement in the EPICA Dome C borehole, *Geophysical Research Abstracts*, EGU General Assembly, pp. 13–18, 2008. 85
- Lenton, T. M., Held, H., Kriegler, E., Hall, J. W., Lucht, W., Rahmstorf, S., and Schellnhuber, H. J.: Tipping elements in the Earth's climate system, *Proceedings of the National Academy of Science*, 105, 1786–1793, doi:10.1073/pnas.0705414105, 2008. 1
- Leysinger Vieli, G. J., Hindmarsh, R. C., Siegert, M. J., and Bo, S.: Time-dependence of the spatial pattern of accumulation rate in East Antarctica deduced from isochronic radar layers using a 3-D numerical ice flow model, *Journal of Geophysical Research: Earth Surface*, 116, doi:10.1029/2010JF001785, 2011. 51, 64, 65, 68
- Li, X., Sun, B., Siegert, M. J., Bingham, R. G., Tang, X., Zhang, D., Cui, X., and Zhang, X.: Characterization of subglacial landscapes by a two-parameter roughness index, *Journal of Glaciology*, 56, 831–836, doi:10.3189/002214310794457326, 2010. 4, 72, 76, 78, 79, 82, 83

- Liefferinge, B. V. and Pattyn, F.: Using ice-flow models to evaluate potential sites of million year-old ice in Antarctica, *Climate of the Past*, 9, 2335–2345, doi:10.5194/cp-9-2335-2013, 2013. 77, 80, 84, 86
- Lisiecki, L. E. and Raymo, M. E.: A Pliocene-Pleistocene stack of 57 globally distributed benthic $\delta^{18}\text{O}$ records, *Paleoceanography*, 20, doi:10.1029/2004PA001071, 2005. 2
- Lohofener, A.: Design and development of a multi-channel radar depth sounder, Ph.D. thesis, University of Kansas, 2006. 54
- Looyenga, H.: Dielectric constants of heterogeneous mixtures, *Physica*, 31, 401–406, doi:10.1016/0031-8914(65)90045-5, 1965. 10, 29
- MacGregor, J. A., Fahnestock, M. A., Catania, G. A., Paden, J. D., Prasad Gogineni, S., Young, S. K., Rybarski, S. C., Mabrey, A. N., Wagman, B. M., and Morlighem, M.: Radiostratigraphy and age structure of the Greenland Ice Sheet, *Journal of Geophysical Research: Earth Surface*, 120, 212–241, doi:10.1002/2014JF003215, 2015a. 5, 26, 52, 65
- MacGregor, J. A., Li, J., Paden, J. D., Catania, G. A., Clow, G. D., Fahnestock, M. A., Prasad Gogineni, S., Grimm, R. E., Morlighem, M., Nandi, S., et al.: Radar attenuation and temperature within the Greenland Ice Sheet, *Journal of Geophysical Research: Earth Surface*, 120, 983–1008, doi:10.1002/2014JF003418, 2015b. 5, 27, 43, 45, 52
- MacGregor, J. A., Fahnestock, M. A., Catania, G. A., Aschwanden, A., Clow, G. D., Colgan, W. T., Gogineni, S. P., Morlighem, M., Nowicki, S. M., Paden, J. D., et al.: A synthesis of the basal thermal state of the Greenland Ice Sheet, *Journal of Geophysical Research: Earth Surface*, 121, 1328–1350, doi:10.1002/2015JF003803, 2016. 5, 52, 88
- Malinverno, A.: A simple method to estimate the fractal dimension of a self-affine series, *Geophysical Research Letters*, 17, 1953–1956, doi:10.1029/GL017i011p01953, 1990. 72, 78
- Masson-Delmotte, V., Schulz, M., Abe-Ouchi, A., Beer, J., Ganopolski, A., González Rouco, J., Jansen, E., Lambeck, K., Luterbacher, J., Naish, T., Osborn, T., Otto-Bliesner, B., Quinn, T., Ramesh, R., Rojas, M., Shao, X., and Timmermann, A.: Information from Paleoclimate Archives, in: *Climate Change 2013: The Physical Science Basis. Contribution of Working Group I to the Fifth Assessment Report of the Intergovernmental Panel on Climate Change.*, edited by Stocker, T., Qin, D., Plattner, G.-K., Tignor, M., Allen, S., Boschung, J., Nauels, A., Xia, Y., Bex, V., and Midgley, P., p. 383ff, Cambridge Univ Press, Cambridge, United Kingdom and New York, NY, USA, 2013. 2
- Matsuoka, K., Furukawa, T., Fujita, S., Maeno, H., Uratsuka, S., Naruse, R., and Watanabe, O.: Crystal orientation fabrics within the Antarctic ice sheet revealed by a multipolarization plane and dual-frequency radar survey, *Journal of Geophysical Research: Solid Earth*, 108, doi:10.1029/2003JB002425, 2003. 43
- Matsuoka, K., Morse, D., and Raymond, C.: Estimating englacial radar attenuation using depth profiles of the returned power, central West Antarctica, *Journal of Geophysical Research: Earth Surface*, 115, 1–15, doi:10.1029/2009JF001496, 2010. 27

-
- Matsuoka, T., Fujita, S., and Mae, S.: Effect of temperature on dielectric properties of ice in the range 5–39 GHz, *Journal of Applied Physics*, 80, 5884–5890, doi:10.1063/1.363582, 1996. 12
- Matsuoka, T., Fujita, S., Morishima, S., and Mae, S.: Precise measurement of dielectric anisotropy in ice Ih at 39 GHz, *Journal of Applied Physics*, 81, 2344–2348, doi:10.1063/1.364238, 1997. 46
- Maxwell, J. C.: A dynamical theory of the electromagnetic field, The Royal Society London, 1864. 9
- Milankovitch, M.: *Kanon der Erdbestrahlung*, Royal Serbian Academy, Spec. publ. 132, Sect. Math Nat. Sci, 1941. 2
- Millar, D.: Radio-echo layering in polar ice sheets and past volcanic activity, *Letters to Nature*, 292, 441–443, doi:10.1038/292441a0, 1981. 12, 26
- Miller, K. G., Wright, J. D., and Fairbanks, R. G.: Unlocking the ice house: Oligocene-Miocene oxygen isotopes, eustasy, and margin erosion, *Journal of Geophysical Research: Solid Earth*, 96, 6829–6848, doi:10.1029/90JB02015, 1991. 6
- Miller, K. G., Wright, J. D., Browning, J. V., Kulpecz, A., Kominz, M., Naish, T. R., Cramer, B. S., Rosenthal, Y., Peltier, W. R., and Sostdian, S.: High tide of the warm Pliocene: Implications of global sea level for Antarctic deglaciation, *Geology*, 40, 407–410, doi:10.1130/G32869.1, 2012. 5
- Moore, J.: High-resolution dielectric profiling of ice cores, *Journal of Glaciology*, 39, 245–248, 1993. 11, 28
- Mouginot, J., Rignot, E., Scheuchl, B., and Millan, R.: Comprehensive annual ice sheet velocity mapping using Landsat-8, Sentinel-1, and RADARSAT-2 data, *Remote Sensing*, 9, 364, doi:10.3390/rs9040364, 2017a. 77, 80
- Mouginot, J., Scheuchl, B., and Rignot, E.: MEaSUREs Annual Antarctic Ice Velocity Maps 2005-2017, Version 1, Boulder, Colorado USA, NASA National Snow and Ice Data Center Distributed Active Archive Center (Accessed: 19 Oct 2016), doi:10.5067/9T4EPQXTJYW9, 19.10.2016, 2017b. 77, 80
- Münch, T., Kipfstuhl, S., Freitag, J., Meyer, H., and Laepple, T.: Regional climate signal vs. local noise: a two-dimensional view of water isotopes in Antarctic firn at Kohnen station, Dronning Maud Land, *Climate of the Past*, 12, 1565–1581, doi:doi:10.5194/cp-12-1565-2016, 2016. 44
- Navarro, F. and Eisen, O.: Ground-penetrating radar, chap. 11, pp. 1–32, 2009. 9, 11, 13, 14
- NEEM community members: Eemian interglacial reconstructed from a Greenland folded ice core, *Nature*, 493, 489, doi:10.1038/nature11789, 2013. 4, 52
- Nereson, N., Raymond, C., Waddington, E., and Jacobel, R.: Migration of the Siple Dome ice divide, West Antarctica, *Journal of Glaciology*, 44, 643–652, doi:10.3189/S0022143000002148, 1998. 4
- Nereson, N. A. and Waddington, E. D.: Isochrones and isotherms beneath migrating ice divides, *Journal of Glaciology*, 48, 95–108, doi:10.3189/172756502781831647, 2002. 3

- Nixdorf, U., Steinhage, D., Meyer, U., Hempel, L., Jenett, M., Wachs, P., and Miller, H.: The newly developed airborne radio-echo sounding system of the AWI as a glaciological tool, *Annals of Glaciology*, 29, 231–238, doi:10.3189/172756499781821346, 1999. 16, 31, 54
- NOAA: EPICA Dome C Ice Cores Dielectrical Profiling (DEP) Data, ftp://ftp.ncdc.noaa.gov/pub/data/paleo/icecore/antarctica/epica_domec/edc2011dep.txt, (Accessed: 26 Feb 2016), 2011. 28
- Nowicki, S., Bindschadler, R. A., Abe-Ouchi, A., Aschwanden, A., Bueller, E., Choi, H., Fastook, J., Granzow, G., Greve, R., Gutowski, G., Herzfeld, U., Jackson, C., Johnson, J., Khroulev, C., Larour, E., Levermann, A., Lipscomb, W. H., Martin, M. A., Morlighem, M., Parizek, B. R., Pollard, D., Price, S. F., Ren, D., Rignot, E., Saito, F., Sato, T., Seddik, H., Seroussi, H., Takahashi, K., Walker, R., and Wang, W. L.: Insights into spatial sensitivities of ice mass response to environmental change from the SeaRISE ice sheet modeling project I: Antarctica, *Journal of Geophysical Research: Earth Surface*, 118, 1002–1024, doi:10.1002/jgrf.20081, 2013. 56
- Nowicki, S. M. J., Payne, A., Larour, E., Seroussi, H., Goelzer, H., Lipscomb, W., Gregory, J., Abe-Ouchi, A., and Shepherd, A.: Ice Sheet Model Intercomparison Project (ISMIP6) contribution to CMIP6, *Geoscientific Model Development*, 9, 4521–4545, doi:10.5194/gmd-9-4521-2016, 2016. 84
- Nye, J.: Glacier sliding without cavitation in a linear viscous approximation, in: *Proceedings of the Royal Society of London A: Mathematical, Physical and Engineering Sciences*, vol. 315, pp. 381–403, The Royal Society, doi:10.1098/rspa.1970.0050, 1970. 72
- Oswald, G. and Gogineni, S.: Recovery of subglacial water extent from Greenland radar survey data, *Journal of Glaciology*, 54, 94–106, doi:10.3189/002214308784409107, 2008. 4
- Oswald, G. and Robin, G. d. Q.: Lakes beneath the Antarctic ice sheet, *Nature*, 245, 251, doi:10.1038/245251a0, 1973. 4, 85
- Oswald, G. K.: Investigation of sub-ice bedrock characteristics by radio-echo sounding, *Journal of Glaciology*, 15, 75–87, doi:10.3189/S0022143000034286, 1975. 4
- Oswald, G. K. A. and Gogineni, S. P.: Mapping Basal Melt Under the Northern Greenland Ice Sheet, *IEEE Transactions on Geoscience and Remote Sensing*, 50, 585–592, doi:10.1109/TGRS.2011.2162072, 2012. 72
- Palais, J. M., Whillans, I. M., and Bull, C.: Snow stratigraphic studies at Dome C, East Antarctica: an investigation of depositional and diagenetic processes, *Ann. Glaciol.*, 3, 239–242, doi:10.3189/S0260305500002846, 1982. 44
- Panton, C.: Automated mapping of local layer slope and tracing of internal layers in radio echograms, *Annals of Glaciology*, 55, 71–77, doi:10.3189/2014AoG67A048, 2014. 65
- Panton, C. and Karlsson, N. B.: Automated mapping of near bed radio-echo layer disruptions in the Greenland Ice Sheet, *Earth and Planetary Science Letters*, 432, 323–331, doi:10.1016/j.epsl.2015.10.024, 2015. 4

- Paolo, F. S., Fricker, H. A., and Padman, L.: Volume loss from Antarctic ice shelves is accelerating, *Science*, 348, 327–331, doi:10.1126/science.aaa0940, 2015. 5
- Paren, J. and Robin, G. d. Q.: Internal reflections in polar ice sheets, *Journal of Glaciology*, 14, 251–259, doi:https://doi.org/10.3189/S0022143000021730, 1975. 4, 12
- Parrenin, F., Petit, J.-R., Masson-Delmotte, V., Wolff, E., Basile-Doelsch, I., Jouzel, J., Lipenkov, V., Rasmussen, S. O., Schwander, J., Severi, M., et al.: Volcanic synchronisation between the EPICA Dome C and Vostok ice cores (Antarctica) 0–145 kyr BP, *Climate of the Past*, 8, 1031–1045, doi:10.5194/cp-8-1031-2012, 2012. 28, 46
- Parrenin, F., Cavitte, M. G., Blankenship, D. D., Chappellaz, J., Fischer, H., Gagliardini, O., Masson-Delmotte, V., Passalacqua, O., Ritz, C., Roberts, J., Siegert, M. J., and Young, D. A.: Is there 1.5 million-year old ice near Dome C, Antarctica?, *The Cryosphere Discuss.*, doi:10.5194/tc-2017-69, 2017. 51, 52
- Pellikka, P. and Rees, W. G.: Remote sensing of glaciers: techniques for topographic, spatial and thematic mapping of glaciers, CRC Press, 2009. 10
- Peters, M. E., Blankenship, D. D., and Morse, D. L.: Analysis techniques for coherent airborne radar sounding: Application to West Antarctic ice streams, *Journal of Geophysical Research: Solid Earth*, 110, doi:10.1029/2004JB003222, 2005. 33
- Peters, M. E., Blankenship, D. D., Carter, S. P., Kempf, S. D., Young, D. A., and Holt, J. W.: Along-track focusing of airborne radar sounding data from West Antarctica for improving basal reflection analysis and layer detection, *IEEE Transactions on Geoscience and Remote Sensing*, 45, 2725–2736, doi:10.1109/TGRS.2007.897416, 2007. 33, 74
- Plewes, L. A. and Hubbard, B.: A review of the use of radio-echo sounding in glaciology, *Progress in Physical Geography*, 25, 203–236, doi:10.1177/030913330102500203, 2001. 9, 11
- Podolskiy, E. A. and Walter, F.: Cryoseismology, *Reviews of Geophysics*, 54, 708–758, doi:10.1002/2016RG000526, 2016. 71
- Rahmstorf, S.: Ocean circulation and climate during the past 120,000 years, *Nature*, 419, 207–214, doi:10.1038/nature01090, 2002. 1
- Raymo, M., Lisiecki, L., and Nisancioglu, K. H.: Plio-Pleistocene ice volume, Antarctic climate, and the global $\delta^{18}\text{O}$ record, *Science*, 313, 492–495, doi:10.1126/science.1123296, 2006. 2, 26
- Raymond, C. F.: Deformation in the vicinity of ice divides, *Journal of Glaciology*, 29, 357–373, doi:10.3189/S0022143000030288, 1983. 3, 4, 111
- Rémy, F. and Tabacco, I. E.: Bedrock features and ice flow near the EPICA ice core site (Dome C, Antarctica), *Geophysical Research Letters*, 27, 405–408, doi:10.1029/1999GL006067, 2000. 43
- Richardson, C. and Holmlund, P.: Spatial variability at shallow snow-layer depths in central Dronning Maud Land, East Antarctica, *Annals of Glaciology*, 29, 10–16, doi:10.3189/172756499781820905, 1999. 44

- Rignot, E., Velicogna, I., van den Broeke, M. R., Monaghan, A., and Lenaerts, J. T.: Acceleration of the contribution of the Greenland and Antarctic ice sheets to sea level rise, *Geophysical Research Letters*, 38, doi:10.1029/2011GL046583, 2011. 1
- Rippin, D., Bamber, J., Siegert, M., Vaughan, D., and Corr, H.: Basal topography and ice flow in the Bailey/Slessor region of East Antarctica, *Journal of Geophysical Research: Earth Surface*, 108, doi:10.1029/2003JF000039, 2003a. 83
- Rippin, D., Bingham, R., Jordan, T., Wright, A., Ross, N., Corr, H., Ferraccioli, F., Le Brocq, A., Rose, K., and Siegert, M.: Basal roughness of the Institute and Möller Ice Streams, West Antarctica: Process determination and landscape interpretation, *Geomorphology*, 214, 139–147, doi:10.1016/j.geomorph.2014.01.021, 2014. 4, 82, 83
- Rippin, D. M., Siegert, M. J., and Bamber, J. L.: The englacial stratigraphy of Wilkes Land, East Antarctica, as revealed by internal radio-echo sounding layering, and its relationship with balance velocities, *Annals of Glaciology*, 36, 189–196, doi:10.3189/172756403781816356, 2003b. 65
- Ritz, C., Edwards, T. L., Durand, G., Payne, A. J., Peyaud, V., and Hindmarsh, R. C.: Potential sea-level rise from Antarctic ice-sheet instability constrained by observations, *Nature*, 528, 115, doi:10.1038/nature16147, 2015. 5, 71, 72
- Robin, G. d. Q., Evans, S., and Bailey, J. T.: Interpretation of radio echo sounding in polar ice sheets, *Phil. Trans. R. Soc. Lond. A*, 265, 437–505, doi:10.1098/rsta.1969.0063, 1969. 4, 12
- Robin, G. d. Q., Swithinbank, C., Smith, B., et al.: Radio echo exploration of the Antarctic ice sheet, *International Association of Scientific Hydrology Publication*, 86, 97–115, 1970. 4, 52
- Rodriguez-Morales, F., Gogineni, S., Leuschen, C. J., Paden, J. D., Li, J., Lewis, C. C., Panzer, B., Gomez-Garcia Alvestegui, D., Patel, A., Byers, K., et al.: Advanced multifrequency radar instrumentation for polar research, *Geoscience and Remote Sensing, IEEE Transactions on*, 52, 2824–2842, doi:10.1109/TGRS.2013.2266415, 2014. 26, 31, 32, 52
- Roesli, C., Helmstetter, A., Walter, F., and Kissling, E.: Meltwater influences on deep stick-slip icequakes near the base of the Greenland Ice Sheet, *Journal of Geophysical Research: Earth Surface*, 121, 223–240, doi:10.1002/2015JF003601, 2016. 72
- Shapiro, N. M. and Ritzwoller, M. H.: Inferring surface heat flux distributions guided by a global seismic model: particular application to Antarctica, *Earth and Planetary Science Letters*, 223, 213–224, doi:10.1016/j.epsl.2004.04.011, 2004. 56
- Shepard, M. K., Campbell, B. A., Bulmer, M. H., Farr, T. G., Gaddis, L. R., and Plaut, J. J.: The roughness of natural terrain: A planetary and remote sensing perspective, *Journal of Geophysical Research: Planets*, 106, 32 777–32 795, doi:10.1029/2000JE001429, 2001. 75, 78
- Shepherd, A., Ivins, E. R., Geruo, A., Barletta, V. R., Bentley, M. J., Bettadpur, S., Briggs, K. H., Bromwich, D. H., Forsberg, R., Galin, N., et al.: A reconciled estimate of ice-sheet mass balance, *Science*, 338, 1183–1189, doi:10.1126/science.1228102, 2012. 5

-
- Shepherd, T., Bamber, J., and Ferraccioli, F.: Subglacial geology in Coats Land, East Antarctica, revealed by airborne magnetics and radar sounding, *Earth and Planetary Science Letters*, 244, 323–335, doi:10.1016/j.epsl.2006.01.068, 2006. 71, 83
- Siegert, M. J., Hodgkins, R., and Dowdeswell, J. A.: A chronology for the Dome C deep ice-core site through radio-echo layer Correlation with the Vostok Ice Core, Antarctica, *Geophysical Research Letters*, 25, 1019–1022, doi:10.1029/98GL00718, 1998. 4
- Siegert, M. J., Taylor, J., and Payne, A. J.: Spectral roughness of subglacial topography and implications for former ice-sheet dynamics in East Antarctica, *Global and Planetary Change*, 45, 249–263, doi:10.1016/j.gloplacha.2004.09.008, 2005. 4, 75, 85
- Sime, L. C., Hindmarsh, R. C., and Corr, H.: Automated processing to derive dip angles of englacial radar reflectors in ice sheets, *Journal of Glaciology*, 57, 260–266, doi:10.3189/002214311796405870, 2011. 65
- Sime, L. C., Karlsson, N. B., Paden, J. D., and Prasad Gogineni, S.: Isochronous information in a Greenland ice sheet radio echo sounding data set, *Geophysical Research Letters*, 41, 1593–1599, doi:10.1002/2013GL057928, 2014. 27, 52
- Steinhage, D., Kipfstuhl, S., Nixdorf, U., and Miller, H.: Internal structure of the ice sheet between Kohlen station and Dome Fuji, Antarctica, revealed by airborne radio-echo sounding, *Annals of Glaciology*, 54, 163–167, doi:10.3189/2013AoG64A113, 2013. 4, 27, 52, 55
- Studinger, M., Bell, R. E., Karner, G. D., Tikku, A. A., Holt, J. W., Morse, D. L., Richter, T. G., Kempf, S. D., Peters, M. E., Blankenship, D. D., et al.: Ice cover, landscape setting, and geological framework of Lake Vostok, East Antarctica, *Earth and Planetary Science Letters*, 205, 195–210, doi:10.1016/S0012-821X(02)01041-5, 2003. 58
- Svensson, A., Bigler, M., Blunier, T., Clausen, H., Dahl-Jensen, D., Fischer, H., Fujita, S., Goto-Azuma, K., Johnsen, S., Kawamura, K., et al.: Direct linking of Greenland and Antarctic ice cores at the Toba eruption (74 ka BP), *Climate of the Past*, 9, 749, doi:10.5194/cp-9-749-2013, 2013. 55
- Tabacco, I., Cianfarra, P., Forieri, A., Salvini, F., and Zirizotti, A.: Physiography and tectonic setting of the subglacial lake district between Vostok and Belgica subglacial highlands (Antarctica), *Geophysical Journal International*, 165, 1029–1040, doi:10.1111/j.1365-246X.2006.02954.x, 2006. 85
- Taflove, A. and Hagness, S. C.: *Computational electrodynamics: the finite-difference time-domain method*, Norwood, 2nd Edition, MA: Artech House, 1995, 1995. 30
- Taylor, J., Siegert, M. J., Payne, A. J., and Hubbard, B.: Regional-scale bed roughness beneath ice masses: measurement and analysis, *Computers & geosciences*, 30, 899–908, doi:10.1016/j.cageo.2004.06.007, 2004. 72
- The EPICA Dome C 2001-02, science and drilling teams: Extending the ice core record beyond half a million years, *EOS Transactions*, 83, 509, 2002. 28

- The PISM authors: PISM, a Parallel Ice Sheet Model, <http://www.pism-docs.org>, 2016. 56
- Thornalley, D. J. R., Oppo, D. W., Ortega, P., Robson, J. I., Brierley, C. M., Davis, R., Hall, I. R., Moffa-Sanchez, P., Rose, N. L., Spooner, P. T., Yashayaev, I., and Keigwin, L. D.: Anomalously weak Labrador Sea convection and Atlantic overturning during the past 150 years, *Nature*, 556, 227–230, doi:10.1038/s41586-018-0007-4, 2018. 1
- Urbini, S., Frezzotti, M., Gandolfi, S., Vincent, C., Scarchilli, C., Vittuari, L., and Fily, M.: Historical behaviour of Dome C and Talos Dome (East Antarctica) as investigated by snow accumulation and ice velocity measurements, *Global and Planetary Change*, 60, 576–588, doi:10.1016/j.gloplacha.2007.08.002, 2008. 3, 26, 41, 42
- Urbini, S., Cafarella, L., Tabacco, I. E., Baskaradas, J. A., Serafini, M., and Zirizzotti, A.: RES Signatures of Ice Bottom Near to Dome C (Antarctica), *IEEE Transactions on Geoscience and Remote Sensing*, 53, 1558–1564, doi:10.1109/TGRS.2014.2345457, 2015. 4, 33, 52
- Van Liefferinge, B., Pattyn, F., Cavitte, M. G., Karlsson, N. B., Young, D. A., Sutter, J., and Eisen, O.: Promising Oldest Ice sites in East Antarctica based on thermodynamical modelling, doi:10.5194/tc-2017-276, 2018. 6
- Van Wessem, J., Reijmer, C., Morlighem, M., Mouginot, J., Rignot, E., Medley, B., Joughin, I., Wouters, B., Depoorter, M., Bamber, J., Lenaerts, J., De Van Berg, W., Van Den Broeke, M., and Van Meijgaard, E.: Improved representation of East Antarctic surface mass balance in a regional atmospheric climate model, *Journal of Glaciology*, 60, 761–770, doi:10.3189/2014JG14J051, 2014. 56
- Vaughan, D., Comiso, J., Allison, I., Carrasco, J., Kaser, G., Kwok, R., Mote, P., Murray, T., Paul, F., Ren, J., Rignot, E., Solomina, O., Steffen, K., and Zhang, T.: Observations: Cryosphere, in: *Climate Change 2013: The Physical Science Basis. Contribution of Working Group I to the Fifth Assessment Report of the Intergovernmental Panel on Climate Change*, edited by Stocker, T., Qin, D., Plattner, G.-K., Tignor, M., Allen, S., Boschung, J., Nauels, A., Xia, Y., Bex, V., and Midgley, P., Cambridge Univ Press, Cambridge, United Kingdom and New York, NY, USA, 2013. 1, 5, 6
- Vaughan, D. G., Corr, H. F., Doake, C. S., and Waddington, E. D.: Distortion of isochronous layers in ice revealed by ground-penetrating radar, *Nature*, 398, 323–326, doi:10.1038/18653, 1999. 4, 26
- Veen, C. and Bolzan, J.: Interannual variability in net accumulation on the Greenland Ice Sheet: Observations and implications for mass balance measurements, *Journal of Geophysical Research: Atmospheres*, 104, 2009–2014, doi:10.1029/1998JD200082, 1999. 44
- Velicogna, I., Sutterley, T., and Van Den Broeke, M.: Regional acceleration in ice mass loss from Greenland and Antarctica using GRACE time-variable gravity data, *Geophysical Research Letters*, 41, 8130–8137, doi:10.1002/2014GL061052, 2014. 5
- Veres, D., Bazin, L., Landais, A., Toyé Mahamadou Kele, H., Lemieux-Dudon, B., Parrenin, F., Martinerie, P., Blayo, E., Blunier, T., Capron, E., et al.: The Antarctic ice core chronology (AICC2012):

- an optimized multi-parameter and multi-site dating approach for the last 120 thousand years, *Climate of the Past*, 9, 1733–1748, doi:10.5194/cp-9-1733-2013, 2013. 39, 40, 46, 55, 58, 66
- Waddington, E. D., Neumann, T. A., Koutnik, M. R., Marshall, H.-P., and Morse, D. L.: Inference of accumulation-rate patterns from deep layers in glaciers and ice sheets, *Journal of Glaciology*, 53, 694–712, doi:10.3189/002214307784409351, 2007. 51
- Walker, R. T.: Grounded meets floating, *Nature Geoscience*, p. 1, doi:10.1038/s41561-018-0098-4, 2018. 5
- Weertman, J.: Deep Steady-State Creep through Dislocation Climb, *Journal of Applied Physics*, 28, 362–364, doi:10.1063/1.1722747, 1957. 72
- Weertman, J.: Sliding-no sliding zone effect and age determination of ice cores, *Quaternary Research*, 6, 203–207, 1976. 64
- Wilhelms, F.: Explaining the dielectric properties of firn as a density-and-conductivity mixed permittivity (DECOMP), *Geophysical Research Letters*, 32, doi:10.1029/2005GL022808, 2005. 29
- Wilkens, N., Behrens, J., Kleiner, T., Rippin, D., Rückamp, M., and Humbert, A.: Thermal structure and basal sliding parametrisation at Pine Island Glacier—a 3-D full-Stokes model study, *The Cryosphere*, 9, 675–690, doi:10.5194/tc-9-675-2015, 2015. 72
- Williams, T., van de Flierdt, T., Hemming, S. R., Chung, E., Roy, M., and Goldstein, S. L.: Evidence for iceberg armadas from East Antarctica in the Southern Ocean during the late Miocene and early Pliocene, *Earth and Planetary Science Letters*, 290, 351–361, doi:10.1016/j.epsl.2009.12.031, 2010. 5
- Winkelmann, R., Martin, M. A., Haseloff, M., Albrecht, T., Bueler, E., Khroulev, C., and Levermann, A.: The Potsdam Parallel Ice Sheet Model (PISM-PIK) Part 1: Model description, *The Cryosphere*, 5, 715–726, doi:10.5194/tc-5-715-2011, 2011. 52, 56, 84
- Winsborrow, M. C., Clark, C. D., and Stokes, C. R.: What controls the location of ice streams?, *Earth-Science Reviews*, 103, 45–59, doi:10.1016/j.earscirev.2010.07.003, 2010. 72
- Winter, A., Steinhage, D., Arnold, E. J., Blankenship, D. D., Cavitte, M. G., Corr, H. F., Paden, J. D., Urbini, S., Young, D. A., and Eisen, O.: Comparison of measurements from different radio-echo sounding systems and synchronization with the ice core at Dome C, Antarctica, *The Cryosphere*, 11, 653–668, doi:10.5194/tc-11-653-2017, 2017. 5, 21, 25, 55
- Winter, K., Woodward, J., Ross, N., Dunning, S. A., Bingham, R. G., Corr, H. F., and Siegert, M. J.: Airborne radar evidence for tributary flow switching in Institute Ice Stream, West Antarctica: Implications for ice sheet configuration and dynamics, *Journal of Geophysical Research: Earth Surface*, 120, 1611–1625, doi:10.1002/2015JF003518, 2015. 3, 27
- Wolff, E., Basile, I., Petit, J.-R., and Schwander, J.: Comparison of Holocene electrical records from Dome C and Vostok, Antarctica, *Annals of Glaciology*, 29, 89–93, doi:10.3189/172756499781820888, 1999. 46

- Wolff, E. W., Cook, E., Barnes, P. R., and Mulvaney, R.: Signal variability in replicate ice cores, *Journal of Glaciology*, 51, 462–468, doi:10.3189/172756505781829197, 2005. 45
- Wolovick, M. J., Bell, R. E., Creyts, T. T., and Frearson, N.: Identification and control of subglacial water networks under Dome A, Antarctica, *Journal of Geophysical Research: Earth Surface*, 118, 140–154, doi:10.1029/2012JF002555, 2013. 54, 74
- Wolovick, M. J., Creyts, T. T., Buck, W. R., and Bell, R. E.: Traveling slippery patches produce thickness-scale folds in ice sheets, *Geophysical Research Letters*, 41, 8895–8901, doi:10.1002/2014GL062248, 2014. 3, 4
- Wright, A. and Siegert, M.: A fourth inventory of Antarctic subglacial lakes, *Antarctic Science*, 24, 659–664, doi:10.1017/S095410201200048X, 2012. 85
- Wright, A., Young, D., Roberts, J., Schroeder, D., Bamber, J., Dowdeswell, J., Young, N., Le Brocq, A., Warner, R., Payne, A., et al.: Evidence of a hydrological connection between the ice divide and ice sheet margin in the Aurora Subglacial Basin, East Antarctica, *Journal of Geophysical Research: Earth Surface*, 117, doi:10.1029/2011JF002066, 2012. 74, 82, 84, 87
- Wrona, T., Wolovick, M. J., Ferraccioli, F., Corr, H., Jordan, T., and Siegert, M. J.: Position and variability of complex structures in the central East Antarctic Ice Sheet, *Geological Society, London, Special Publications*, 461, 113–129, doi:10.1144/SP461.12, 2018. 4, 74
- Young, D. A., Wright, A. P., Roberts, J. L., Warner, R. C., Young, N. W., Greenbaum, J. S., Schroeder, D. M., Holt, J. W., Sugden, D. E., Blankenship, D. D., et al.: A dynamic early East Antarctic Ice Sheet suggested by ice-covered fjord landscapes, *Nature*, 474, 72–75, doi:10.1038/nature10114, 2011. 5, 33, 74, 84, 87
- Young, D. A., Schroeder, D., Blankenship, D., Kempf, S. D., and Quartini, E.: The distribution of basal water between Antarctic subglacial lakes from radar sounding, *Phil. Trans. R. Soc. A*, 374, 20140 297, doi:10.1098/rsta.2014.0297, 2016. 74
- Young, D. A., Roberts, J. L., Ritz, C., Frezzotti, M., Quartini, E., Cavitte, M. G., Tozer, C. R., Steinhage, D., Urbini, S., Corr, H. F., et al.: High-resolution boundary conditions of an old ice target near Dome C, Antarctica, *The Cryosphere*, 11, 1897, doi:10.5194/tc-11-1897-2017, 2017. 5, 6, 52, 74, 75, 85

Appendix

Appendix A: Mapping the Raymond bump at Sørasen

In a small 'Introductory Study' into working with RES data, I investigated the ice ridge Sørasen, approximately 100 km south-west of Neumayer Station. An overview of the location is given in Fig. A1. At ice divides, so called Raymond bumps can evolve (first described by Raymond (1983)), due to the nonlinearity in Glen's flow law. The downward motion of the ice at the divide is slower than at the flanks, where the ice is softer due to the higher deviatoric stress (Drews et al., 2013). Such a structure can also be seen at Sørasen. To characterize the ridge and its Raymond bump, a RES survey was conducted in 2014, covering the Sørasen ridge with a dense grid of profiles. Furthermore, there are two older RES profiles from 1999 and 2006 crossing the ridge. The location of all profiles can be inferred from in Fig. A5.

Figures A2 and A3 show the RES images of the two crossing profiles from older surveys (99 and 06). The bump is clearly visible in the data and evolves into a double bump in the deep IRHs. By means of ice-flow modeling, where curves of modeled isochrones are fitted to the RES isochrones, the ice dynamics and stability of the ice divide can be investigated. Interestingly, the double bump (Fig. A2 and A3) can only be reproduced when including anisotropic ice flow and COF into the models (Drews et al., 2013). Figure A4 shows a RES image from the grid of the 2014 survey. The bump is visible in the data, but unfortunately those data are not of good quality and show an enhanced intensity loss with depth for all profiles. The data show only very shallow IRHs and do not reach deep enough to detect the double bump. Nevertheless, I used those data to map the Raymond bump at the Sørasen ridge. It is shown by the yellow lines in Fig. A5. It could not be resolved what causes the intensity loss in the 2014 data, so it was most probable a problem during data recording. As the data quality could not be regained in the processing, this study was dropped for the time being.

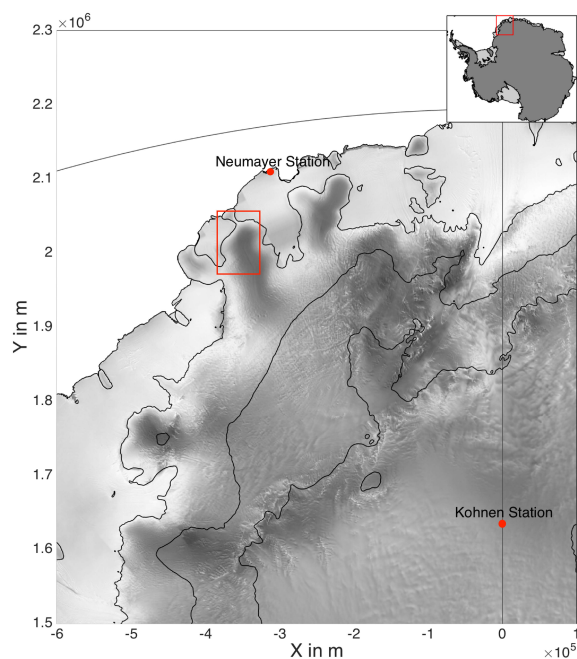


Figure A1. Location of the Sørasen ridge in East Antarctica. The red square is the frame of Fig. A5.

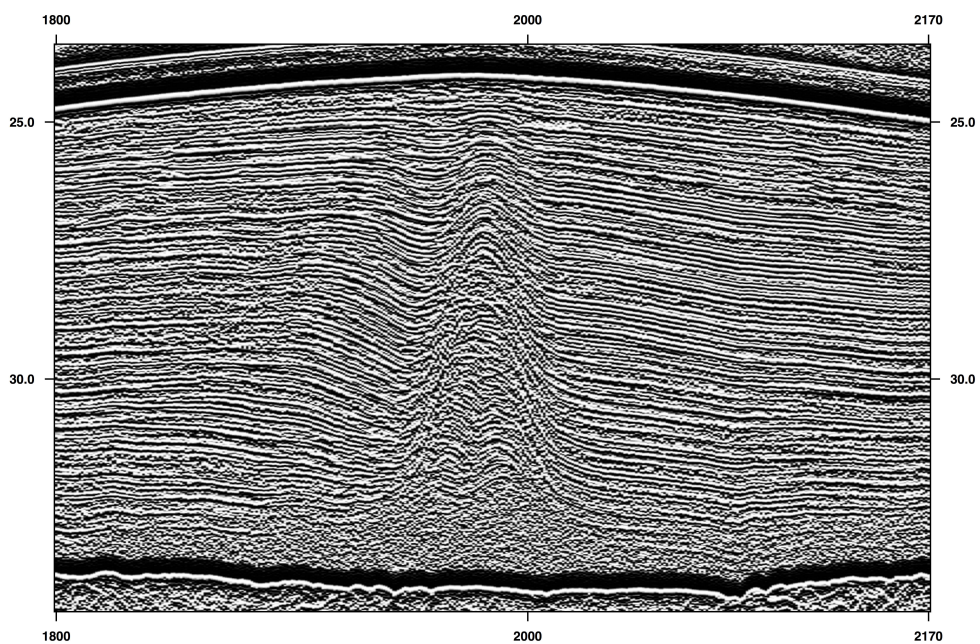


Figure A2. Radargram imaging the Raymond bump at Sørasen. The x-axis gives the trace number, the y-axis the TWT in μs . The data are recorded with the AWI system with 60 ns burst lengths and 10-fold horizontally stacked. The amplitude of the Raymond bump, which is clearly visible around trace 2000, increases with depth. In the very deep part it evolves into a double bump.

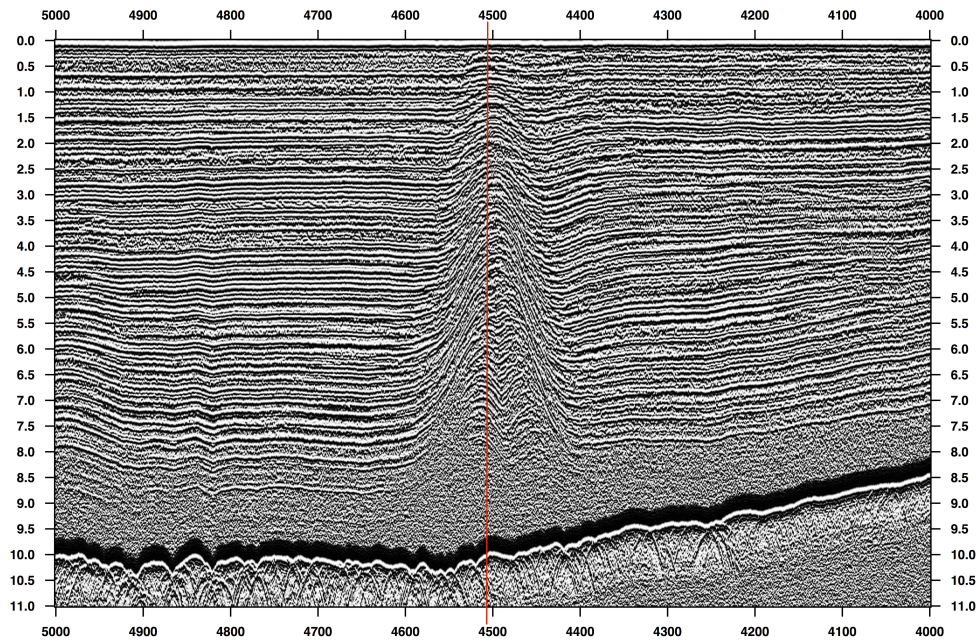


Figure A3. RES profile, perpendicular to the profile in Fig. A2 (\sim N-S direction). The red line indicates the crossing location. The x-axis gives the trace number, the y-axis the TWT in μs . The data are recorded with the AWI system with 60 ns burst lengths and 10-fold horizontally stacked. Here, the surface reflection is shifted to 0 μs .

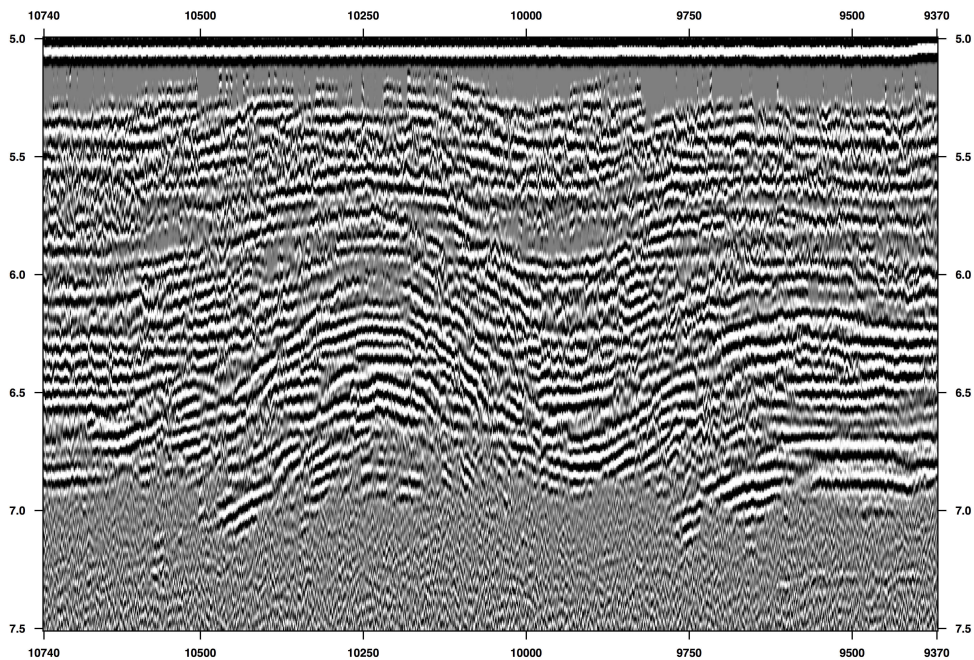


Figure A4. RES profile of the 2014 grid, imaging the Raymond bump at Sørasen. The x-axis gives the trace number, the y-axis the TWT in μs . The shallow part of the Raymond bump is visible around trace 10250. Note that the visible IRHs cease approximately 2 μs below the surface reflection (shifted to 5 μs), whereas IRHs are clearly visible down to 8.5 μs in Fig. A3.

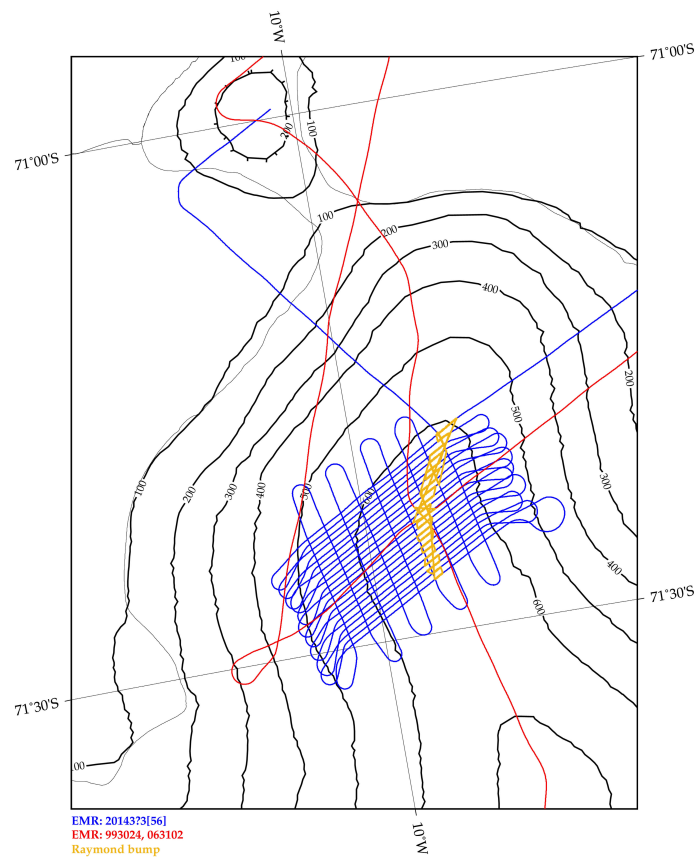


Figure A5. The grid of the 2014 RES survey at Sørasen (blue), older RES profiles (red) and the mapped location of the Raymond bump (yellow). The numbers below the figure are the profile names.

Appendix B: Exemplary RES images of structures seen in the radiostratigraphy

This section gives a few exemplary radargrams to illustrate which information about ice flow can be obtained from the radiostratigraphy. The first example shows a radargram from a region without considerable spatial or temporal changes of the ice flow characteristics (Fig. B1). The shallow IRHs are relatively flat, slowly aligning with the bed when moving deeper and remaining nearly parallel to each other. In that case, IRHs can easily be traced over long distances.

Figure B2 shows a radargram at Lake Vostok, where the base of the ice sheet is melting. The melting at the bottom pulls the IRHs downwards, they move faster in the vertical direction than in the surrounding region without basal melt. This has the effect that the IRHs are steeper than the subjacent bed topography. Furthermore, at smaller shot numbers (which is in the direction towards Dome C), there are unconformities in the stratigraphy. IRHs are no longer parallel, but have different slopes at different depths.

Figures B3, B4 and B5 show further examples of such unconformities in radargrams of different locations.

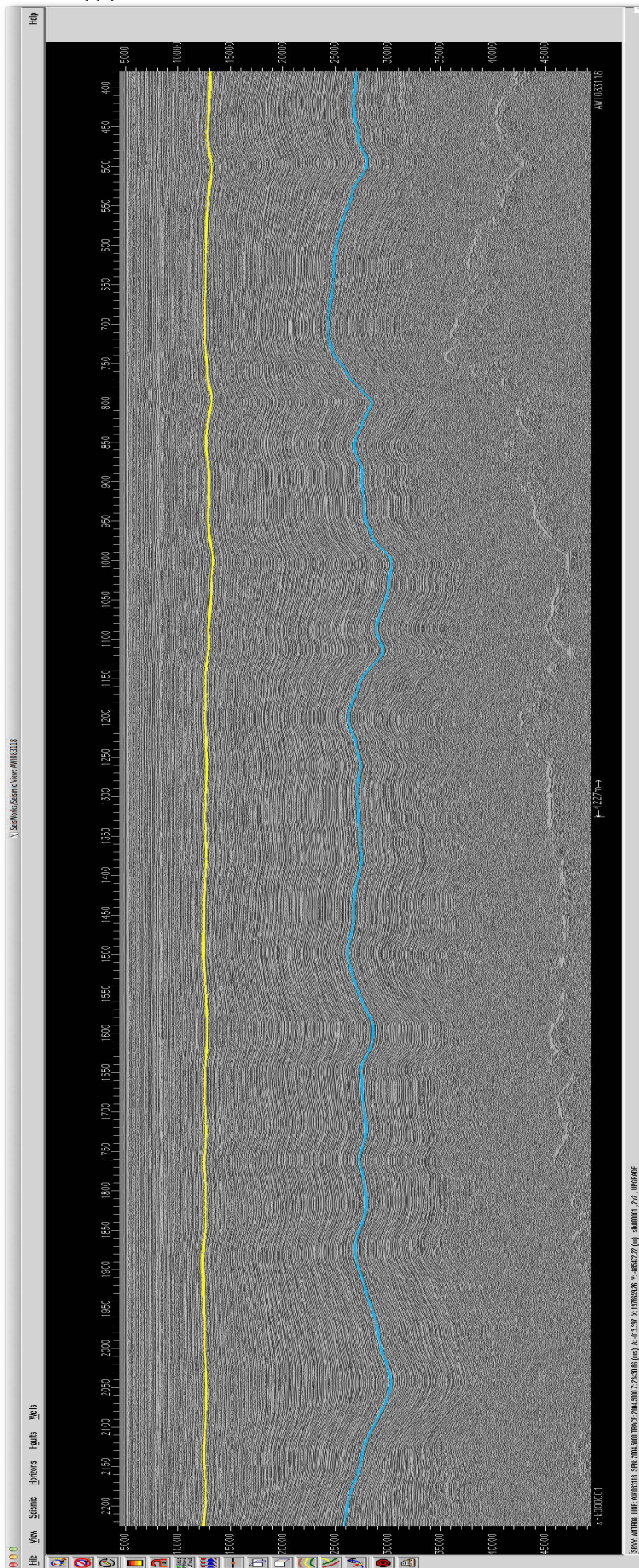


Figure B1. Example of a radargram (rotated) from a region with flat layering. TWT is given in ns. IRHs (e.g., the yellow and blue lines) can easily be traced over long distances. The overall distance of the shown section is nearly 200 km, the ice thickness approximately 3.5 km. The bed can be seen as a bright reflection close to the bottom (right) of the figure.

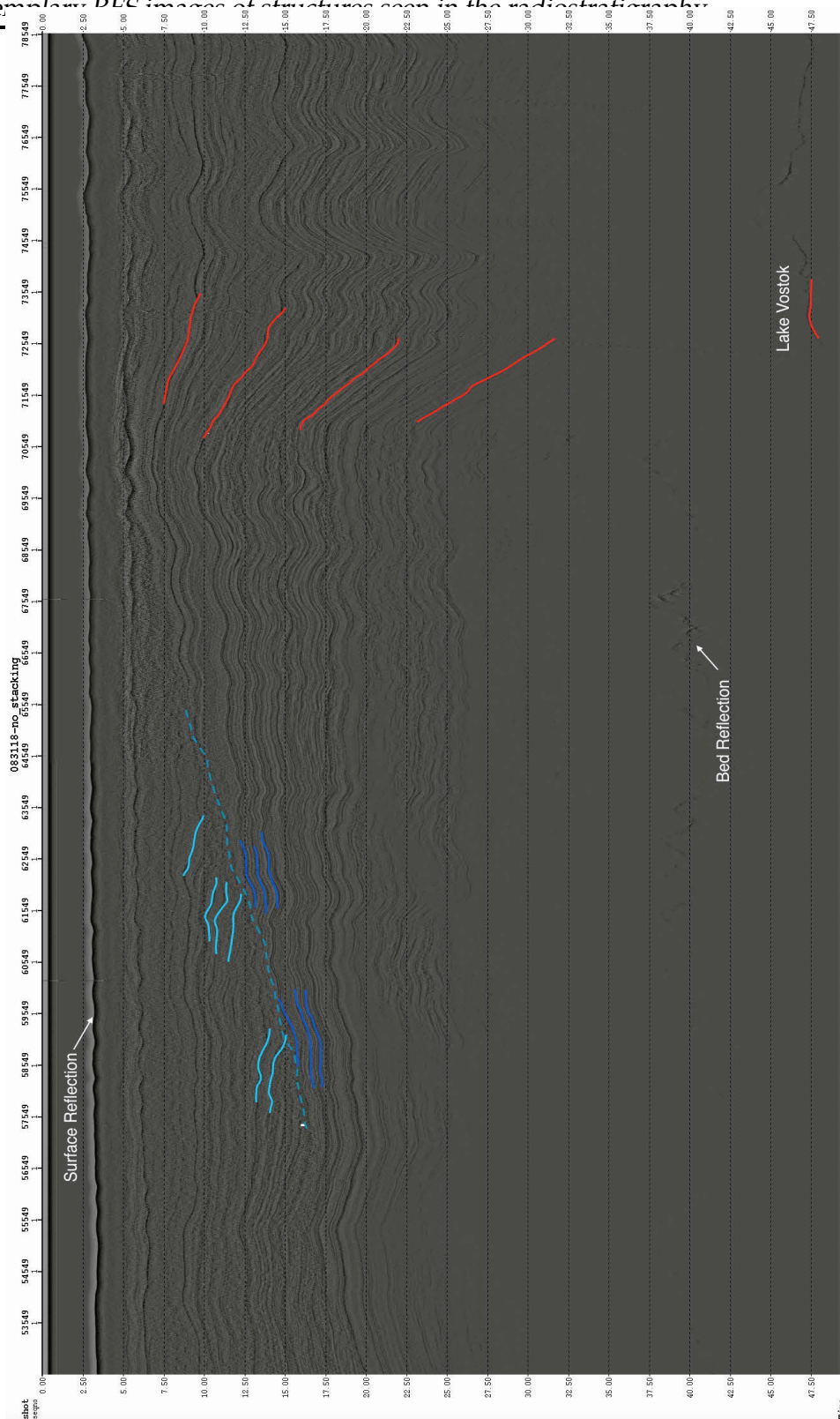


Figure B2. Example of a radargram (rotated) at Lake Vostok. The data are unfiltered and unstacked. x-axis is shot number, y-axis is TWT in μs . Isochrones are 'pulled downwards' above the lake, meaning they become steeper with depth (red lines), because of basal melt. At smaller shot numbers, unconformities in the stratigraphy can be seen. Isochrones at different depths are not parallel to each other (blue lines), indicating a change of flow direction, or surface erosion. In the latter case, the dashed line could be the eroded surface.

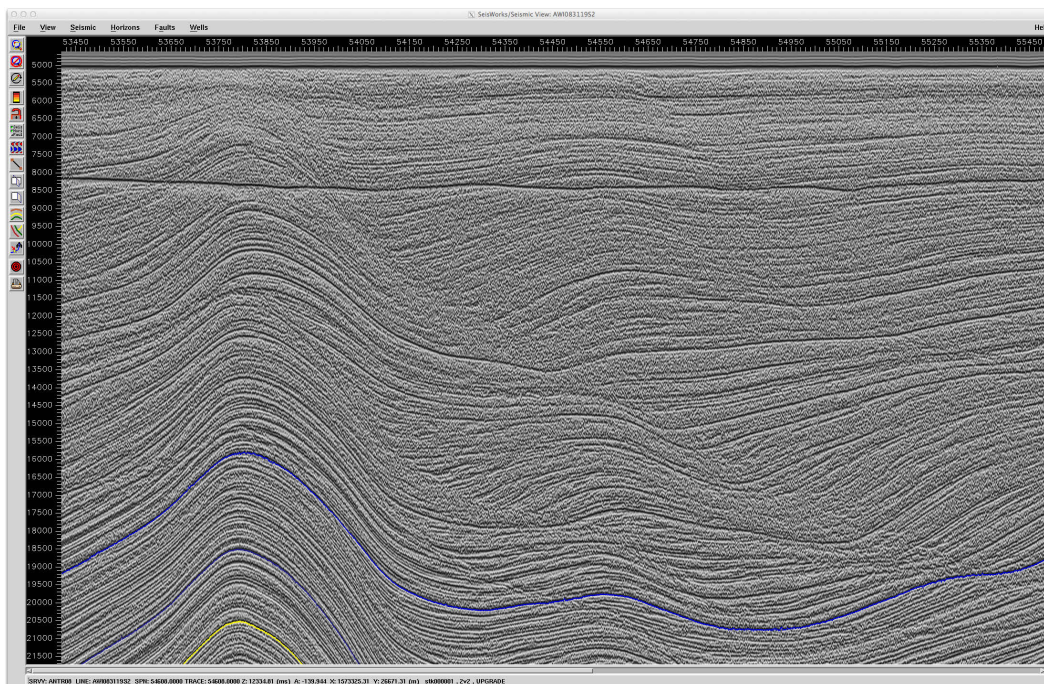


Figure B3. Radargram with disturbed stratigraphy, close to Dome A. The x-axis gives the trace number, the y-axis the TWT in ns.

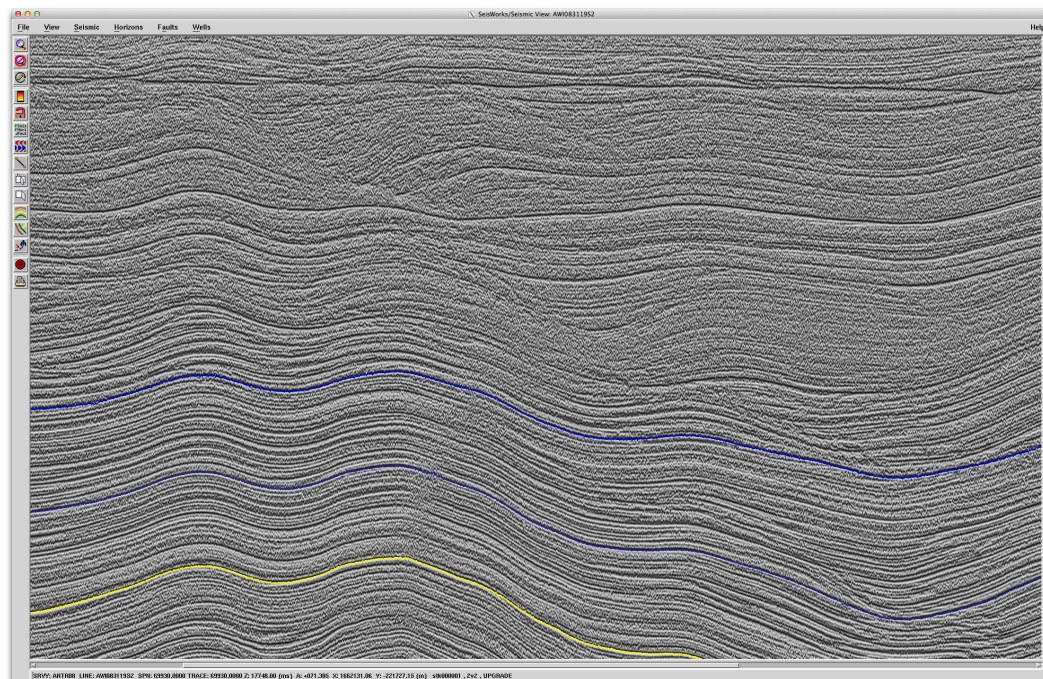


Figure B4. Radargram with disturbed stratigraphy, approximately half way between Vostok and Dome A. The deeper IRHs are continuous but shallower ones fade out. Either the flow field has changed, or paleo surfaces were eroded by wind and the stratigraphy was filled up at a later stage. This was taken as a screenshot without axes, but dimensions are approximately the same as in Fig. B3

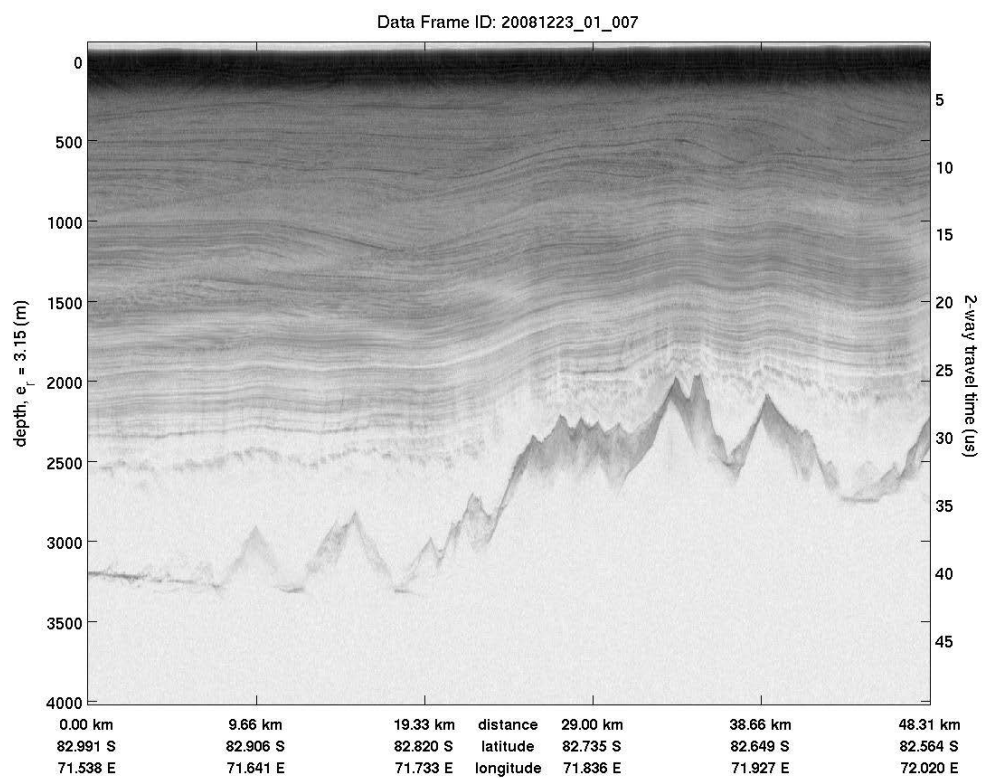


Figure B5. Radargram from the AGAP-S survey with disturbed stratigraphy (Antarctica's Gamburtsev Province Project - South, 2008/09). The x-axis gives the distance along the profile and the coordinates. Again the deeper IRHs are continuous and parallel, but shallower ones are highly nonparallel. This suggests several changes of flow direction in younger time periods, or surface erosion by wind scour.

Appendix C: List of publications

ISI peer-reviewed

Article

Winter, A. , Steinhage, D. , Arnold, E. J. , Blankenship, D. D. , Cavitte, M. G. P. , Corr, H. F. J. , Paden, J. D. , Urbini, S. , Young, D. A. and Eisen, O. (2017): **Comparison of measurements from different radio-echo sounding systems and synchronization with the ice core at Dome C, Antarctica**, *The Cryosphere*, 11 (1), pp. 653-668. doi:10.5194tc-11-653-2017, hdl:10013epic.50579

Article

Karlsson, N. B. , Eisen, O. , Dahl-Jensen, D. , Freitag, J. , Kipfstuhl, S. , Lewis, C. , Nielsen, L. T., Paden, J. , Winter, A. and Wilhelms, F. (2016): **Accumulation Rates during 1311 – 2011 CE in North-Central Greenland Derived from Air-Borne Radar Data**, *Frontiers in Earth Science*, 4, p. 97. doi:10.3389feart.2016.00097, hdl:10013epic.48973

In review

Article

Winter, A. , Kleiner, T. , Steinhage, D. , Creyts, T. T and Eisen, O.: **Deducing large-scale age distribution and paleo-accumulation rates from radiostratigraphy in East Antarctica**, *Journal of Glaciology*, submitted in November 2017

In preparation

Article

Winter, A. , Steinhage, D. , Helm, V. and Eisen, O.: **Basal roughness of the East Antarctic Ice Sheet and indications on ice flow and basal thermal state**, to be submitted in Mai 2018

Conferences

Conference-Poster

Winter, A. , Steinhage, D. , Kleiner, T. , Creyts, T. and Eisen, O. (2017): **Accumulation rates from 38 ka and 161 ka radio-echo sounding horizons in East Antarctica**, EGU General Assembly, Vienna, 24 April 2017 - 28 April 2017. hdl:10013epic.51249

Conference-Talk

Winter, A. , Eisen, O. , Steinhage, D. , Zirizzotti, A. , Urbini, S. , Cavitte, M. , Blankenship, D. D. and Wolff, E. (2016): **Radio-echo sounding at Dome C, East Antarctica: A comparison of measured and modeled data**, EGU General Assembly, Vienna, Austria, 18 April 2016 - 22 April 2016. hdl:10013epic.49861

Conference-Talk

Winter, A. , Eisen, O. and Steinhage, D. (2015): **RADAR INTERNAL LAYERS: SYNCHRONIZATION WITH ICE-CORE RECORDS AND LAYER TRACING**, 26th International Congress on Polar Research, Munich, Munich, Germany, 6 September 2015 - 11 September 2015. hdl:10013epic.46870

Danksagung

Zu guter Letzt möchte ich den Menschen einen ganz herzlichen Dank aussprechen, ohne die diese Arbeit nie vollendet worden wäre.

Ganz besonderer Dank geht an Olaf Eisen für die Ermöglichung meiner Promotion, die Begutachtung der Arbeit und vor allem für die hervorragende Betreuung während dieser nun fast vier Jahre. Wenn auch häufig per Mail oder telefonisch, bekam ich doch immer sofort eine Antwort auf meine Fragen. Es war gut, jemanden zu haben, der den Überblick behielt wenn ich mich verzettelte und immer hilfreiche Anregungen und Auswege aus vermeintlichen Sackgassen parat hatte.

Tilo von Dobeneck danke herzlich ich für die Übernahme der Korreferates.

Daniel Steinhage, Martin Werner und Martin Rückamp danke ich für ihre Bereitschaft, meinem Promotionskomitee beizutreten und ihre Zeit für die regelmäßigen Treffen.

Meinen Kollegen der Sektion Glaziologie möchte ich für die gemeinsame Zeit am AWI danken; davon insbesondere Daniel Steinhage für das Näherbringen diverser Radarsoftware und anderer Tricks und Kniffe im Umgang mit den Daten, Thomas Kleiner für anregende Diskussionen über Modellergebnisse, Andreas Frenzel für die Unterstützung in allen technischen Belangen und Daniela Jansen, Maddalena Bayer und Johanna Kerch für das Korrekturlesen der Arbeit.

Ich danke allen Beteiligten der Grönland- und Antarktisexpeditionen für die wundervolle Zeit im Eis und Olaf für die Möglichkeit diese zu erleben.

Meinen Freunden inner- und ausserhalb des AWIs danke ich herzlichst für gemeinsame Pausen, Unterstützung, Korrekturlesen der Arbeit und vor allem für die nötige Ablenkung von derselben.

Besonderer Dank gilt meiner Familie für ihre Unterstützung bei all meinen Vorhaben und für ihr unverbesserliches Vertrauen in mich und meine Fähigkeiten.

Danke!